Journal of
NIMechE

Journal of the Nigerian Institution of Mechanical Engineers

VOL. 10, NO.2 ISSN 2141 - 2987 **SEPTEMBER, 2021**

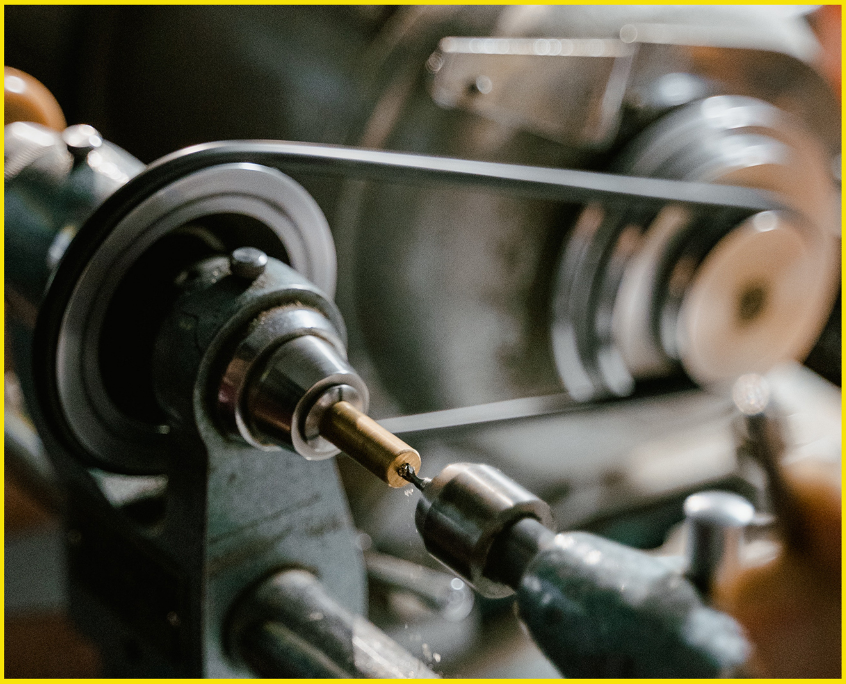

SEPTEMBER, 2021
ISSN 2141 - 2987

The Nigerian Institution of Mechanical Engineers

(A Division of The Nigerian Society of Engineers)

Journal of the Nigerian Institution of Mechanical Engineers

AIMS AND SCOPE OF THE JOURNAL

The journal of the Nigerian Institution of Mechanical Engineers publishes well researched, original and high-quality papers from the academia and industry on Mechanical Engineering Science and its application. the papers may be of a fundamental nature addressing analysis and experiment. reports of advances in Mechanical Engineering theories, techniques, methodologies, applications and practice. Papers may also be reports of design, development and service experience by practicing engineers in industry. the journal strives to bridge the gap between research and development and practical applications of Mechanical Engineering knowledge.

The scope includes:

- Production Engineering
- Power and Energy Systems
- Maintenance Engineering and Management Systems
- Metallurgical Engineering
- Machinery Design and Fabrication
- Automobile Engineering
- Operations Research
- Building Services Engineering
- Nano Systems
- Reliability Engineering
- Engineering Tribology
- Mechanical Engineering Science

EDITOR IN CHIEF
Engr. Prof. Aniekang Offiong
University of Uyo
FNIMechE

ASSOCIATE EDITORS
Engr. Prof. Fatai Anafi
ABU zaria
FNIMechE
Engr. Prof. Vincent. A Balogun
Edo state University, Iyamoh
FNIMechE
Engr. Prof. Sunday Ojolo
University of Lagos
FNIMechE
Engr. Prof. Mohammed DaudaUniversity of Maiduguri
FNIMechE

Engr. Prof. Spencer Onuh
NASDRA, Abuja
FNIMechE

MANAGING EDITOR
Engr. Dr. Sunday Albert Lawal
Federal University of Technology, Minna
MNIMechE

COPY EDITOR
Akoh Dominion
Federal University of Technology, Minna

TECHINCAL EDITORS
Engr. Dr. Mrs. Okopujie Imhade Princess
Covenant University, Ota
MNIMechE

Editorial Board

Professor Adisa Bello
Abubakar Tafawa Balewa University, Bauchi
Professor S.B Adeyemo
University of Ado Ekiti
Professor D. B Yahaya
Bayero University, Kano
Professor O. K. Abubakre
Federal University of Technology, Minna
Professor I. Garba
Bayero University, Kano

Professor N. A.Ademoh
Federal University of Technology, Minna
Professor D. A. Fadare
University of Ibadan
Dr. Uche Obiajulu
Chevron Nigeria PLC
Professor D. A Fadare
University of Ibadan, Ibadan
Professor F.O. Anafi
Ahmadu Bello University, Zaria

.
ZONAL SUB-EDITORS

Ife Zone: Prof A.A Asere
Mechanical Engineering Department
Obafemi Awolowo University, Ile-Ife

Port Harcourt Zone: Prof. Hart Howels
Mechanical Engineering Department
Rivers State University of Science and Technology, Port Harcourt

Enugu Zone: Dr A.J. Ujam
Mechanical Engineering Department
Enugu State University of technology
Enugu

Abuja Zone: Prof. B. O Oloche
Mechanical Engineering Department
University of Abuja, Gwagwalada

Kano Zone: Prof. Adamu Umar Alhaji,
Mechanical Engineering Department
Bayero University Kano

Bauchi Zone: DR. Robinson I Elijah
Mechanical Engineering Department
Abubakar Tafawa Balewa University,
Bauchi

JOURNAL OF THE NIGERIAN INSTITUTION OF MECHANICAL ENGINEERS

SEPTEM,BER, 2021 VOL 10 NO 2 ISSN 2141-2987

CONTENT

Editorial

The vision of the Editorial Board of the journal of the Nigerian Institution of Mechanical Engineers (**NIMechE**) is to establish a learned journal that is recognized internationally for its high academic scholarship and practical applications of mechanical Engineering science. Our mission is to frequently publish articles that are well researched, original and of high quality from the academia and the industry. In order to ensure that we meet our quality standard, we have carefully chosen some outstanding Mechanical Engineers as Editorial Board and regional factors. All the members of the board are engineers who are very knowledgeable in the areas of professional practice.

This Edition of the journals contains 5 high quality papers in the areas o Machining, Renewable energy systems and composite materials.

The board is grateful to the contributors, members of the Editorials board and the secretariat staff or their cooperation and support in making the publication of the journal possible.

Engr. Prof. Aniekang Offiong ***FNIMechE***
EDITOR IN CHIEF

Journal of NIMechE Vol.10 No. 2,
pp 1-14 Printed in Nigeria

ISSN 2121-2987

Copyright@2022, The Nigerian Institution of Mechanical Engineers (A Division of Nigerian Society of Engineers)

NUMERICAL SIMULATION OF OUTDOOR AIR FLOW AND VENTILATION PERFORMANCE AROUND AN ARRAY OF BUILDINGS

Ayo Samuel Adinoyi[1*], Normah-Mohd Ghazali[2]

[1]Department of Mechanical Engineering, Federal University of Technology Minna, Nigeria
[2]School of Mechanical Engineering, Faculty of Engineering, Universiti Teknologi Malaysia, 81310 Johor Bahru, Johor, Malaysia

Corresponding Email: saayo1@gmail.com

ABSTRACT

This study examines outdoor air flow and ventilation around an array of buildings by parameterizing the separation distance (*W*) between the frontal column of buildings and the rest of the building array. The aim was to assess the impact of the separation distance on the air ventilation performance. The study was set around a neighborhood of Kuala Lumpur, the Capital City of Malaysia, and employs the numerical simulation technique utilizing the Reynolds Averaged Navier-Stokes equations. The full-scale size models of common building configurations and weather data around the city were utilized to calculate the mean wind field around the building array. The air ventilation performance was evaluated in terms of air velocity ratio (*VR*) and air flow rate (*AFR*). Results indicate that the invigoration of the flow in the lateral streets is mostly due to corner-stream inflow into the streets through the side-openings. The *VR* was found to increase with increase in the separation distance and this was found to be mainly due to corner-stream inflow to the streets. The increase in *VR* ranged between 15% and 60% between the values at separations $W = 12$ m and $W = 36$ m. The results demonstrate the existence of an optimal location of the frontal column of buildings in a building array that would invigorate the outdoor air flow and improve human thermal comfort.

Keywords: Building array; Numerical simulation; Outdoor air ventilation; Velocity ratio, Air flow rate

1. INTRODUCTION

In low-wind urban areas, improving air flow and ventilation around buildings is very important for the thermal comfort and environmental health of the inhabitants. Several researches has, thus, been used to examine strategies which improve air flow and ventilation around building clusters. Air movement is a direct factor of human thermal comfort as it affects the rate at which heat is transferred from the surface of the human skin by convection and evaporation to the environment. Air ventilation, on the other hand, engenders dilution and exchange of domestic anthropogenic heat and pollutant emissions due to vehicular and domestic activities in the urban environment with the cleaner upper atmosphere to improve thermal comfort (Chen et al., 2017; You et al. 2018).

It has been demonstrated that factors which strongly influence air flow and ventilation in street canyons of building arrays include building packing density (Buccolieri et al, 2010; Buccolieri et al, 2015; Chen et al, 2017), building arrangement (Yim et al, 2009; Yang et al, 2016; You et al, 2018), and direction of ambient wind (van Hooff and Blocken, 2010; Park, 2013; Gough et al, 2018). In other heat generating systems too, it has also been shown that the arrangement of the elements is a crucial factor affecting the rate of heat dissipation (Wulamdari et al, 2020). The application of building density in enhancing air flow and ventilation around building arrays, however, appears to be the most common strategy normally adopted. Unfortunately, the strategy usually involves additional land resource utilization in order to provide the low building density required to engender improved ventilation. This is due of the extra parcel of land that is required in spacing each building in both the longitudinal and lateral directions. On the other hand, if advantage is taken of corner-streams (Penwaden & Wise, 1975) resulting from high-speed winds generated at the base of buildings when an approach wind is intercepted on the buildings' façades, higher street canyon ventilation performance could be achieved with much higher building density. From literatures, it has been observed that this potential and the mechanism by which it occurs have not been adequately explored. It is, thus, the main focus of this study to examine air flow and ventilation around a regular building array by parameterizing the separation distance between the frontal column of buildings and the remaining section of the array and determine how the separation distance can be used to engender higher air flow and ventilation. The lateral passage width between the buildings and the longitudinal distance separating the buildings in the downwind section of the building array are fixed, as such the additional cost incurred by this strategy is that of the marginal increase in the size of the parcel of land between the frontal buildings and the building array downwind.

2. METHODOLOGY OF THE RESEARCH

2.1. Physical Model and Configurations of the Building Layout

The study was conducted with special reference to a low-wind, hot and humid sub-urban area of Kuala Lumpur, the Capital City of Malaysia. Consequently, reference was made to the meteorological conditions of the city and common building configurations found around the city. The meteorological data collected from Subang Meteorological Station situated at a distance of about 23.64 km from Kuala Lumpur Sentral indicate that Kuala Lumpur has a ten-year mean surface wind speed of about 1.52 m/s and an overall 24-hour mean temperature of about 27.77°C. The maximum and minimum mean relative humidity readings are 98% and 38%, respectively. A common residential building style found around Malaysia is building grouping consisting of low-rise buildings, with height equivalent to that of a four-story building. The study employs a 4 x 3 in-line array of the buildings with each of the buildings having dimensions of the building envelope 40 m x 12 m x 10 m in width (W), height (H), and depth (D), respectively. The dimensions of the room units are in accordance with the Bye-Law 42 of Malaysian Uniform Building Bye-Law (UBBL) 1984.

To examine the air flow and ventilation impact of the separation distance on the building array, five different configurations of the array are formed by varying the longitudinal separation distance between the frontal building column and the remaining 3 x 3 array from a minimum of 12 m = H to a maximum of 36 m = $3H$ by a step increase of 6 m = $½H$. The 3 x 3 array has a constant longitudinal separation distance W_c = 18 m based on a previous study. A constant lateral passage width *w* = 6 m between the buildings is maintained based on Malaysia GP022 Planning Guidelines. The layout and geometries of the building array are as shown in Figures 1 and 2, respectively.

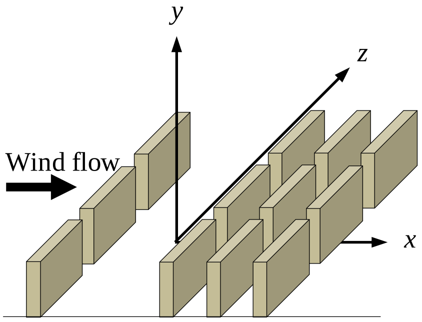

Figure 1 Layout of the building array

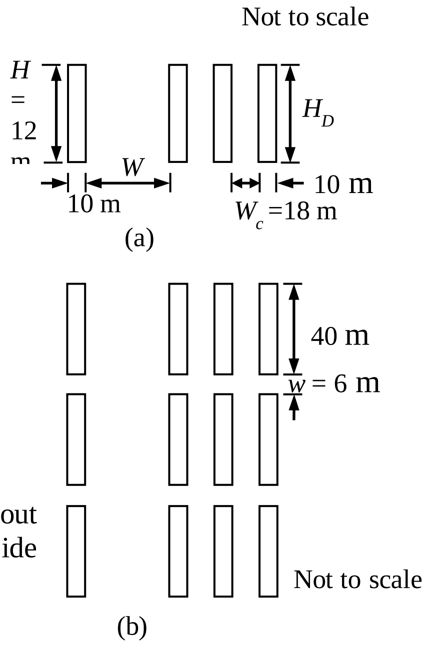

Figure 2 Geometry of the layout of the building array, (a) Side view, (b) Top view

2.2. Approach to the Study and Procedure

The study employs a numerical solution procedure of the computational fluid dynamics (CFD) technique to examine the flow field around the full-scale sizes of the array of buildings. The flow in the urban boundary layer model can be described by the conservation laws of fluid flow. The flow is often considered turbulent at Reynolds number $Re_H \geq 3400$ (Hoydysh, 1974). In the present study, the Reynolds number is determined as $Re_H = 695924.92$, confirming that the flow is in the turbulent regime. The solution procedure adopted is based on Reynolds-Averaged Navier-Stokes (RANS) equations, with closure obtained for the governing equations by the Realizable *k*-*ε* turbulence model (Shih et al, 1995), where *k* is turbulence kinetic energy and *ε* is the dissipation rate of the kinetic energy. For an isothermal condition of the environment, the governing equations are as expressed by Ayo et al, (2015).

2.3. Configuration of the Computational Domain and Boundary Conditions

To implement the numerical solution of the model equations for the flow around the buildings, a computational domain was designed following recommendations of major guidelines and past studies (Tominaga et al, 2008). In the present study, the inflow boundary is located at a distance 5*H* away from the windward face of the first building at the upwind location, while the outflow boundary is set at 15*H* from the leeward face of the last building at the downwind location. The lateral and top boundaries of the domain are set at 5*H* away from the lateral and the top surfaces of the building, respectively.

The profiles of *x*-, *y*- and *z*-components of velocity, the turbulence kinetic energy, the dissipation rate of the kinetic energy, their gradients and the gradient of pressure are specified at the boundaries of the computational domain as the boundary conditions. At the inflow boundary, the vertical profile of velocity prescribed is based on the wind data of Subang Meteorological Station. The mean wind speed of 1.52 m/s was adjusted for the urban location of the study area to obtain a reference mean wind speed of 0.92 m/s. The inflow profiles for velocity, k and ε are specified following the recommendations of COST employing the relations suggested by Richards & Hoxey (1993).

The boundary conditions at the two lateral boundaries and the top boundary of the computational domain are specified by the inviscid wall condition. The conditions at the downwind exit boundary are specified by the outflow boundary conditions. At the solid boundaries, wall-functions are applied to the surfaces following Tominaga et al (2008) to prescribe the mean velocity, k and ε conditions at the wall-adjacent cells as follows:

$$\frac{U_p}{u^*} = \frac{1}{\kappa} ln\left(\frac{u^* y_p}{\nu}\right) + B; \quad k_p = \frac{u^{*2}}{\sqrt{C_\mu}}; \; \varepsilon_p = \frac{u^{*3}}{\kappa y_p} \qquad (1)$$

where U_p, k_p, ε_p are, respectively, the tangential component of wind velocity, the k and ε at the centre-point P of the near-wall cell, and y_p is the distance between point P and wall. B ($\approx 5 - 5.5$) is a universal constant, $u^* = C_\mu^{1/4} k_p^{1/2}$, C_μ $(= 0.09)$ is a model constant of the Standard k-ε model, ν is the kinematic viscosity of the fluid and κ ($\approx 0.4 - 0.42$) is von Karman constant. For the rough ground surface, the wall-function for mean velocity of the wall-adjacent cells is expressed as (ANSYS Fluent 14.0, 2011),

$$\frac{U_p}{u^*} = \frac{1}{\kappa} ln\left(\frac{u^* y_p}{\nu C_S K_S^+}\right) + 5.43 \qquad (2)$$

where $K_S^+ \left(= \frac{u^* K_S}{\nu}\right)$ is the dimensionless surface roughness height, $K_S \left(= \frac{9.793 y_0}{C_S}\right)$ is the dimensional roughness height, and C_S, with value in the interval between 0 and 1, is the surface roughness constant which accounts for the type of roughness.

2.4. The Numerical Simulation

The set of governing RANS equations and model equations for turbulence kinetic energy and its rate of dissipation were solved by the finite-volume numerical method. The computation was implemented by the commercial code ANSYS Fluent 14.0. The computational domain was discretized into unstructured tetrahedral grid elements, with the finest elements concentrated around building corners and in the vicinity of solid surfaces. Far from the solid surfaces the mesh elements are larger, gradually increasing from the surfaces by expansion ratios not greater than 1.2. The aspect ratios of the elements range between 0.5 and 20 (ANSYS Fluent 14.0, 2011).

The pressure-based solver which adopts the Semi-Implicit Method for Pressure-Linked Equations (SIMPLE) algorithm to solve the pressure-velocity coupling was used in computing the mathematical models. At the inflow boundary, user defined function (udf) was used in coding the profiles for U, k and ε to implement the flow conditions at the boundary in the solver. At the lateral and top boundaries of the domain, the prescribed flow conditions were implemented in the solver by specifying zero shear stress condition, while at the downstream boundary, the flow conditions were implemented by the outflow boundary conditions. For the ground surface, equation (2) was implemented in the solver to calculate the values of the mean velocity at the wall-adjacent cells, while equation (1) was implemented to calculate the values for k and ε at the cells. The ground terrain roughness height $y_0 = 0.02\ m$, corresponding to a grassland terrain with grass cover varying between short and long grass (Wieringer, 1992) and a roughness constant C_s = 1.0 were specified to be able to calculate the values of the wall-adjacent variables. The wall-function for a smooth surface as expressed by equation (1) was implemented in the solver for the building surfaces. During the computation, convergence of the iteration process was controlled by specifying a uniform scaled-residual set at 1 x 10^{-5} for all the variables. The implementation of the computation of the model equations was accomplished on the High-Performance Computer (HPC) system of the Centre for Information and Communication Technology (CICT) Unit of Universiti Teknologi Malaysia (UTM), Malaysia.

2.5. Air Ventilation Performance Indicators

The air ventilation performance criteria adopted for the various configurations of the building array examined are air velocity ratio (*VR*) and air flow rate (*AFR*). The *VR* is a dimensionless quantity of the ratio of wind speed at the pedestrian level (2 m height) around a building to the freestream wind speed at the boundary layer height. For the building array under investigation, the measurement planes for the *VR* are as shown in Figure 3.

The *AFR* is a measure of the breathability of an array of buildings to exchange air with the surrounding environment (Buccolieri et al, 2010). In the measurement procedure, mass flow balance of a target control volume is applied across the external openings of the control volume to estimate the amount of flow across the control volume. In the present layout of the building array, the control volume, which is the domain of the downstream array of buildings, and the openings are as shown in Figure 4.

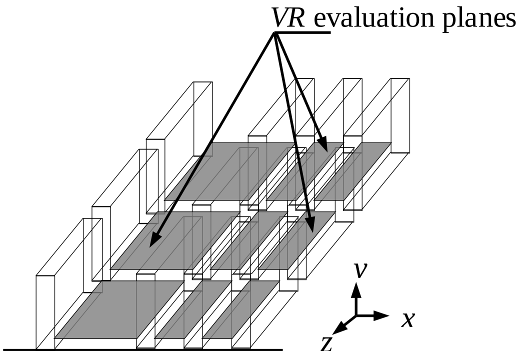

Figure 3 *VR* evaluation planes for the building array

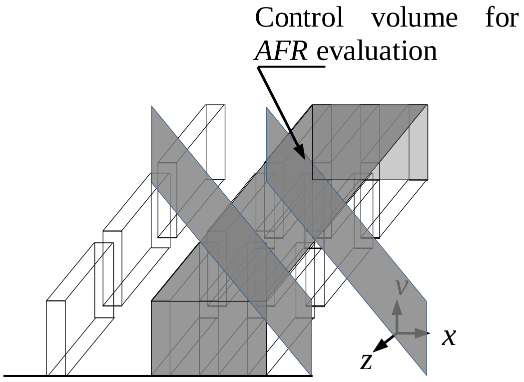

Figure 4 *AFR* evaluation geometries for the building array

The *AFR* normalized with the flow rate referenced at a location far upwind where flow conditions are not disturbed by the presence of the buildings can be expressed as

$$q^{*} = \frac{q}{q_{ref}} = \frac{\int_A \vec{V}.\vec{n}dA}{\int_A \vec{U}_{ref}.\vec{n}dA} \qquad (3)$$

where $\vec{V}$ and $\vec{n}$ are respectively the velocity vector and the unit vector normal to the surface of an opening, and A is the area of the opening. $\vec{U}_{ref}.\vec{n}$ is streamwise velocity at the far upwind location of the building array through an area A with size equivalent to the area of the frontal openings. Equation 3 was used to estimate the air flow rate across the external openings of the building array.

2.6. Validation of the CFD Turbulence Model

In order to ascertain that the RKE turbulence model was robust enough to satisfactorily simulate the flow field around the building array, the validation of the model was performed. This was done by predicting, using the turbulence models, the flow field around an array of scaled-models of city blocks employed in a wind tunnel experiment conducted at the Japanese National Institute for Environmental Studies (Uehara et al., 2000) and comparing the simulation results with data from the experiment. Several research studies have employed data from this experiment in the past for similar validation purposes (Xie et al, 2007). The model city blocks and measurement geometries were set as shown in Figure (5) (Uehara et al, 2000).

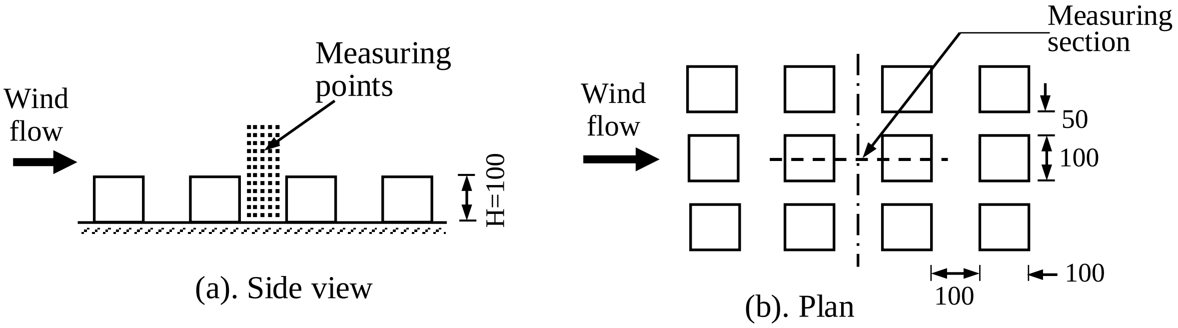

(a). Side view

(b). Plan

Figure 5 Setting of experimental models and the measurement points (in mm)

In the design of the computational domain for the CFD validation, the procedure that was intended to be employed for the design of the computational domain for the simulation of the actual array of buildings as detailed in section 2.2 was replicated for the validation exercise. Relevant data as obtained from the experiment were specified as the conditions at the boundaries of the computational domain. At the inflow boundary, the mean inflow velocity profile data were carefully extracted from the graphical results provided in the literature and fitted with closely approximating curves to serve as the mean wind speed profile at the inflow boundary. The velocity variance and the turbulence kinetic energy were obtained from the friction velocity, the roughness length and roughness Reynolds number, and the scaled velocity variances all of which were also provided in the literature for the approach flow. The profile of the rate of dissipation of turbulence kinetic energy at the inflow boundary was specified as expressed by Richards & Hoxey (1993). At the other boundaries of the computational domain, conditions were specified as were done for the simulation of the actual array of buildings. The wall functions at the solid surfaces of the model blocks and the wind tunnel floor for the values of the mean flow velocity, turbulence kinetic energy and the rate of dissipation of kinetic energy at the wall-adjacent cells were specified following similar procedure. The validation results are presented in section 3.

3. RESULTS AND DISCUSSION

3.1. Results of the CFD Validation

The results of the CFD validation of the Realizable k-ε turbulence model employed in this study are presented in this section. But first, a comparison is made between the profile of the approximating function of the data of the approach flow measured in the wind tunnel experiment employed for the CFD validation and the profile of the data as shown in Figure 6. The figure demonstrates that the approximating function employed for the wind speed data at the inflow boundary closely follows the profile for the measured wind speed data. The results gave the authors the confidence that the right profile of the approach flow has been specified for the CFD validation exercise and therefore proceeded to conduct the validation. The CFD validation result is presented in Figure 7.

In Figure 7 the measured vertical profile of the normalized streamwise velocity component at the center of the target street canyon is compared with the calculated values. The figure shows that the simulation result of the vertical profile of the streamwise velocity component has the same pattern as that of the experimental data. It is also shown in the figure that the result closely agrees with the experimental data, particularly at the higher wind region, i.e. at $y/H \geq 1.0$. It would also be observed from the figure that the in-canyon recirculation vortex observed in the experiment is satisfactorily reproduced by the simulation. It is observed, however, that in the weak wind region, particularly for $y/H < 1.0$, the mean wind speed is calculated a little lower than the values measured in the experiment. The calculation of the centre of the recirculation vortex is also slightly lower than that measured in the experiment. However, these results are consistent with those of Yim et al (2009) and Yoshie et al (2007) and may be due to the inherent weakness of RANS turbulence models to accurately predict the flow field in the wake region. The uncertainty with some of the conditions imposed at the boundaries, such as the profiles for k and ε, and the surface roughness at the solid boundaries, might have also contributed to the observed discrepancy. It is believed that utilizing actual values of these boundary conditions would significantly improve the prediction accuracy of the RKE turbulence model.

When compared to the results of previous validation (Xie et al., 2007) conducted for the unstable condition of the atmosphere, the results for the present study have been demonstrated to yield a much better performance. This may be as a result of the actual 3-D configuration adopted for the present validation compared to the 2-D configuration used in these previous studies or the isolated street canyon employed (Xie et al., 2005) instead of the actual urban street canyon involved. Besides, a closely approximating function of the actual profile of the approach flow at the inlet of the wind tunnel test section was employed for the CFD validation simulation as against the vertically uniform horizontal velocity prescribed at the inlet boundary of the computational domain in the studies.

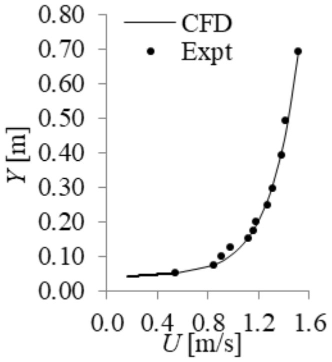

Figure 6 Measured approach flow vertical wind profile and the CFD approximation

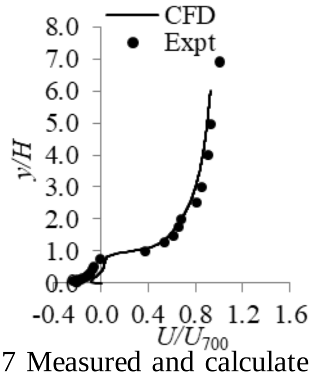

Figure 7 Measured and calculated vertical profiles of normalized streamwise velocity component at the center of the target street

Considering the overall satisfactory performance of the model, it was believed that the model is robust enough in realistically predicting the flow field around the array of buildings under investigation. The air ventilation performance of the different configurations of the building array was, thus, proceeded with to be examined by the turbulence model.

3.2. Results for the Array of Buildings

Results are hereby presented for the air ventilation performance of the flow around various configurations of the regular building array examined. The ventilation performance was measured in terms of air velocity ratio and dimensionless air flow rate, and are presented for the various sections of the streets. But first, the street sections were each designated for the half-domain configuration of the building array as shown in Figure (8), for the purpose of easy identification. In the figure, ten different street sections consisting of nine lateral street sections and a streamwise street section were identified. The street along the direction of flow was designated Longitudinal Street (LG). The lateral street that separates the frontal column of buildings and the remaining array is called Lateral Street 1 (LT1). The street is divided into the portion by the middle of the building array, called Lateral Street 1 Middle (LT1M), and the portion towards the side of the building array and called Lateral Street 1 Edge (LT1E). The next lateral street is designated as Lateral Street 2 (LT2) and similarly divided as Lateral Street 2 Middle (LT2M) and Lateral Street 2 Edge (LT2E). The last lateral street was designated as Lateral Street 3 (LT3) and divided into Lateral Street 3 Middle (LT3M) and Lateral Street 3 Edge (LT3E).

Figure 9 shows the profiles of velocity ratio at the pedestrian level for various sections of the streets of the building array, while the average velocity ratio characteristics for the measurement planes is shown in Figure 10.

Figure 9 shows that *VR* is not uniform across the streets. The *VR* is higher at LT1 than at LT2 and LT3, and at the edge sections than the middle sections. It is highest at LT3E and least at LT3M for all separation distances except at *W* between 24 m and 36 m, with a maximum percentage difference ranging between 146% at *W* = 12 m and 214% at *W* = 24 m. At the edge sections, the *VR* is highest at LT3E and least at LT2E, while at the middle sections, it is highest at LT1M and least at LT2M and LT3M.

The *VR* at the street sections generally increases with increase in separation distance between the frontal column of building array and the objective domain, except at LT2M where it decreases continuously with increase in the separation distance. The *VR* increases continuously with increase in separation distance for the edge sections of the objective domain, while for the separation streets the *VR* increases with the distance until it reaches a maximum, after which it begins to decrease with further increase in the separation. The increase of *VR* with *W* across the street sections ranges between 15% at LT1E and 62% at LT2E between *W* = 12 m and *W* = 36 m. The percentage increase in *VR* across the street sections ranges from 15% to 60% between the values at separations *W* = 12 m and *W* = 36 m.

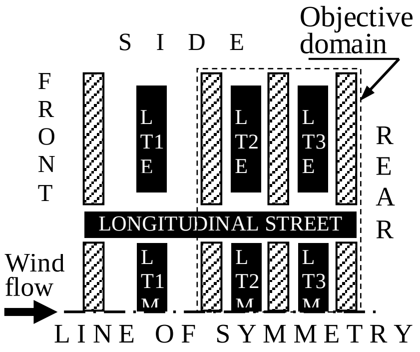

Figure 8 Street designations for half-domain in top view

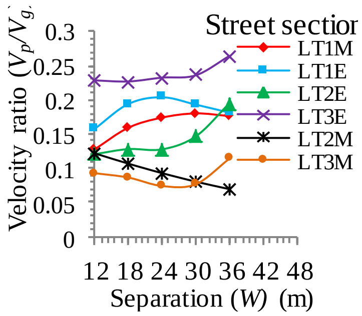

Figure 9 Profiles of velocity ratio at various street sections of the building array

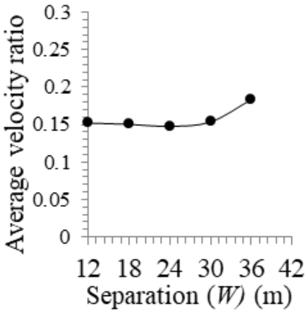

Figure 10 Profile of average velocity ratio

Figure 10 shows that the average velocity ratio characteristics across the whole pedestrian-level planes tends to be invariant with separation distance until as from W = 24 m when the *VR* begins to increase with increase in the separation distance. The increase in in the average *VR* is about 21% between the values at W = 12 m and W = 36 m.

The air flow rate characteristics of the objective domain are shown in Figures 11, 12 and 13. While Figure 11 shows the impact of the separation distance between the frontal column of building and the objective domain on the overall (net) rate of air exchange across the domain boundaries, Figure 12 shows the flow rate characteristics through the front, sides, top and rear openings of the domain in order to examine the contribution of air exchanges across each opening of the domain. Figure 13, on the other hand, shows the flow balance and the direction of flow across the various openings of the objective domain for various separation distances. The entry path into the array for each opening extends from the ground level to the height of the buildings.

It is shown in Figure 11 that the air flow rate for the objective domain generally decreases with increase in the separation distance until it reaches a minimum at W = 30 m, after which it begins to mildly increase with further increase in the separation distance. The result is similar in part to the results observed in Buccolieri et al. (2010). Figure 12 shows that the air flow rate is highest across the top opening, but it decreases with separation distance until at W=30 m, after which it begins to increase. The flow rate across the front opening decreases with increase in separation distance, while that across the side openings increases with increase in the distance. The flow rate across the rear opening is least of all and, like the flow through the front opening, decreases with separation distance. From Figure 13, it would be observed that the net air flow into the domain is through the front and side openings, while the top and rear openings serve for the net outflow.

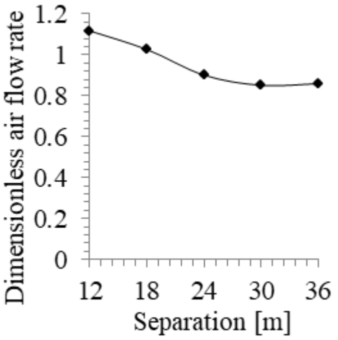

Figure 11 Air flow rate characteristic of the objective

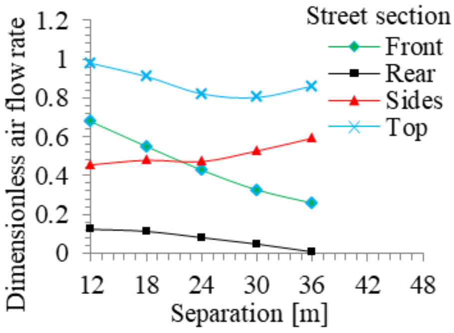

Figure 12 Air flow rate characteristics of the various openings of the domain

Figures 12 and 13 show that the air flow rate through the front opening accounts for the greater proportion of the total inflow at $W < 24$ m, whereas that through the sides accounts for the greater proportion of the net inflow at $W > 24$ m. It may also be observed from Figure 12 that the initial rate of decrease of the inflow through the frontal opening is so high that the rate of increase of the inflow through the sides is not sufficient to offset the rate of decrease. The overall rate of air flow into the objective domain, thus, decreases with separation distance until at W = 30 m as observed in Figure 11. In order to understand the flow mechanism responsible for the flow characteristics just observed, an inspection of typical flow patterns around the building array was undertaken.

Figure 14 shows typical flow patterns around some horizontal sections of the half-domain of the building array at the pedestrian height. From the figure, it would be observed that at W = 12 m, there is high-speed inflow through the frontal opening, which extends far into the objective domain. But as the separation distance increases, the reach of the high-speed inflow decreases and at $W > 24$ m, the high-speed inflow is almost entirely confined to and dispersed into Lateral Street 1. It would also be observed that the inflow through the side openings is mainly due to the high-speed corner-streams. At small separations, e.g. $W = 12$ m, the flow tends to overshoot the openings and therefore the proportion that is intercepted into the objective domain is small.

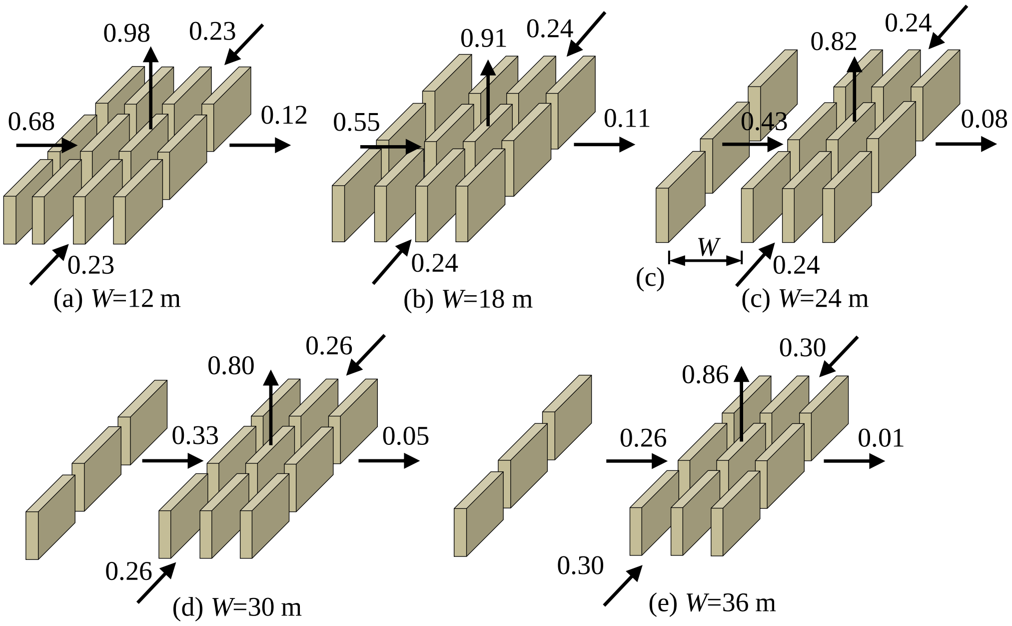

(a) *W*=12 m (b) *W*=18 m (c) *W*=24 m (d) *W*=30 m (e) *W*=36 m

Figure 13 Flow balance and the direction of flow across the various openings of the objective domain for various separation

However, as the separation distance increases, greater proportion of the flow is intercepted into the domain, beginning with LT3 and then LT2. It, thus, indicates that the flows at the middle section of the objective domain, particularly at LT2M, and at LT2 are influenced mainly by the frontal inflow, while those at the edge sections of the objective domain are influenced more by the corner-stream inflow.

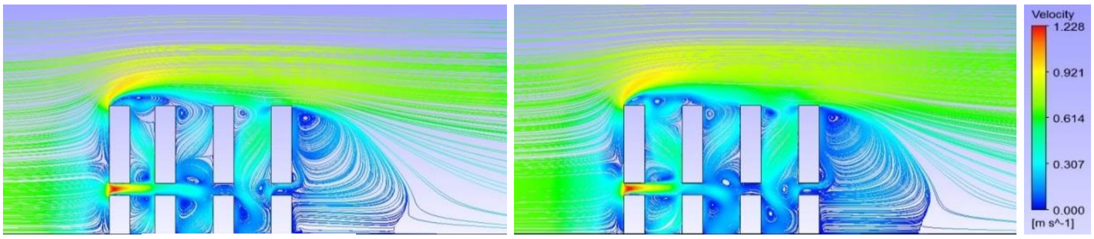

(a) *W* = 12 m (b) *W* = 18 m

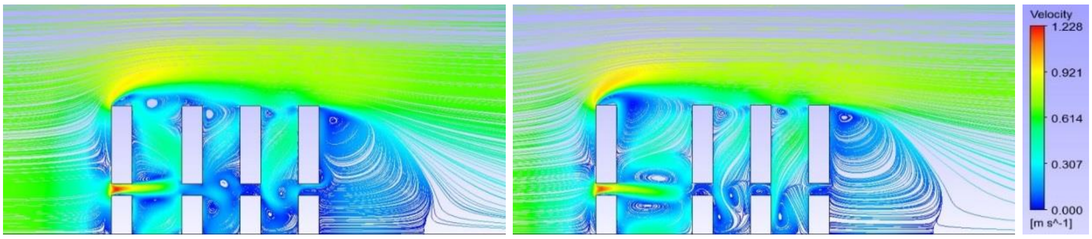

(c) W = 24 m (d) W = 36 m

Figure 14 Typical flow patterns around the building array on horizontal planes at pedestrian level for half-domain. Flow is from left to right

As separation distance increases, the influence of the frontal inflow at LT2M decreases, while that at LT1 initially increases before decreasing, giving rise to the observed *VR* pattern for LT2M and LT1 in Figure 8. However, at the edge sections of the objective domain, as the separation distance increases, the increasing proportion of the corner-stream that is intercepted into the objective domain through the side openings causes the *VR* to increase continuously with increase in the separation distance. At $W \geq 30$ m (Figure 8), the influence of the corner-steam extends to LT3M, causing the *VR* to rise.

Comparing the results for the velocity ratio shown in Figure 9 and that for the air flow rate, Figure 11, it would be noticed that while the mean wind speeds at various streets, except at LT2M, increases with increase in separation distance, the air flow rate decreases with increase in separation distance before tending to increase for $W \geq 30$ m. This could mean that at $W < 30$ m when the inflow through the frontal opening is predominant, a greater proportion of the inflow through the opening does not penetrate into the lateral streets, but is channeled out through the top and rear openings. It would also indicate that the inflow through the side openings invigorate the pedestrian wind flow more than that through the frontal opening. This is observed from Figure 12 in which the rapid increase in the air flow rate through the side openings after W = 24 m is able to offset the decrease in the inflow through the frontal opening, causing the overall air flow rate to begin to increase with separation distance at W = 30 m (Figure 11).

4. CONCLUSION

The characteristics of air flow and ventilation at the outdoor environment of an array of uniform buildings have been studied by numerical simulation for the effects of the separation distance between the frontal column of buildings of a regular building and the rest of the arrays. The results demonstrate that increasing the separation distance can trigger significant increase in the mean wind speeds at almost all sections of the streets. The invigoration of the wind motion is mostly due to the inflow across the lateral street openings, which tends to increase with separation distance. The inflow through the frontal opening contributes very little to the invigoration of the wind motion in the lateral streets. However, the breathability of the neighbourhood as depicted by air flow rate across the boundaries of the building array decreases with increase in the separation distance. It is, therefore, concluded that the separation distance between the frontal buildings and the downwind part of an array of uniform buildings could be used to significantly enhance air flow and thus, thermal comfort, for residential neighbourhoods in which there exists little or no vehicular emissions, or other noxious gases in the environment. Further studies could be carried out to examine the impact of the width of the

Longitunal Street on the ventilation parameters, which appears in the present study to be insignificant probably due to the narrow width specified. The findings could be applied in the building industry where it would provide a useful strategy for enhancing air ventilation and flow in a building array, particularly in low-wind residential environments.

REFERENCES

ANSYS Fluent 14.0 (2011) User's Guide. ANSYS Inc., Canonsburg, PA.

Ayo, S.A., Mohd-Ghazali, N., Mansor, S (2015) Outdoor Ventilation Performance of Various Configurations of a Layout of Two Adjacent Buildings under Isothermal Conditions. Building Simulation. Volume 8(1), pp. 81-98

Buccolieri, R., Sandberg, M., Di Sabatino, S (2010) City Breathability and its Link to Pollutant Concentration Distribution within Urban-like Geometries. Atmospheric Environment. Volume 44 (15), pp. 1894-1903.

Buccolieri, R., Salizzoni, P., Soulhac, L., Garbero, V. Di Sabatino, S (2015) The breathability of compact cities. Urban Climate. Volume 13, pp. 73 – 93.

Chen, L., Hang, J., Sandberg. M., Claesson, L., Di Sabatino, S (2017) The influence of building packing densities on flow adjustment and city breathability in urban-like geometries. Procedia Engineering. Volume 98, pp. 758 – 769.

Gough, H., Sato, T., Halios, C., Grimmond, C. S. B., Luo, Z., Barlow, J. F., Robertson, A., Hoxey, R., Quinn, A (2018) Effects of variability of local winds on cross ventilation for a simplified building within a full-scale asymmetric array: Overview of the Silsoe field campaign. Journal of Wind Engineering & Industrial Aerodynamics. Volume 175.

Hoydysh, W.A (1974). Scale Model Study of Dispersion of Pollutant in Street Canyons. In: 67th Annual Meeting of the Air Pollution Control Association (APCA) Paper No. 74–157. Denver, CO.

Park, J. S (2013). Long-term field measurement on effects of wind speed and directional fluctuation on wind-driven cross ventilation in a mock-up building. Building and Environment. Volume 62, pp. 1 – 8.

Pendwarden, A.D., Wise, A.F.E (1975) Wind Environment around Buildings. Building Research Establishment Report. Department of Environment, BRE, Her Majesty's Stationery Office, London, UK.

Richards, P.J. Hoxey, R.P (1993) Appropriate Boundary Conditions for Computational Wind Engineering Models using the k-ε Turbulence Model. Journal of wind engineering and industrial aerodynamics. Volume 46, pp. 145-153.

Shih, T.H., Liou, W.W., Shabbir, A., Yang, Z., Zhu, J (1995) A New k–ε Eddy Viscosity Model for High Reynolds Number Turbulent Flows. Computers & Fluids, Volume 24, pp. 227–238.

Tominaga, Y., Mochida, A., Yoshie, R., Kataoka, H., Nozu, T., Yoshikawa, M., Shirasawa, T (2008) AIJ Guidelines for Practical Applications of CFD to Pedestrian Wind Environment around Buildings. Journal of Wind Engineering and Industrial Aerodynamics. Volume 96(10), pp. 1749-1761.

Uehara, K., Murakami, S., Oikawa, S., Wakamatsu, S (2000) Wind Tunnel Experiments on How Thermal Stratification

Affects Flow in and above Urban Street Canyons. Atmospheric Environment. Volume 34(10), pp. 1553-1562.

Wieringa, J (1992) Updating the Davenport Roughness Classification. Journal of Wind Engineering and Industrial Aerodynamics. Volume 41(1), pp. 357-368.

Wulandari, D. A., Akmal, M., Gunayan, Y., and Nasruddin (2020). Cooling Improvement of the IT Rack by Layout Rearrangement of the A2 Class Data Center Room: A Simulation Study. EVERGREEN. Volume 07(04), pp. 489-499.

Xie, X., Huang, Z., Wang, J.-S (2005) Impact of Building Configuration on Air Quality in Street Canyon. Atmospheric Environment. Volume 39(25), pp. 4519-4530.

Xie, X., Liu, C.-H., Leung, D.Y.C (2007) Impact of Building Facades and Ground Heating on Wind Flow and Pollutant Transport in Street Canyons. Atmospheric Environment. Volume 41(39), pp. 9030-9049.

Yang, F., Gao, Y., Zhong, K., Khang, Y (2016) Impacts of cross-ventilation on the air quality in street canyons with different building arrangements. Building and Environment. Volume 104, pp. 1-12.

Yim, S.H.L., Fung, J.C.H., Lau, A.K.H., Kot, S.C (2009) Air Ventilation Impacts of the “Wall Effect” Resulting from the Alignment of High-Rise Buildings. Atmospheric Environment. Volume 43(32), pp. 4982-499.

Yoshie, R., Mochida, A., Tominaga, Y., Kataoka, H., Harimoto, K., Nozu, T., Shirasawa, T (2007) Cooperative Project for CFD Prediction of Pedestrian Wind Environment in the Architectural Institute of Japan, Journal of Wind Engineering and Industrial Aerodynamics. Volume 95, pp. 1551–1578.

You, W., Shen, J., Ding, W (2018) Improving residential building arrangement design by assessing outdoor ventilation efficiency in different regional spaces. Architectural Science Review. DOI: 10.1080/00038628.2018.1471388

ISSN 2121-2987

Journal of NIMechE Vol.10 No. 2,
pp 11-28 Printed in Nigeria

Copyright@2022, The Nigerian Institution of Mechanical
Engineers (A Division of Nigerian Society of Engineers)

MECHANICAL AND THERMO-MECHANICAL PROPERTIES OF POT AND COOKER HANDLES PRODUCED USING GROUNDNUT SHELL REINFORCED POLYESTER COMPOSITES

Ashwe, A.[1] Amine, J.D[1], Terhemeniorpine, S.[2]

[1] Department of Mechanical Engineering, JS Tarkaa University, Makurdi, Nigeria
[2] Department of Vocational and Technical Education, Benue State University, Makurdi, Nigeria.

Corresponding e-mail: terhemeniorpines@gmail.com

ABSTRACT

Groundnut shell reinforced polyester (GSP) composites were produced with the aim of determining their suitability as materials for producing cooker/pot handles. Particle size of GSP of 600 µm was used. Percentage composition of GSP was varied in 5%wt., 10%wt., 15%wt., 20%wt. and 25%wt. compositions. Keone peroxide was used as catalyst/hardener and cobaltoctoate as an accelerator. Mechanical (tensile, flexural and impact strength) and thermo-mechanical properties (storage/loss modulus and damping factor) of composite were determined. Tensile strength of composite increased with increase in reinforcement due to treatment of particles with NaOH and high lignin content of GSP. Optimal tensile strength occurred at 20%wt. particle loading. Increase in reinforcement resulted in increase in flexural strength. This was caused by the enhamcement of interfacial adhesion induced through surface modification of GSP with NaOH. Maximum flexural strengh was recorded at 15 wt.% composition. Storage modulus (E') decreased with increase in temperature. This is due to increase in molecular mobility of polymer chains at higher temperatures. Loss modulus increased with increase in temperature up to glass temperature and then decreased. This was due to restriction of relaxation process of chain segments within composites due to higher number of chain segments upon filler addition. Damping factor (tan d) increased with increase in temperature. This fact can be explained as strong filler-matrix adhesion reduced mobility of polymer chains which in turn reduced damping. Values of properties analysed meet requirement for use of composite in producing cooker/pot handles. Optimum values were obtained in sample at 20%wt./150µm.

Keywords: Groundnut shell, composite, mechanical properties, thermo-mechanical properties.

1.0 INTRODUCTION

A composite material is made by combining two or more materials to give a unique combination of properties. One of the materials combined is made up of stiff, long fibres and the other, a binder or 'matrix' which holds the fibres in place. According to Agarwal *et al.* (2006) composites should not be regarded simply as a combination of two materials. In a broader perspective, the composite formed through this combination has its own distinctive properties. In terms of strength to heat resistance ratio or some other desirable quantity, it is better than either of the components alone or radically different from either of them. He also described composite materials as heterogeneous materials consisting of two or more solid phases, which are in intimate contact with each other on a microscopic scale. They can be considered as homogeneous materials on a microscopic scale in the sense that any portion of it has the same physical property**.**

Natural fibers are complex and three-dimensional polymer composites, which are made up of cellulose, pectin, hemicellulose and lignin (Grandawa, 2014). Currently natural fibers form an alternative for glass fiber. They are renewable, widely distributed, available locally, moldable, anisotropic, hydroscopic, recyclable, versatile, non-abrasive, porous, viscoelastic, easily available in many forms, biodegradable, combustible, compostible, and reactive (Grandawa, 2014). Agro-based fibers have a high aspect ratio, high strength to weight ratio, relatively low in energy conversion, and have good insulation properties (sound, electrical and thermal). The fiber structure is hollow, laminated, with molecular layers and an integrated matrix. Some might consider part of these properties as limitations, such as biodegradable and combustible, but these features provide a means of predictable and programmable disposal not easily achieved with other resources. Our resources are being used up, our planet is being polluted, that non-renewable resources will not last forever, and that we need more environmentally friendly materials. In some cases, agro-based fibers are being used for no other reason than their cost compared to other resources. It is therefore important to know and understand chemical and physical properties or what factors affect fiber properties. For the purpose of this research work, an agricultural bye-product, groundnut shell particles was used. Three different sizes of ≤150 μm, ≤300 μm and ≤600 μm were used. Also, the percentage composition of groundnut shell was varied in 30%, 25% and 20% compositions for each particle size.

1.1 Testing/Evaluation Techniques for Composite Materials

Composite samples can be subjected to mechanical and thermo mechanical analyses to determine their properties. This is done through certain test procedures are presented below.

1.1.1 Mechanical testing

The mechanical properties, among all the properties of composite materials, are often the most important properties because virtually all service conditions and the majority of end-use applications involve some degree of mechanical loading. The material selection for a variety of applications is quite often based on mechanical properties such as tensile strength, modulus, elongation, flexural and impact strength. A thorough understanding of mechanical properties, tests employed to determine such properties and the effect of adverse conditions on mechanical properties over a long period is extremely important.

1.1.2 Tensile tests

Tensile test was carried out in accordance with ASTM A638 (2018). Tensile elongation and tensile modulus measurements are among the most important indications of strength in a material and are most widely specified properties of plastic materials. Tensile test, in a broad sense, is a measurement of the ability of a material to withstand forces that tend to pull it apart and to determine to what extent the material stretches before breaking. Tensile modulus, an indication of the relative stiffness of a material can be determined from a stress-strain diagram. The tensile strength, tensile modulus test were carried out and expressed as

$$\text{Tensile strength } (mPa) = \frac{p}{bh} \qquad (1)$$

$$\text{Tensile modulus (mPa)} = \frac{\sigma}{\varepsilon} \qquad (2)$$

Where; p is the pulling force (N), B is the specimen width (mm), H is the specimen thickness (mm), σ is the stress (mPa), $^{\varepsilon}$ is the strain

$$\text{Percentage elongation at fracture} = \frac{elongation}{originallength} x\ 100\% \qquad (3)$$

1.1.3 Flexural test

Flexural test is carried out in accordance with ASTM A790 (2018). The stress-strain behavior of polymers in flexure is of interest to a designer as well as a polymer manufacturer. Flexural strength is the ability of the material to withstand bending forces applied perpendicular to its longitudinal axis. The stresses induced due to the flexural load are a combination of compressive and tensile stresses. Flexural properties are reported and calculated in terms of the maximum stress and strain that occur at the outside surface of the test bar. The sample bar of rectangular cross section was placed to rest on two supports and loaded by means of a loading nose midway between the supports. The maximum axial fiber stresses occur on a line under the loading nose. The modulus of rupture (MOR) and modulus of elasticity (MOE) of composite specimen was determined using the following equation:

$$\text{Modulus of Rupture, MOR} = \frac{3pl}{2bt^2} (mPa) \qquad (3)$$

$$\text{Modulus of elasticity (MOE)} = \frac{pl^3}{4bt^3 Y} (mPa) \qquad (4)$$

Where, p is max load applied on test specimen (N), L is guage length (mm), B is the width of specimen (mm), T is thickness of specimen (mm), Y is the deflection

1.1.4 Dynamic mechanical analysis (DMA)

Dynamic Mechanical Analysis (DMA) is carried out according to ASTM standard D-256 (2018). It is a technique that is widely used to characterize a material's properties as a function of temperature, time, frequency, stress, atmosphere or a combination of these parameters. DMA, is a technique where a small deformation is applied to a sample in a cyclic manner. This allows the materials response to stress, temperature, frequency and other values to be studied. DMA measures stiffness and damping, these are reported as modulus and tan delta. Because we are applying a sinusoidal force, we can express the modulus as an in-phase component, the storage modulus, and an out of phase component, the loss modulus. The storage modulus, either E' or G', is the measure of the sample's elastic behavior. The ratio of the loss to the storage is the tan delta and is often called damping. It is a measure of the energy dissipation of a material.

2.0 MATERIALS AND METHODS

2.1 Materials

The materials used in this study include groundnut shells, polyester, keone peroxide, cobaltoctoate, distilled water, vaseline and sodium hydroxide (NaOH).

2.2 Methods

The methodology employed in evaluation of GSP reinforced polyester composites included: Samples/material collection and preparation, preparation of composites and experimentation/test procedure. Groundnut shells were collected from farmers for preparation of the matrix material. The groundnut shells were taken through various processes to produce the groundnut shell particles, suitable for composite preparation. Moulds used for casting the composites were constructed to specification. Keone peroxide, cobaltoctoate were also collected and used alongside polyester to form polyester resin. Lastly, the composite material was produced using various compositions of matrix and reinforcement components as specified.

2.3 Material collection and preparation

Groundnut shells were collected from local farmers and washed with ordinary water to remove impurities. They were further washed with distilled water to remove sand and other impurities. The washed shells were sun dried for two days. The shells were soaked in a large bowl containing an alkaline solution of 10% NaOH solution for 2 hours for chemical treatment. This alkaline treatment, according to Akindapo *et al*. (2015), increases the tensile strength and flexural strength of the composites. They were removed after that and then washed with distilled water until all NaOH got eliminated. Subsequently, the shells were sun dried for 2days to remove all moisture content in the fibers. Washed and dried groundnut particles are shown in Plates 1 and 2. The dried shells were ground using a grinding mill until particles were relatively smooth. The ground particles were sieved using hand sieves. Sieve sizes used were ≤150 µm, ≤300 µm and ≤600 µm to obtain the variation in particle sizes of groundnut shells.

2.4 Preparation of composites

The matrix component used was polyester. Cobalt octane (0.35% by volume of resin) was added to act as accelerator and methyl ethyl ketone (MEKP) (1% by volume) was added to act a catalyst. The use of accelerator is necessary because resin does not cure properly. The use of accelerator and catalyst is not high because a high percentage reduces gel time of polyester resin and may adversely affect impregnation. The masses of all the different volume fractions were estimated using the relationship between mass and volume. To prepare the laminate, polyester resin, accelerator and catalyst were thoroughly mixed in a plastic container. The measured quantity of groundnut shell particles was added in the plastic container and mixed thoroughly. The mixture was poured into the mould and the lid was placed over it. External pressure was applied to the mould to ensure good compaction and remove all pores. The closed mould was kept under a load of 25 kg at room temperature for about 24 hours before the composite was removed from the mould. Three different particle sizes (≤150 µm, ≤300 µm, ≤600 µm) of groundnut shell particles were used. Different volume fractions (5%, 10%, 15% 20% and 25%)wt were prepared for sample production. The detailed formulation of the composites for each treatment was divided into five main composition ratio as shown in Table 1. A total of fifteen samples were used in the evaluation of the physical, mechanical and thermo-mechanical properties of GSP reinforced polyester

Plate 1: Untreated Groundnut shells for composite preparation

Plate 2: NaOH Treated Groundnut shells for composite production

Table 1:Percentage Composition of Groundnut Shell/Hardener/Catalyst Composite

S/N	Sample	Composition (by % wt.)	
		GSP	Resin
1	A	5	95
2	B	10	90
3	C	15	85
4	D	20	80
5	E	25	75

3.0 RESULTS AND DISCUSSION

3.1 Effect of reinforcement and particle size on tensile strength

From the tensile strength test carried out and presented in Fig. 1 above, the sample with the highest tensile strength in sample 600µm, 20%wt with tensile strength of 9.56MPa. this was so because tensile strength increased with reinforcement. The increase in tensile strength is noticed upto 20 % reinforcement beyond which there is a drop.

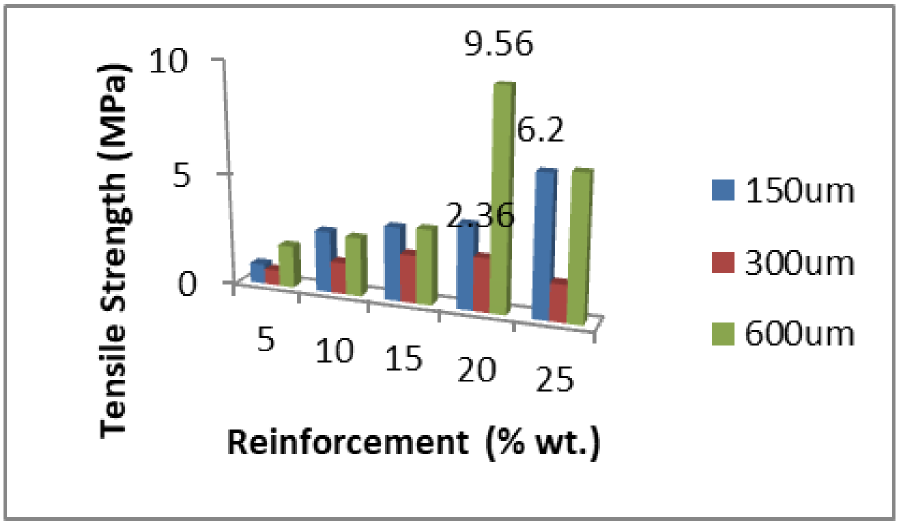

Fig. 1: Effect of Reinforcement on Tensile Strength of groundnut shell reinforced polyester

This is in conformity with the work of Adeosun *et al.* (2016) who posited that tensile strength increase with reinforcement until it reaches saturation and the decreases. The decline after saturation is attributed to agglomeration and sediment effects associated with higher filler content or poor wetting between the fillers and matrix resulting in formation of micro-cracks. Also, from the works of Usman *et al.* (2016), tensile strength of samples increased as a result of treatment of fibres (particles).

Smaller particle sizes had the highest tensile strength. Also, ultimate tensile strength increased with particle loading (reinforcement). Optimal tensile strength occurred at 20wt. % particle loading. Further loading resulted in decrease. In the same vein, Raju *et al*. (2012) explained that fillers had created some reinforcing effect and had been responsible for the increase in tensile strength. However, at some point of further increment in the filler content, a decrease in the tensile strength was witnessed. During tensile loading, partially separated microspaces are created that obstructs stress propagation between the fibre (particle) and the matrix. As the fibre (particle) loading increases, the degree of obstruction increases, which in turn decreases the strength of the samples.

Based on particle size variation, tensile strength was seen to decrease with increase in particle size up till 300 µm beyond which it increased. Potadar and Kadam (2018) aserts that tensile strength decreases with increase in the grain size of the particulate groundnut fibre. Also,Njoku *et al*. (2011) stated that for a given particle weight fraction, the composite strength increases with decrease in particle size. Smaller particles have a higher total surface energy for a given particle loading. Strength increases with increasing surface area of the filler particles through a more efficient stress transfer mechanism. Addition of particles leads to an increase in strength and smaller particles give better reinforcement.

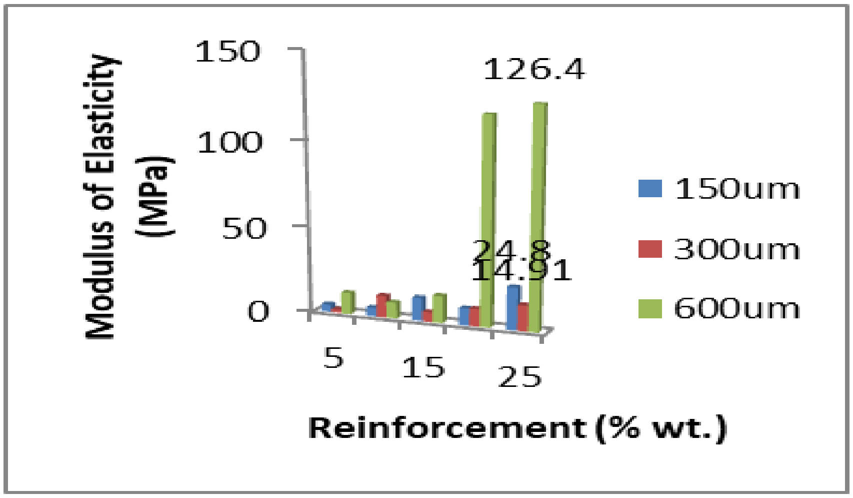

Fig. 2: Effect of Reinforcement on Modulus of Elasticity of groundnut shell reinforced polyester

3.2 Effect of reinforcement and particle size onmodulus of elasticity

Modulus of Elasticity result is presented in Fig. 2. The sample with the highest modulus of elasticity is sample at 600 µm and 25%wt with MOE of126.4MPa. This is so because modulus of elasticity increased as the reinforcement increased in all samples. Similar results have been reported by other works of literature that modulus of elasticity increases with increase in reinforcement (Haque *et al*, 2009). This behavior may possibly lead to the conclusion that modulus of elasticity depends on the filler content rather than particle-matrix interface (Raju *et al*, 2012). Furthermore, increase in modulus of elasticity for higher filler content is due to the higher stiffness of the reinforcing particles rather than that of the matrix material. Owing to this overall stiffness of the composite, samples increased and thus modulus of elasticity was enhanced. Fu *et al*, (2008) reported that the particulate composite modulus is insensitive to particle size but when the particle decreased to a critical value (usually in the nano size range), the effect on the composite modulus is more significant with modulus increasing with decreasing particle size below this critical value.

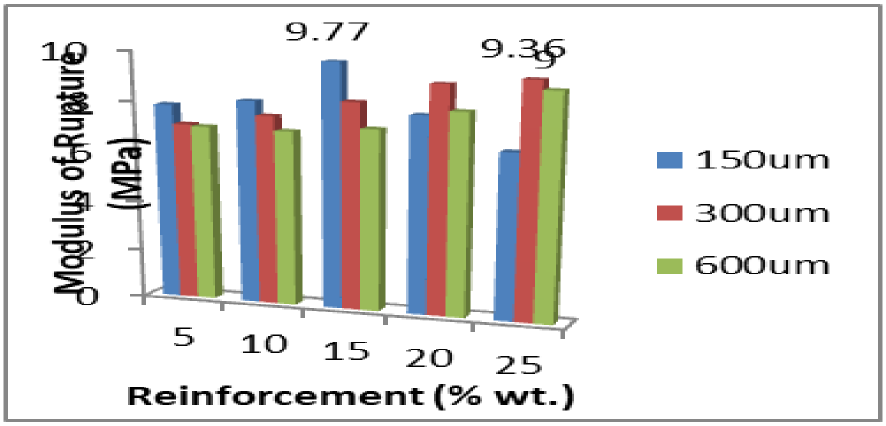

Fig. 3: Effect of Reinforcement on Modulus of Rupture (Flexural Strength) of groundnut shell reinforced polyester

3.3 Effect of reinforcement and particle size on flexural strength

Results of flexural strength test are shown in figure 3. Sample with the highest flexural strength is sample at 150 µm and 15%wtwith MOR of 9.77MPa. Results show that the flexural strength and flexural modulus of samples increased with increase in filler content. This is caused by the enhancement of interfacial adhesion induced through surface modification of the filler component with NaOH. The better wetting between the filler component and the matrix component are achieved thus improving the level of adhesion. The highest flexural strengh value was recorded at 15 wt.% GSP. Beyond this point, there was a decease in the value of MOR. This decrease can be attributed to weak filler matrix adhesion and insufficient wetting of the fillers by the resin for the higher filler content. In accordance with this, Potadar and Kadam (2018) stated that the flexural strength first decreases with increase in the grain size and then further increases with increase in the grain size.

3.4 Effect of reinforcement and particle size on storage modulus

Storage modulus increased to a maximum of 2500 MPa as the temperature increased to 35 ^{0}C. As the temperature increased beyond 47 ^{0}C there was a drop in storage modulus of the sample. The results of the storage modulus showed that, as the temperature increased, storage modulus (E’) decreased for all the samples. This can be attributed to the increase in the molecular mobility of the polymer chains at higher temperatures. As for all composite materials, these variations correspond to a material transition. Similar results were observed by Ornaghi *et al.* (2010), as the temperature increased, E’ decreased for all composite materials. The curves of the storage modulus clearly exhibit frequency dependence as seen from the figures; higher frequencies gave higher storage modulus values. According to Ornaghi *et al.* (2010), modulus measurements performed over a short time (high frequency) result in higher values and on the other hand, if the reverse is done, it results in lower modulus values. On varying the oscillation frequency, changes occur in E' of composites.

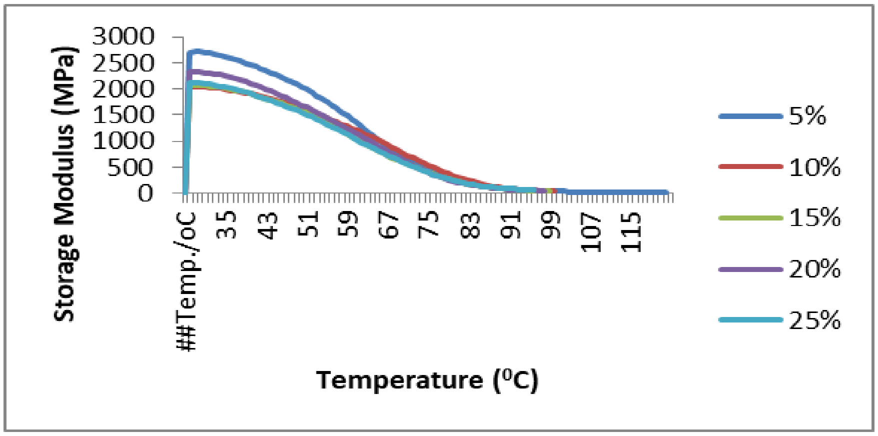

Fig. 4: Variation of storage modulus at 2 Hz

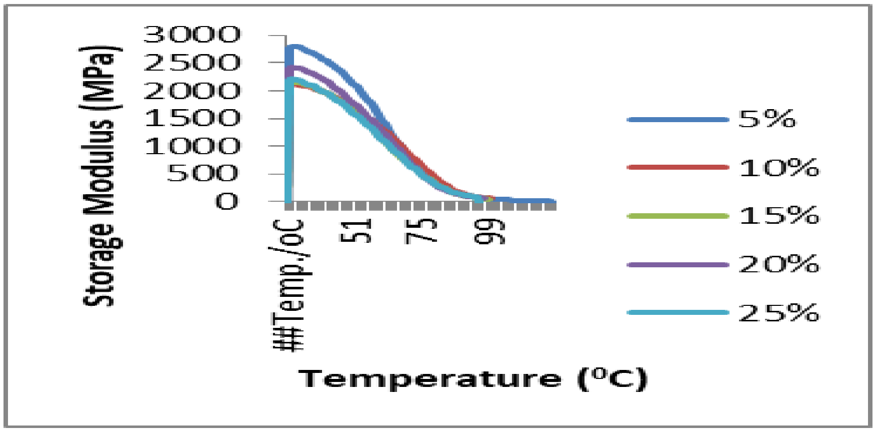

Fig. 5: Variation of storage modulus at 5 Hz

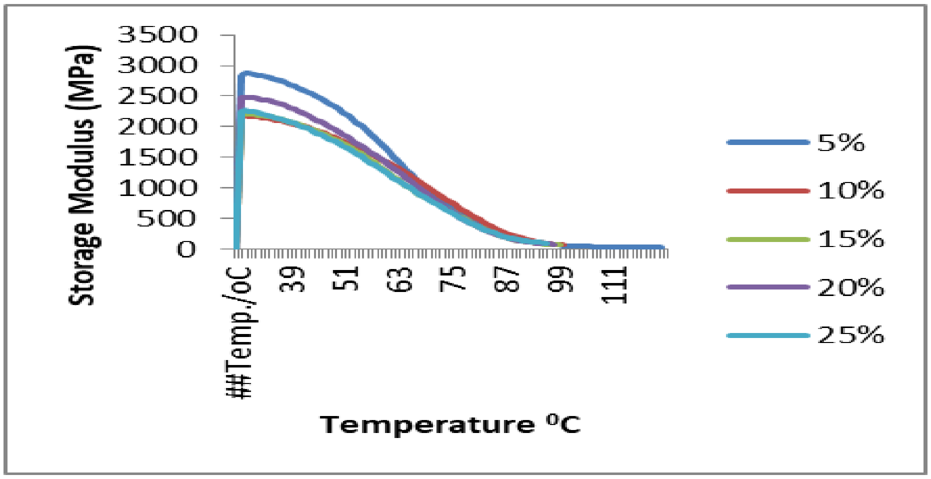

Fig. 6: Variation of storage modulus at 10 Hz

3.5 Effect of reinforcement on loss modulus (E'')

Loss modulus increased with increasing temperature up to the glass temperature and then decreased in all samples. The glass transition temperature (Tg) of the composite was measured from the peak of the loss modulus curve according to ASTM D4065 (Ornaghi *et al*, 2010). The loss modulus result for 20 % reinforcement showed that, the glass transition temperature occurred around 67.8 ^{0}C at all the frequencies of 10 Hz, 5 Hz and 2 Hz. The loss modulus results clearly exhibit frequency dependence. The glass transition temperature of the composites shifted to higher temperatures at higher frequencies in all samples. According to Ornaghi *et al*. (2010), modulus measurements performed over a short time (high frequency) results in higher values and on the other hand, if the reverse is done, it results in lower modulus values. It was observed that, for higher filler content, the loss modulus curve spread over a wider distribution and showed a higher peak. This effect was a consequence of the inhibition/restriction of the relaxation process of the chain segments within the composites due to higher number of chain segments upon filler addition (Ornaghi *et al*, 2010).

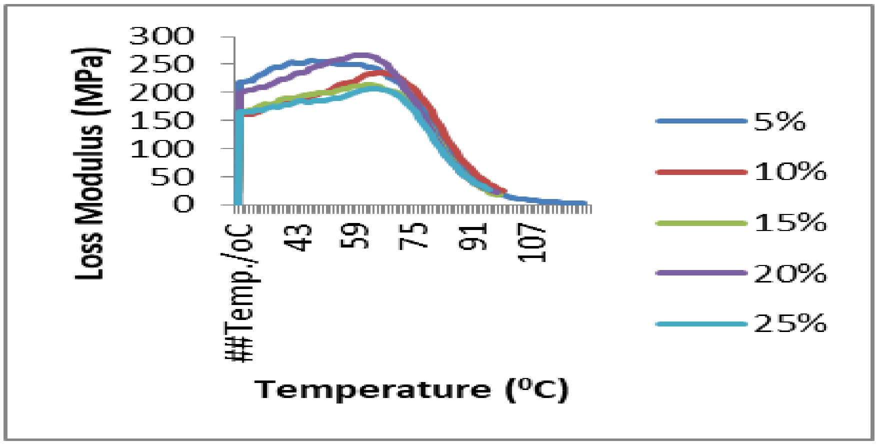

Fig. 7: Variation of loss modulus at 2 Hz

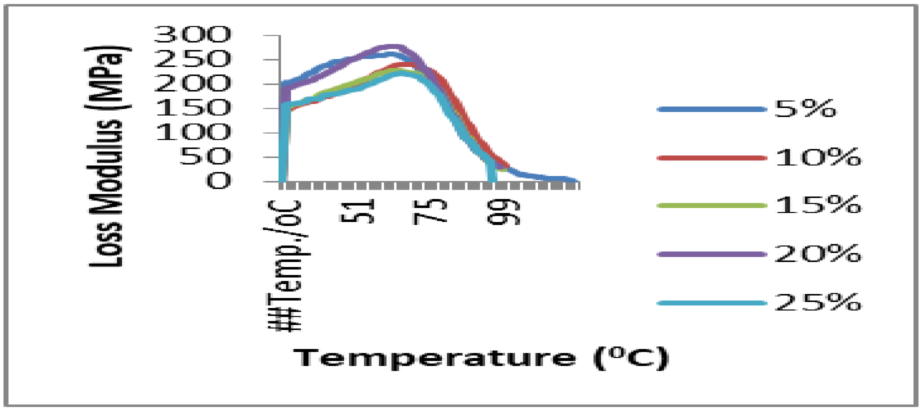

Fig. 8: Variation of loss modulus at 5 Hz

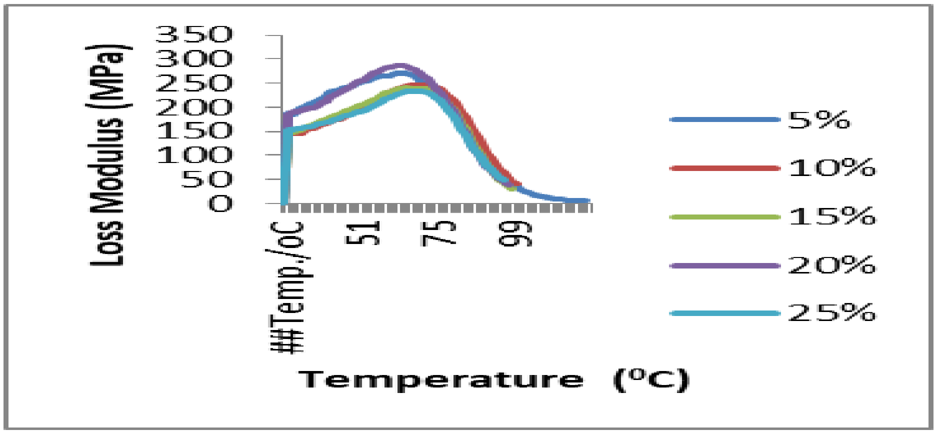

Fig. 9: Variation of loss modulus at 10 Hz

3.6 Effect of reinforcement on mechanical loss factor (Damping parameters) Tan d

Damping factor (tan d) increased with increase in temperature and reached a maximum in the transition region and decreased in rubbery region in all samples. According to Ornaghi *et al.* (2010), all materials exhibit a relaxation process, which is associated with the glass-rubber transition of the matrix. This relaxation process, involves the release of cooperative motions of chains between crosslinks. Below Tg damping is low because, in this region, the chain segments are in the frozen state. Hence, the deformations are primarily elastic and the molecular slips resulting in the viscous flow are low. Also, in the rubbery region, the molecular segments are quite free to move and hence damping is low and this there is no resistance to flow

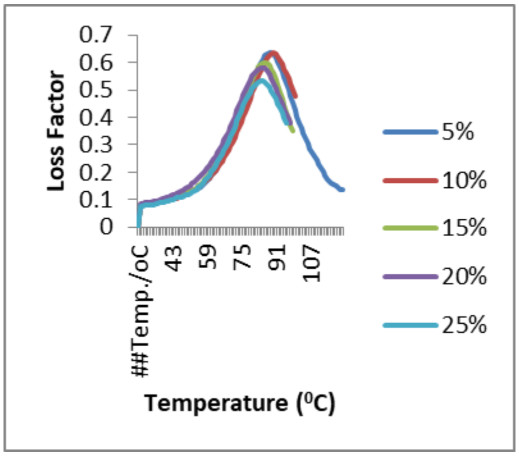

Fig. 10: Variation of loss factor at 2 Hz

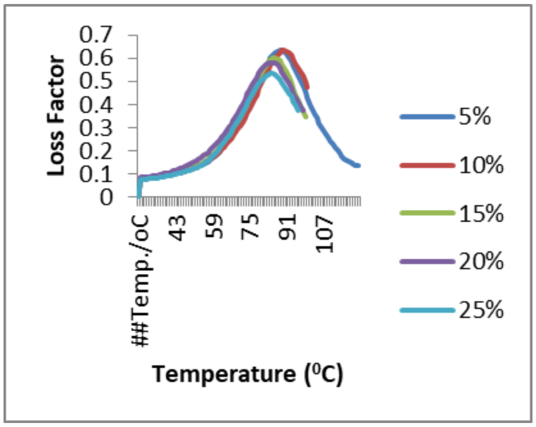

Fig. 11: Variation of loss factor at 5 Hz

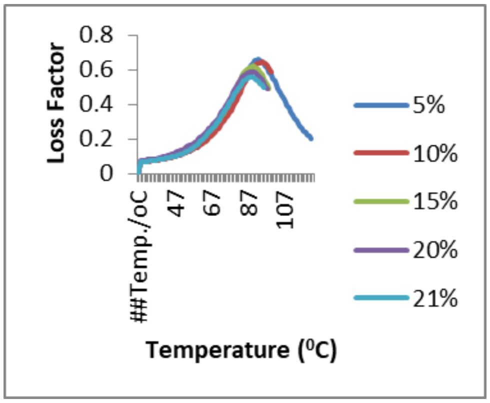

Fig. 12: Variation of loss factor at 10 Hz

3.7 Optimum Results

The most satisfactory particle-matrix composition of groundnut shell with polyester that produced thermosetting plastics with the best mechanical and thermomechanical properties are: tensile strength, at 600 µm and 20%wt. (9.56 kg/mm^2); flexural strength, at 150 µm and 15%wt. (9.77 MPa); storage modulus, 600 µm and 25%wt. (126.4 MPa); loss modulus, at 20%wt. and 67.8 ^{0}C (287 MPa) and lastly loss factor at 25 %wt. and 92.3 ^{0}C (0.557). This is presented in Table 2 below.

Table 2: Samples With Highest Performance

Quantity measured	**Percentage filler content**	**Particle size/temperature**	**Figure obtained**
	20%	600 µm	9.56 kg/mm^2
Flexural Strength	15%	150 µm	9.77 MPa
Density	20%	150 µm	0.97 g/cm^2
Percentage water absorpti	10%	150 µm	0

on			
Storage modulus	5%	27°C	2800 MPa
Loss modulus	20%	67.8⁰C	287 MPa
Loss factor	25%	92.3°C	0.557

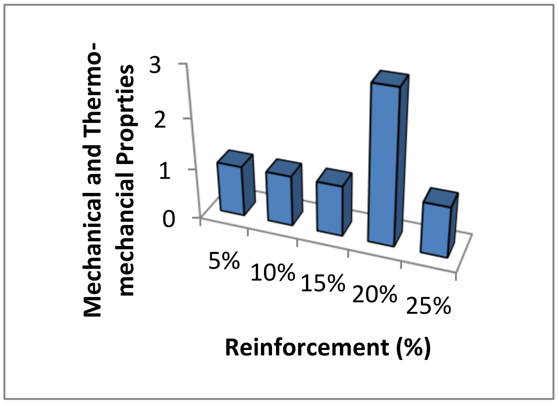

Fig. 13: Optimum results for variation in percentage reinforcement of GSP

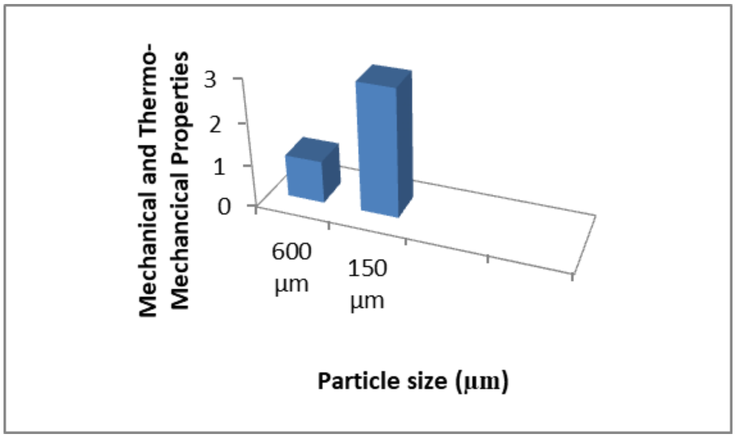

Fig. 14: Optimum results for variation in particle size of GSP

4.0 CONCLUSIONS

This study investigated the feasibility of using groundnut shell reinforced polyester composites in the production of cookware parts such as cooker and pot handles. The following conclusions were drawn:

1. Thermosetting plastic composites were produced using groundnut shells and polyester at different groundnut shell/polyester compositions;
2. Evaluated mechanical properties (tensile strength, flexural strength and impact strength) of the composite material produced were satisfactory with the mos satisfactory being sample produced at 20% GSP composition and 150 µm.
3. Evaluated thermo-mechanical properties (storage modulus, loss modulus and damping factor) of composite material produced were satisfactory with the most satisfactory being sample produced at 25% GSP composition and 92°C.

REFERENCES

Adeosun, S.O., Gbenebor, O.P., Akpan, E.I., and Udeme, F.A. (2016). Influence of Organic Fillers on Physicochemical and Mechanical Properties of Unsaturated Polyester Composites: *Arabian Journal of Science and Technology*. 41(10): 4153-4159.

Agarwal, B.D., Broutman, L.J. and Chandrashekhara , K. (2006) *Analysis and Performance of Fiber Composites*: Chicago, Illinois, USA

Akindapo, J.O.; Binni, U.A.; Sanusi, O.M. (2015). Development of Roofing Sheet Material Using Groundnut Shell Particles and Epoxy Resin as Composite Material. *American Journal of Mechanical Engineering*. 4(6): 165-173

Haque M.M., Saiful, I.M., Sakinul, I.M., Nazrul, I. (2009). Physicochemical Properties of Chemically Treated Palm Fiber Reinforced Polypropylene Composites. *Journal of Reinforced Plastics and Composites*; 29: 1734-1742

Njoku, R.E., Okon, A. E. and Ikpaki, T.C. (2011) Effects of Variation of Particle Size and Weight Fraction on the Tensile Strength and Modulus of Periwinkle Shell Reinforced Polyester Composites. *Nigerian Journal of Technology*. 30(2).

Ornaghi, H.L., Bolner, A.S., Fiorio, R., Zattera, A.J. and Amico, S.C. (2010). Mechanical and Dynamic Analysis of Hybrid Composites Molded by Resin transfer Molding. *Journal of Applied Polymer Science:* 118:887-896.

Potadar, V.O., and Kadam, G.S. (2018). Preparation and Testing of Composites using Waste Grundnut Shells and Coir Fibres: *Procedia Manufacturing*. 20: 91-96

Raju, G.U.; Kumarappa, S.O.; Gaitonde, V.N. (2012). Mechanical and Physical Characteristics of Agricultural Waste Reinforced Polymer Composites. *Journal of Material and Environmental Science*, 3(5). (907-916)

Usman, M.A., Momohjimoh, I. and Gimba, A.S.B. (2016) Effect of Groundnut Shell Powder on the Mechanical Properties of Recycled Polyethylene and Its Biodegradability. *Journal of Minerals and Materials Characterization and Engineering*.4: 228-240.

ISSN 2121-2987

Journal of NIMechE Vol.10 No. 2, pp 29-41
Printed in Nigeria

Copyright@2022, The Nigerian Institution of Mechanical Engineers (A Division of Nigerian Society of Engineers)

DESIGN ANALYSIS OF A PLASTIC SHREDDING MACHINE

Solanke O. and *Abdullahi, A. A.

Department of Mechanical Engineering, Federal University of Technology, Minna

aliuaabdullah@futminna.edu.ng

ABSTRACT

Waste is naturally produced by all humans and possesses great health and environmental risks. The lack of proper waste disposal in developing communities lead to disease out breaks. Most of the wastes available are made up of plastic materials. Shredding of plastic is a crucial step in the recycling process of plastic materials and the machines available for its execution are bulky, scarce and generally unavailable. The paper aims at the design analysis of a shredding machine for processing waste plastics. From the analysis the minimum required power to shred plastic was obtained as 721 N and the electric motor to drive the system was determined to be 5 hp. The bending and twisting moments acting on the shaft were determined to be 16 Nm and 15.3 Nm respectively which led to the selection of a shaft of 25 mm diameter. Further study to be conducted are applying the design result for fabrication and performance evaluation of the plastic shredding machine.

Keywords: *Design Analysis, Electric Motor, Performance Evaluation, Plastic Materials, Shredding Machines.*

1.0 INTRODUCTION

Waste is naturally produced by all humans and possesses great health and environmental risks. Indiscriminate loitering of waste is prevalent in our streets due high rate of production and in adequate disposal mechanisms. Studies link the lack of proper waste disposal to water contamination in developing communities and cholera outbreak in those places (Al-Gheethi *et al*., 2018; Chinedu*et al*., 2018). Aside from these serious risks in developing nations traffic congestion, drainage blockages are some of the problems caused by the lack of efficient waste management practice in Nigeria. Plastic and non-degradable materials constitute most of the waste disposed in the present day (Jadhav *et al*., 2018). Plastics are made from petroleum products and if improperly disposed cause grave agricultural and environmental problems due to the long time it takes without degrading in the soil. Most of the plastic disposed take more than 500 years without degrading (Canopoli *et al*., 2019; Akash, *et al*., 2019), presently the world over it constitutes a nuisance. Artificial islands formed by these non-degradable wastes can even be viewed from satellites. Recycling these types of materials seem to be the solution to this menace.

Thermo plastics do not undergo chemical change when heated therefore are good candidates for recycling (Olukunle, 2016). Recycling of plastics is the process of recovering plastic materials and reprocessing them into usable products. Various products can be made from recycling plastics, like polytene bin liners, and carrier bags, plastic bottles, flooring and window frames. The recycling process includes washing, sorting, shredding, heating, extruding and pelletizing. The recycling of plastics requires specialized machines. The shredding process is crucial as the enormous volume of the waste is plastic is reduced to make it easy to undergo the rest of the recycling process and to ease transportation of raw materials. Machines available are bulky, costly, scarce and generally out of the reach (Akash, *et al*., 2019; Olukunle, 2016) if commensurate with amount of waste available.

Shredding of plastic is a crucial step in the recycling process of plastic materials and the machines available for its execution are bulky, scarce and generally unavailable (Akash, *et al*., 2019). Moreover, the sheer volume of plastic waste available makes it paramount to develop smaller machines using locally available materials that are less bulky, easily operational systems that are capable of shredding plastic waste. The paper aims at carrying out design analysis of a shredding machine to generate standard design data for fabrication and performance evaluation of a shredding machine.

Waste generation is a natural and inevitable phenomenon. As humans consume, waste is bound to be produced.According to Chinedu *et al.,* (2018) about 42 million ton of waste is generated annually in Nigeria. Disposing of this waste is a major concern in developing countries. Most cities in Africa spend more than 50 % of their environmental budget on municipal waste management. The process of waste disposal in the municipals is highly inefficient due to poor infrastructure available (David and Joel, 2018). Over 20 % of the waste generated is made up of non-degradable plastic materials (David and Joel, 2018) making the situation even worse.

Recycling of solid wastes have been recycled to some degree for many years now, and in more recent years plastic recycling has become common. In most plastic recycling operations, the first step after sorting is to shred and grind the plastic into chips, which are easier to clean and handle in subsequent steps. Some of the common types of plastic shredders are:

single shaft plastic shredders, multiple shaft plastic shredders, high-speed-low torque plastic shredders, low-speed-high-torque plastic shredders, simple plastic shredders, and industrial plastic shredders (Adepo and Obanoyen, 2017).

Reddy and Raju (2018) developed a mini plastic shredding machine which was powered with a 1.5 hp motor. Mild steel was selected to be used for the blades that will perform the shredding action. The blades were divided into two parts; the fixed and the movable blades. The movable blades are bolted on the blade carrying bars welded on the shaft while the fixed blades are bolt on the edge of the lower hemisphere of the cutting chamber. The performance is said to be efficient though no results or discussion is presented. Adepo and Obanoyen (2017) found 11.5 m/s to be the optimum velocity needed to run their shredder. Their machine was designed to shred nylon materials and had a 97 % efficiency was recorded from the performance evaluation though results of experiments were not presented. VijayAnanth *et al*. (2018) included gear in their design. The gears transmit the rotation between two shafts. The number of driver and driven gear teeth are 50 and 70 respectively. A 2 hp motor was selected after the necessary design analysis carried out. VijayAnanth *et al*. (2018) suggested that the blade tips be strengthened by coating with the help of a carbide tool. The blades were arranged on both shafts in such a way that each had a total of nine blades. A space was provided between the blades in the design to allow the shredded materials to fall.

The shredder developed by David and Joel (2018) was capable of delivering an end product of 10 – 20 mm size. With a hopper size determined to be 0.0063 m^3 the machine was able to accommodate over 25 kg of waste and shred within 43 s using a shredding force of 690 N. The major components in the machine are hopper made from mild steel plate of 0.22 mm and angle bar of 0.33 mm for rigidity. A flywheel was incorporated to resist changes in speed and help steady the shaft rotation and uneven torque. The fly wheel as defined by David and Joel (2018) is a hevy material attched to a drive shaft having most of its weight concerntrated at the circumference. Jadhav *et al*. (2018) used a speed of 50 rpm to drive the main shaft of their machine, the speed was reduced from a motor speed of 1440 rpm.

2 MATERIALS AND METHODS

The materials used for the fabrication of the machine are mild steel sheet for the hopper, main enclosure and the chute, mild steel for both shafts to drive the blades. Angle bars were used for the frame. Figure (1) represents the conceptual model designed in AUTOCAD modelling software.

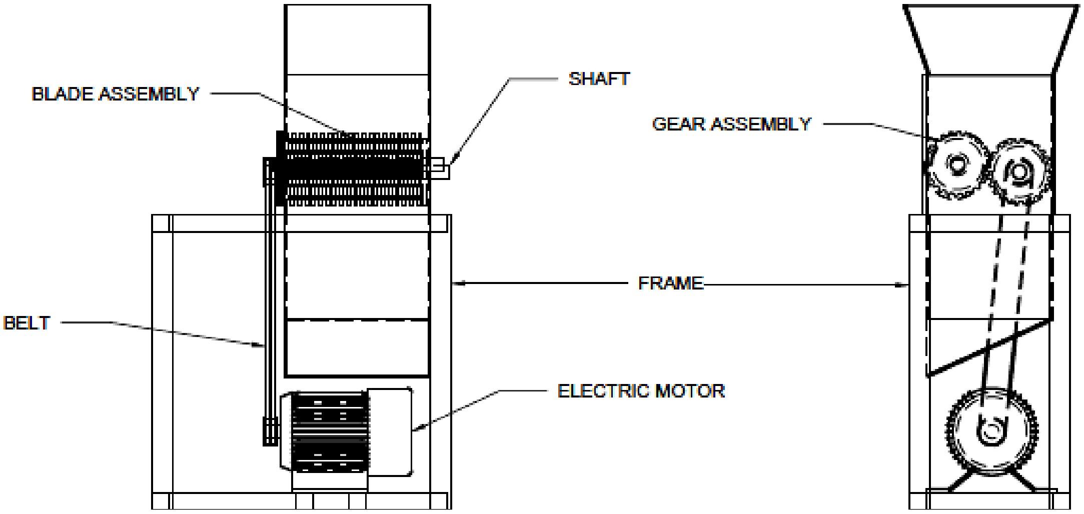

Figure 1: Schematic of proposed plastic shredder

2.1 Design Analysis

2.1.1 Plastic Materials

Plastic type selected for analysis and evaluation is high density polyethylene (HDPE) with density 960 kg/m^3 (Khalaf, 2012). The machine must be capable of shredding HDPE to the desired dimension. The proposed shredder is depicted in Figure 1, it is driven by two shafts with blades arranged in such a way to provide optimum shredding.

Table1: The properties of various polymers(Source: Grigore, 2017)

Properties	**Limits**	**TYPES OF POLYMERS**					
		PP	**LDPE**	**HDPE**	**PC**	**PBT**	**PAI**
$\rho(g/cm^3)$	Upper	0.920	0.925	1.000	1.24	1.35	1.45
	Lower	0.899	0.910	0.941	1.19	1.23	1.38
Tg (The glass transition temperature)	Upper	-10	-125	-100	150	45	2.90
	Lower	-23	-	-133	140.5	20	2.44
σ_{max}(MPa)	Upper	41.4	78.6	38	72	55.9	1.92
	Lower	26	4	14.5	53	51.8	9.0
E (GPa)	Upper	1.776	0.38	1.490	3	2.37	4.4
	Lower	0.95	0.0.055	0.413	23	-	2.8

2.1.2 Minimum Required Power to Shred the Plastic

The design is commenced by determining the power required to shred the HDPE material. First the volume that will be fed to the machine for a single operation is determined from the hopper and crushing chamber volume. The volume of the frustum shaped hopper can be determined using Equation (1) as given by Olukunle (2016).

$$v_{hopper} = \frac{h}{3}\left(Area_{big} + Area_{small} + \sqrt{Area_{big} \times Area_{small}}\right) \quad (1)$$

Where v_{hopper} is the hopper volume, $Area_{big}$ is the area of the upper pyramid base, $Area_{small}$ is the area of the lower pyramid base. The pyramid bases are rectangular shaped.

The volume is determined as 0.036 m^3.

The shredding chamber is assumed to be filled to about two-third giving room for the blade assembly. The shredding chamber is rectangular shaped and the volume is obtained as 0.0405 m^3. The total volume of plastic to be shredded at a single operation is the total of volumes determined and is 0.0765 m^3.

The weight of HPDE plastic to be shredded w_{HDPE} is given by Equation (2) as provided by Olukunle (2016).

$$w_{HDPE} = v_t \times \rho_{HDPE} \times g \quad (2)$$

Where ρ_{HDPE} is the density of HDPE plastic (960 kg/m^3 (Khalaf, 2012)) and g, is acceleration due to gravity (9.81 m/s^2). Therefore, weight is 720.45 N.Assuming blade is not to shear relative to plastic (to be shredded) then the force required to shred must be greater than (equal to) the weight obtained (Sulaiman *et al*., 2017).

$$\text{Force}_{\text{shredding}} \geq \text{Force}_{\text{HDPE}}$$

Shredding force is determined to be $\geq$ 721 N

The blade torque, T_b is obtained according to Akash *et al*. (2019) using Equation (3).

$$T_b = \text{Force} \times \text{Perpendicular distance} \quad (3)$$

The blade length as shown in Figure (4) is the perpendicular distance.

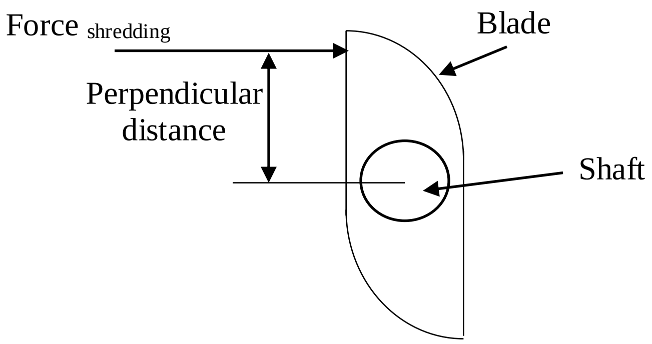

Figure 2: Shredding force acting on blade edge

Perpendicular distance and force are 0.075 m and 721 N respectively, the torque is obtained as 54.075 Nm. (Olukunle, 2016) provided the required shredding speed as 300 rpm, so the power required can be obtained using Equation (3) as provided by Khurmi and Gupta (2005).

$$P = \frac{2\pi N T_b}{60} \quad (3)$$

Where N is the shredding speed.

$$P = \frac{2\pi \times 300 \times 54.075}{60} = 1698.8W \text{ or } 2.28 \text{ hp}$$

The minimum required power to shred the plastic is 2.28 hp, but considerations must be given to the power required to drive the machine components.

2.1.3 Power Required for Driving Machine Components

The material considered for the blade and shaft is mild steel with density of 7860 kg/m^3 (Manik *et al.*, 2012). The blade is machined from a cylindrically shaped mild steel plate of radius 0.075 m and thickness of 0.004 m. The volume of a cylinder is given by Equation (4) (Barderas *et al.*, 2016).

$$V = \pi r^2 h \qquad (4)$$

Where r is the radius and h is the thickness (in this case). The volume is obtained as 7.07 × 10^{-5}m^3. The mass is obtained considering the density (7860 kg/m^3) and volume of the blade. The mass is therefore obtained as 0.56 kg. For 14-piece blade assembly, 0.56 × 14 = 7.84 kg. The total weight is 7.84 × 9.81 m/s^2 = 5.5 N

Using Equation (4) and radius 0.075 m the torque is 0.4125 Nm, and using Equation (3) the power can be obtained as 12.96 W or 0.017 hp. Adding both powers obtained gives 1698.8 + 12.96 = 1711.8 W or 2.3 hp.

Service factor of 1.5 is used given by Equation (5) as stated by Sulaiman *et al.* (2017).

Design power = Service factor × required power (5)

Design power = 1.5 × 1711.8 = 2567.7 W or 3.44 hp

The efficiency of an electric motor is given by Equation (6) (Sulaiman, *et al.*, 2017).

$$\eta_m = \frac{P_{out}}{P_{in}} \qquad (6)$$

Where P_{out} and P_{in} are powers input and output of the electric motor. For a 2.6 kW motor efficiency of 78 % (Yu *et al.*, 2011) is adopted.

$$P_{in} = \frac{2567.7}{0.78} = 3291.9 \text{ W or } 4.4 \text{ hp}$$

The power determined is 4.4 hp therefore a 5 hp motor is selected for the machine.

2.1.4 Belt Selection and Analysis

The V-belt drive is used in this design. It simplifies machine design, reduces cost and is highly efficient in use (Khurmi and Gupta, 2005). The A-type belt cross section is selected due to the 5 hp power motor rating (Khurmi and Gupta, 2005). The maximum tension T in the belt was determined as 218.4 N using Equation (12) as given by Khurmi and Gupta (2005).

$$T = \sigma.b.t \qquad (7)$$

The recommended minimum pulley diameter from Table (1) is 0.075 m. So, to maintain a speed of 300 rpm (Olukunle, 2016) the machine pulley is obtained using Equation (8) as stated by Khurmi and Gupta (2005).

$$N_1 D_1 = N_2 D_2 \qquad (8)$$

Where, N_1, N_2 are driver and driven pulley speeds and D_1, D_2 are driver and driven pulley diameters respectively. The electric motor speed is measured as 1400 rpm. So, the D_2 is 0.35 m. Tight and slack tensions T_1 and T_2 were obtained as 214.81 N and 10.2 N respectively using Equations (9) and (10) as given by Khurmi and Gupta (2005).

$$T_1 = T - T_c \qquad (9)$$

$$\frac{T_1}{T_2} = e^{\mu \theta_1 \operatorname{cosec} \beta} \qquad (10)$$

Belt length is determined according to Khurmi and Gupta, (2005) using Equation (11).

$$L_B = \frac{\pi}{2}(D_1 + D_2) + 2C + \left(\frac{D_1 - D_2}{4C}\right)^2 \quad (11)$$

2.1.5 Determination of Shaft Diameter

The diameter of a shaft can be determined from the American Society of Mechanical Engineers ASME design code as used by Egbe and Olugboji (2016).

$$d^3 = \frac{16}{\pi S_s}\sqrt{(Mk_b)^2 + (T_s k_t)^2} \quad (12)$$

S_s

where, is the shear stress, and it is taken as 42 MN/m^2. M and T are bending and twisting moments respectively. According to ASME design code: combined shock and fatigue bending (K_b) and torsion (K_t) factors for suddenly applied load, minor shock are 1.5-2 and 1-1.5 respectively (Egbe and Olugboji, 2016).The torque T_s is obtained as 15.3 Nmusing Equation (13) as given by Egbe and Olugboji (2016).

$$T_s = (T_1 - T_2) R \quad (13)$$

The bending moment is first obtained by ascertaining the total weight acting on the shaft, which was obtained as 721 + 5.5 = 726.5 N. this weight is considered to be uniformly distributed on the shaft as the blade distances are minimal. The forces acting on the shaft are depicted in Figure (3).

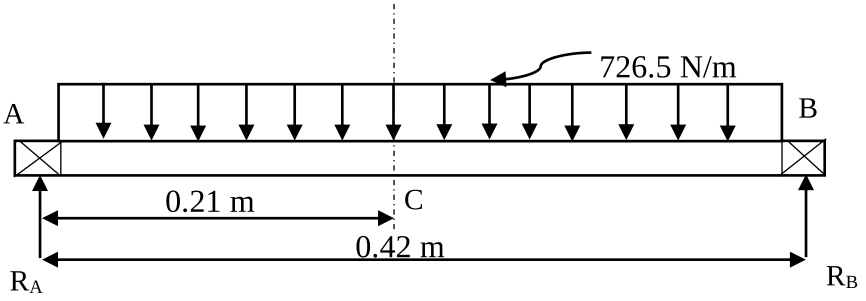

Figure 3: Free body diagram of forces acting on the shaft

Reactions at point A and B are given by Equation (14) as stated by Bansal (2010).

$$R_A = R_B = \frac{wL}{2} \quad (14)$$

Where R_A and R_B are reactions at point A and B, w is the load acting on shaft and L is the length of shaft. So, R_A and R_B are obtained as 152.6 N. The shear force at a point say 0.105 m is given by Equation (3.23) as derived by Bansal (2010).

$$F_{0.105} = +R_A - w(0.105) \quad (15)$$

$F_{0.105}$ becomes 76.32 N. Shear forces at point A, B and C are described in Equations (16), (17) and (18) as given by Bansal (2010).

$$F_A = +\frac{wL}{2} \quad (16)$$

$$F_B = -\frac{wL}{2} \quad (17)$$

$$F_C = 0 \quad (18)$$

Therefore, the shear forces at points A, B and C are 152.6, -152.6 and 0 N respectively. For the bending moment analysis, bending moment at a point say 0.105 m is obtained using Equation (19) as derived from Bansal (2010).

$$M_{0.105} = +R_A(0.105) - \frac{w(0.105)^2}{2} \quad (19)$$

$M_{0.105}$ = 16.023 – 4.0048 = 12.02 Nm

For points A and B their bending moments are 0 Nm and for C the bending moments is given by Equations (20) as derived from Bansal (2010). M_A and M_B are 0 Nm.

$$M_C = +\frac{wL^2}{8} \quad (20)$$

M_C = 16 Nm

The diameter of the shaft can be determined using bending moment, M = 16 Nm and twisting moment, T = 15.3 Nm. The K_b and K_t are selected as 1.5 and 1.2 as the shock on the shaft is minor.

$$d^3 = \frac{16}{\pi \times 42 \times 10^6}\sqrt{(16 \times 1.5)^2 + (15.3 \times 1.2)^2}$$

$$d^3 = 3.66 \times 10^{-6}$$

d = 0.0154 m or 15 mm

3 RESULTS AND DISCUSSION

The results of the analysis are presented in Table 2, while Figure 4 is shear force and bending moment diagrams for the shaft.

Table 2: Design Calculations

S/N	Equation Number	Parameter/Quantity	Values obtained
1.	1	Volume of hopper	0.036 m^3
2.	2	Wieght of plastic to be shreded	720.45 N
3.	3	Required power to shred HDPE	1698.8 W
4.	6	Power to drive machine	3291.9 W
5.	13	Shaft torque	15.3 Nm
6.	20	Shaft bending moment	16 Nm
7.	12	Shaft diameter	15 mm

The power required to shred plastic of mass 73 kg was determined to be 1698.8W with 1711.8 W required to drive the machine components that will shred the plastic inputs. The minimum power obtained to shred from this analysis is within the same range as that obtained by David and Joel (2018), which is 700 N, this strengthens the validity of the results obtained from the analysis. Due to the setup torque and moment value of 15.3 and 16 Nm were obtained respectively which relatively similar to that obtained by Reddy and Raju (2018).15 mm was obtained from the analysis as the shaft diameter, so two shafts of 25 mm diameter are selected for the machine from standard shaft dimensions provided by Khurmi and Gupta (2005). To drive the system succesfully a 5 hp motor has been selected as against the 4.4 hp (3291.9 W) in Table 2.

The behaviour represented in Figure 4 is typical for a uniformly distributed load as expected. The shear force extremes are at 152.6 N and -152.6 N respectively with completely positive bending moment values as represented in the Figure 4.

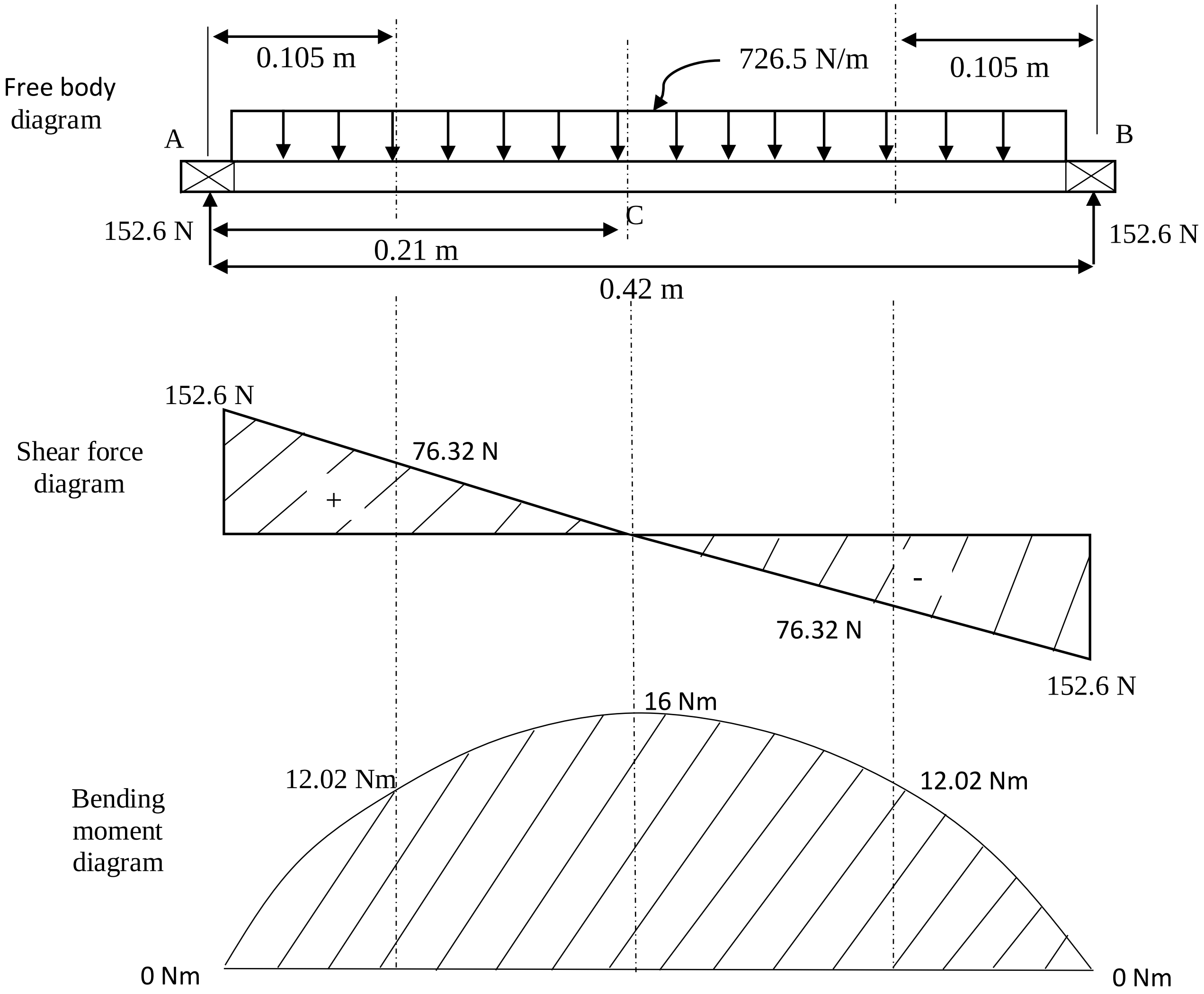

Figure 4: Shear force and bending moment diagrams for the shaft

4 CONCLUSIONS

Waste is naturally produced by all humans and possesses great health and environmental risks, with plastic and non-degradable materials constituting most of the waste disposed in the present day. The design analysis of a plastic shredding machine capable of shredding plastic of 73 kg was achieved in the analysis which is the aim of the paper. The major components that require efficient running of the machine have been accounted for in the analysis. Hopefully the analysis will be used for further study; this includes the fabrication and performance evaluation of the machine.

REFERENCES

Adepo, S. O. & Obanoyen, N. O. (2017). Design and construction of a plastic shredding machine. *Journal of Multidisciplinary Engineering Science and Technology (JMEST)*, 4(9), 8190-8194.

Akash, B., Christina, P., Drashan, K. & Manoj, S. (2019). Plastic waste management by mechanical shredder machine. *International Journal of Advance Research and Innovative Ideas in Education*, 3218-3223.

Al-Gheethi, A., Noman E., Jeremiah, D. B., Mohamed, R., Abdullah, A. H., Nagapan, S. & Hashim M., A. (2018). A review of potential factors contributing to epidemic cholera in Yemen. *Journal of Water Health.* , 16(5):667-680. doi: 10.2166/wh.2018.113.

Bansal, R. K. (2010). *A textbook of strength of materials.* New Delhi, India: Laxmi Publications.

Barderas, A. V., Stephania, B. S. & Rodea, G. (2016). How to calculate the volumes of partially full tanks. *International Journal of Research in Engineering and Technology*, 5(4), 1-7.

Canopoli, L., Coulon, F. & Wagland, S. T. (2019). Degradation of excavated polyethylene and polypropylene waste from landfill. *Science of The Total Environment*, 1-8.

Chinedu, I., Ezeibe, C., Anijiofor, S. C. & Daud, N. N. N. (2018). Solid waste management in nigeria: problems, prospects, and policies. *Journal of Solid Waste Technology and Management* , 44(2),163-172 .

David, A. & Joel, O. O. (2018). Design and construction of a plastic shredder machine for recycling and management of plastic wastes. *International Journal of Scientific and Engineering Research*, 9(5), 1379-1385.

Egbe, E. A. P., & Olugboji, O. A. (2016). Design, fabrication and testing of a double roll crusher.. *International Journal of Engineering Trends and Technology (IJETT)* , 35(11), 2231-5381.

Jadhav, N. D., Patil, A., Lokhande, H. & Turmabe, D. (2018). Development of plastic bottle shredding machine. *International Journal of Waste Resources*, 8(2),1-4.

Khalaf, M. N. (2012). Mechanical properties of filled high density polyethylene. *Journal of Saudi Chemical Society*, 19, 88-91.

Khurmi, R.S. & Gupta, J. K. (2005). *A textbook of machine design.* New Delhi, India: Eurasia Publishing House (Pvt.) Ltd.

Manik, A., Halder, P., Paul, N. & Rahman, S. (2012). Effect of welding on the properties of Mild steel & cast iron specimen . *International Conference on Mechanical, Industrial and Energy Engineering* , 1-5.

Olukunle, T. A. (2016). Design consideration of a plastic shredder in recycling processes. *International Journal of Mechanical, aeorospace, Industrial, Mechanical and Manufacturing Engineering*, 10(11), 1824-1827.

Reddy, S. & Raju, T. . (2018). Design and development of mini plastic shredder machine. *Materials Science and Engineering*, 1-6, doi:10.1088/1757-899X/455/1/012119.

Sulaiman, I., Egbe, E. A. P., Alkali, B., Kolo, Y. B. & Enock, O. I. (2017). Development of a horizontal shaft hammer mill. *2nd International Engineering Conference* (pp. 365-369). Minna: IEC2017.

VijayAnanth, S., Sureshkumar, T. N., Dhanasekaran, C. & Aravinth Kumar, A. (2018). Design and fabrication of plastic shredder machine for clean environment. *International Journal of Management, Technology And Engineering*, 8(12), 4601-4606.

ISSN 2121-2987

Journal of NIMechE Vol.10 No. 2, pp 42-56
Printed in Nigeria

Copyright@2022, The Nigerian Institution of Mechanical Engineers (A Division of Nigerian Society of Engineers)

EFFECTS OF OXIDIZED SUCROSE CROSS-LINKED CASSAVA STARCH FILM ON THE PHOTOVOLTAIC PROPERTIES OF PEROVSKITE SOLAR CELLS

J. Y. Jiya[1, 2], J. S. Enaburekhan[1], M. T. Jimoh[1], E. C. Egwim[3], I. A. Joseph[4]

[1]Department of Mechanical Engineering, Bayero University Kano.
[2]Department of Mechanical Engineering, Federal University of Technology, Minna.
[3]Centre for Genetic and Biotechnology Engineering, FUT, Minna, Niger state.
[4]Department of Chemical Engineering, Federal University of Technology, Minna, Niger state

ABSTRACT:

Despite rapid progress in the perovskite solar cell efficiency, there have been concerns about issues which could affect the measurement accuracy and/or practical applications of these devices, amongst which are stability, scaling up (large area devices), and possible environmental effects related to the use of lead-based active material. Based on the findings from previous studies, an optimized biodegradable oxidized sucrose cross-linked cassava starch film layer with zirconium oxide is introduced as a desiccant and buffer against damp heat and thermal recycling. This modified photovoltaic device is capable of resisting ingress of moisture at elevated temperatures, withstanding temperature cycling without delamination, and as such, enables efficient and stable operation. The layers in the PSC were modified by replacing the conventional metallic counter electrode with a low-cost carbon counter electrode. The PSC device with the control architecture underwent a more rapid degradation, particularly within the first 288 hours though with a higher PCE than the modified device. However, in contrast, the PSC device with the buffer layer only degraded a small amount. The best device maintained 95% of its initial efficiency after exposure for 550 hours.

Keywords: *Oxidized sucrose, films, Perovskite, current density, open circuit voltage, fill factor*

1.0 INTRODUCTION

Perovskite-based photovoltaics is still a nascent technology. However, the distinct properties of perovskites such as high absorption coefficient, tunable band gap, longer carrier diffusion length, and the rapid increase in efficiency, makes it a very interesting technology. A considerable amount of research is being carried out in this field. Solar cells used for power generation must possess certain characteristics like high efficiency, low cost of raw materials, simple fabrication technique, ease of solar panel installation, and long term stability. Unfortunately, there is not yet a device that can simultaneously meet all the above requirements. First and second generation solar cells have high efficiency and stability except for the amorphous silicon solar cells. However, they also possess some disadvantages. Majority of these solar cells employ high-efficiency silicon-based materials which are expensive. The scarcity of indium which is used in copper indium gallium silicon (CIGS) solar cells is a potential challenge for the widespread use of these cells. The toxicity of cadmium and the low earth abundance of tellurium are often regarded as the drawbacks of cadmium tellurium (CdTe) solar cells. In the recent years, research has focused on the development of cost-effective and feasible non-silicon solar cell technologies. The new (third) generation solar cells are primarily organic solar cells, dye sensitized solar cells (DSSCs), quantum dots, conjugated polymers, and perovskites (Figure 1).

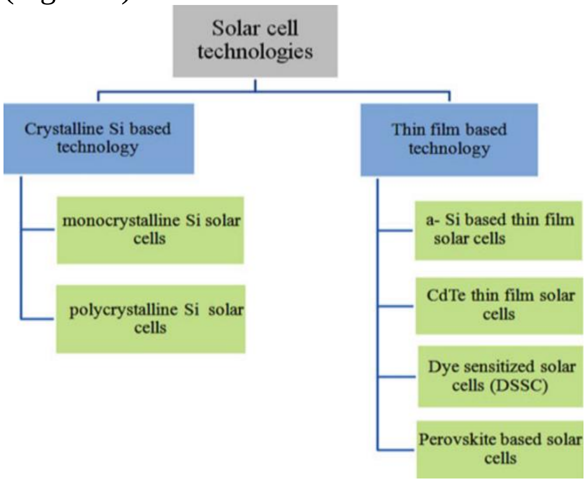

Fig.1: Classification of the Third Generation Solar Cell Technologies

The perovskite already gained much attention as a potential replacement of the silicon photovoltaic (PV) devices, which has still occupied the most dominant position in the current PV market. Its low-cost and convenient fabrication techniques also serve as the possible advantages over silicon-based devices that require complicated and costly high-vacuum deposition methods. Regardless of wide potentials, the technology of perovskite solar cell (PSC) still remains at an infant stage of becoming commercially viable in comparison to other existing solar technologies due to some limiting concerns. Of such limiting concerns or major problems are the problems of stability and the overall material cost. Current flexible PSCs use non-biodegradable, petroleum-based polymer substrates, hence, environmental pollution is aggravated due to inadequate recycling process. Therefore, developing a biodegradable and low-cost component will provide a great alternative to PSC substrates. This work therefore seeks to address the problem of instability of the device through interface modifications by incorporating a hydrophobic starch film oxide that will serve as a desiccant and buffer against ambient conditions (oxygen and humidity) which leads to degradation of PSCs.

Efficiency gain of the thin film solar cells greatly depends upon the quality and thickness of the buffer layer. The standard CIS solar cell needs optimized thickness of buffer layer between the absorber layer and the transparent front contact layer to improve efficiency. It drives out the photo generated carriers with minimal losses while coupling light to the junction with minimum absorption losses, yielding a highly efficient solar cell. Thin film heterojunction solar cells provide more light towards the junction as it has wide band gap buffer layer in contrast with optimal low bandgap absorber layer. This provides the most reliable way of increasing the efficiency of the cell. The beneficial effects of the buffer layer ranges from modifying the absorber surface chemistry to protecting the sensitive interface during the subsequent window deposition.

Starch is a natural desiccant which is readily available, cheap and biodegradable. The application of starch or starch derivatives as desiccants is not new in the industry: corn starch, corn grits, enzyme modified corn grits and other starch based materials have already been widely used as natural desiccants (Beery & Ladisch, 2001). These materials were found to be efficient and stable desiccants. Starch was also shown to selectively absorb water from ethanol/water vapor in fixed bed absorption systems (Móczó, Kun, & Fekete, 2018). Furthermore, mixing PLA with other biodegradable polymers like starch, cellulose or thermoplastic starch (TPS) might result in cost reduction.

2.0 EXPERIMENTAL SETUP

The methods adopted in this research are thus stated in accordance with the specific objectives of the research as presented in figure 2;

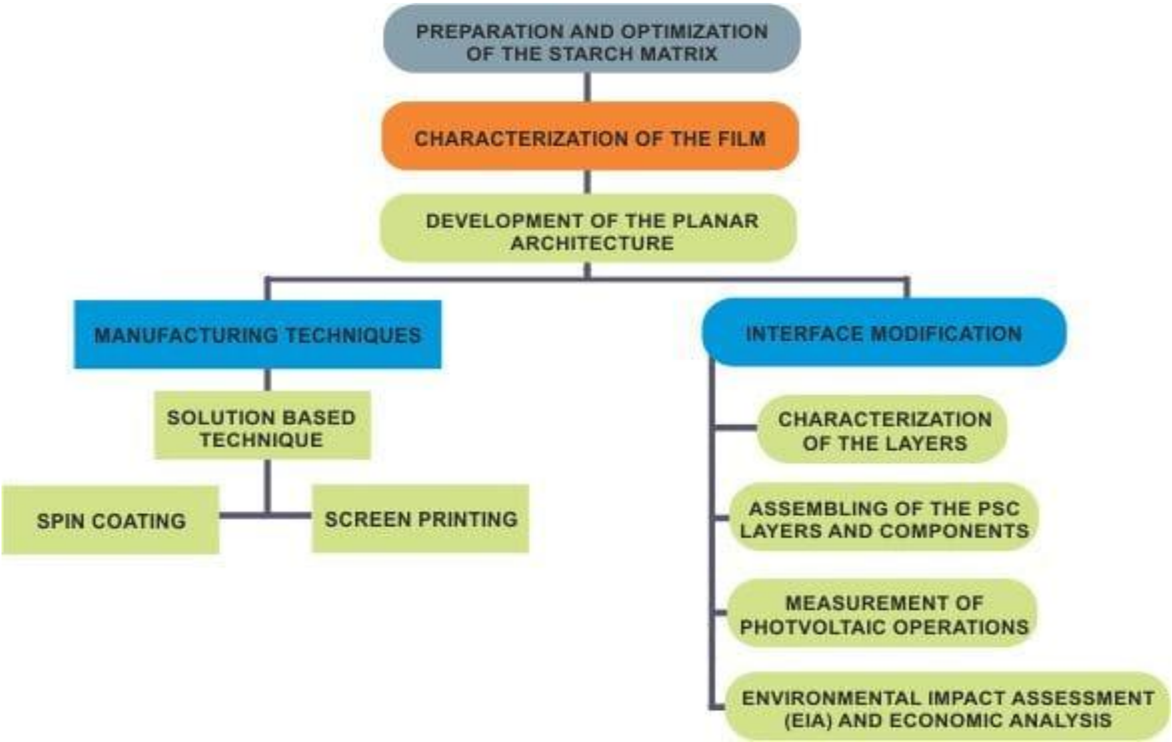

Figure 2: Experimental Process Setup for the fabrication of the PSC Device

Basically, for a larger band gap, the structure of this design is FTO/D-TiO_2/M-TiO_2/$MAPbI_3$/ZrO_2/Buffer layer/C which consists of the following layers as presented in figure 3; The Transparent conducting oxide (TCO) layer - a Fluorine doped tin oxide (FTO), the Electron transport layer (ETL) which consists of a dense and mesoporous titanium oxide, the Photo-active layer which is the Perovskite ($CH_3NH_3PbI_3$), Zirconium oxide with the buffer layer (oxidized-sucrose crosslinked starch film) and the Counter electrode layer (Carbon).

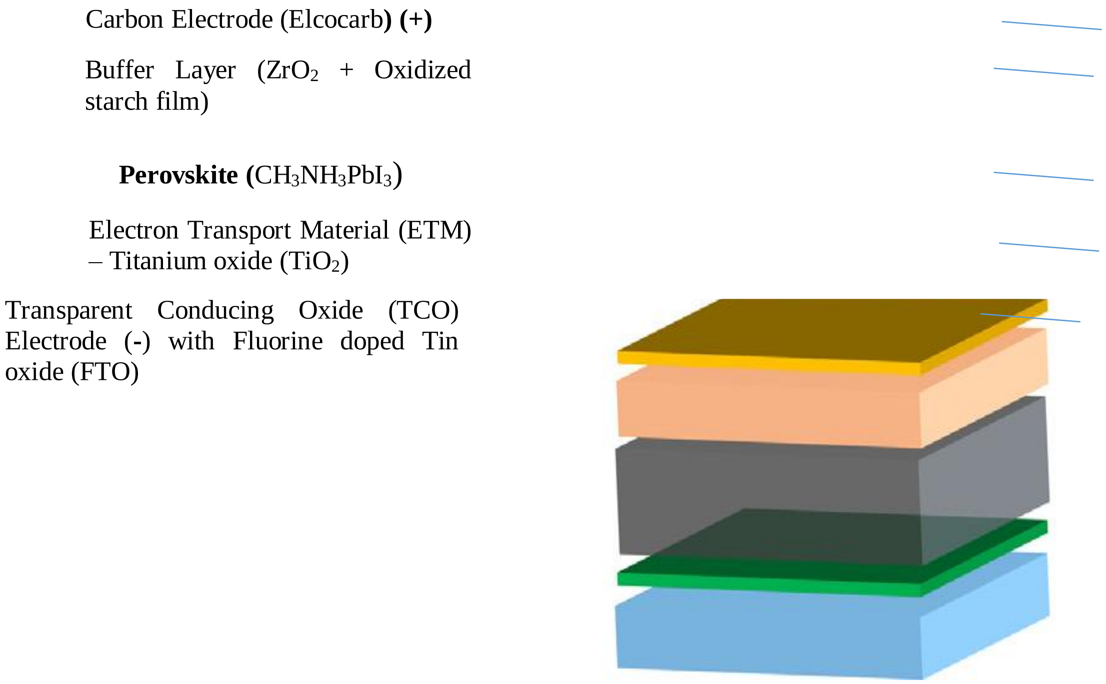

Figure 3: Planar Architecture of the PSC Device

The process of fabrication of the solar cell technically begins with the deposition of a compact TiO_2 hole-blocking layer on a fluorine-doped tin oxide (FTO) as represented in this study or an optional Indium Tin Oxide (ITO) substrate. This engages suitable deposition methods such as spin coating or spray pyrolysis (as used in this study) of 0.015 molar concentration of titanium di-isopropoxide-bis (acetyl-acetonate) upon preheated transparent conductive glass such as FTO at 350 ^{0}C for about 5 minutes and subsequent annealing at 500 ^{o}C for 30 Minutes. It is important to ensure that the compact layer is pinhole-free and uniform to prevent the recombination between carriers from the perovskite layers and FTO. On top of the compact layer, a meso-porous layer of n-type TiO_2 is formed by spin coating a nano-particle TiO_2 precursor solution followed by annealing to remove the polymeric binders (Seigo, 2015). The thickness and porosity of these layers can be modulated by changing the filler and solvent concentrations in the TiO_2 precursor solution. The perovskite films are then deposited on top of the n-type meso-porous layer by spin coating of precursor solution of perovskite prepared materials with N, N-dimethylformamide (DMF) and annealing at 150 ^{0}C (Miguel, et al., 2015). Finally, a carbon electrode is deposited to complete the solar cell as shown in figure 3

2.1 Cassava Starch Film Formation.

The starch film formation follows the under listed procedures;

(a) Process of Film Formation

There are various biomaterial film forming processes such as casting, spraying, extrusion and thermo-molding. The most common process to produce films on a laboratory scale is casting, which is used to produce free films for testing. In this process, a film forming solution is cast on a non-adhesive surface. Water or solvent is evaporated from the solution in order to form the film (Anker, Stading, & Hermansson, 2010). As a result of solvent evaporation, biopolymer increases with the result that hydrogen bonds are formed and basic film structure is created. Environmental properties, such as temperature and air relative humidity, during the evaporation stage could be used to control some of the film properties (Kawahara, et al., 2013).

In the spraying process a film forming solution is sprayed onto a surface of product on which droplets formed by a sprayer form uniform films. In spraying, solvent evaporates to some extent after leaving the nozzle of the sprayer allowing a shorter drying time for coating. Even if film formation occurs in a different way in casting and spraying processes the same starch-based film forming solution could be used in casting and spraying. Continuous film forming can be carried out using extrusion which is widely used to produce synthetic polymer films. Extrusion has been used to produce films or sheets from starch. In thermo-molding film forming materials, which are mixed with blender or extruder, are pressed between two heated plates to obtain films.

A starch film forming solution is prepared by heating to gelatinize starch in excess water in which plasticizer is added before gelatinization or after gelatinization into the hot solution (95°C). In some studies film forming suspension containing native starch, amylose, amylopectin or mixture of amylose and amylopectin is heated in a pressurized vessel to complete amylose and amylopectin leaching into the solution (Rindlav-Westling, Stading, & Gatenholm, 2002). After gelatinization, the film forming solution is poured onto a non-adhesive plate, such as polytetrafluoroethylene (teflon^R). Water is evaporated from the film forming solution to obtain films at various conditions, such as at the room temperature or in an oven at elevated temperatures. These different drying conditions affect film properties because of different setting times of biopolymers. The longer the film formation takes, the longer time there is for a film component to phase separate and crystallize.

The starch film was prepared by measuring 50 ml of distilled water into a 250 ml beaker and heating on a hotplate magnetic stirrer until the temperature reaches 50 ^{0}C. 3g of cassava starch was measured into the beaker and the temperature was allowed to attain 70 ^{0}C before 0.5 ml of Hydrogen peroxide, H_2O_2 was added for bleaching to improve the transparency, 0. 5 ml of the oxidized sucrose was added for cross-linking and further oxidation. 1.2 ml of glycerol was added to improve the plasticity. The solution was then subjected to drying to achieve the desired film.

2.1 Perovskite Solar Cell Device Characterization Technique

The performance of the PSC is mainly characterized by parameters such as incident photon to current efficiency (IPCE), short circuit photocurrent density (J_{sc}), open circuit photovoltage (V_{oc}), the fill factor (FF) and the overall efficiency of the photovoltaic cell (η).

Short Circuit Photocurrent Density (J_{sc})

The short-circuit current density is the maximum photo-generated current delivered by a solar cell when the terminals of the solar cell are in contact with each other (i.e. short-circuited). J_{sc} is the photocurrent per unit area (mA/cm^2) when an illuminated cell is short circuited where the external output voltage is zero. It depends on several factors such as the light intensity, light absorption, injection efficiency, regeneration of the oxidized dye, and the efficiency of charge transport in the TiO_2 film to the counter electrode. It is strongly related to the IPCE and theoretical values of the J_{sc} can be calculated from integrated sum of IPCE measure over the entire solar spectrum**.**

$$J_{sc} = \int_0^\infty \mathrm{IPCE}(\lambda).I_{sun}(\lambda)\mathrm{d}\lambda \qquad (1)$$

$$J_{sc} = J(V) + J_o\left(e^{qv/mK_BT^{-1}}\right) \qquad (2)$$

Where V is the voltage across the junction, T is the absolute temperature, J_o is the dark saturation current density and m is the ideality factor with values between 1 and 2. The electric charge $q = 1.603 \times 10^{-19} C$ and the Boltzmann's constant, $K_B = 1.38 \times 10^{-23} JK^{-1}$

Open Circuit Photovoltage (V_{oc}**)**

V_{oc} is measured when the circuit is open or no external load is connected. Under this condition, there is no external current flows between the two terminals i.e. I = 0 and V = V_{oc}. It depends on both the Fermi level of the semiconductor and the level of dark current. It is the maximum voltage that a solar cell can deliver. The theoretical maximum of the V_{oc} of the cell is determined by the difference between the Fermi level of the semiconductor and the redox potential of the electrolyte. The V_{oc} depends on the photogenerated current density J_{ph},

$$V_{oc} = \frac{mK_BT}{q}\ln\left(\frac{J_{ph}}{J_o} + 1\right) \qquad (3)$$

Optimum Voltage (V_m**)**

V_m is the voltage at the optimum operating point at which the PSC output power is maximum.

Optimum Current (J_m**)**

The value of J_m gives the maximum photocurrent obtainable at maximum power point.

Output Power (P_{out}**)**

For a given bias voltage the output power of the cell is the product of the measured current density and the bias voltage

$$P_{out} = V.\,J \qquad (4)$$

P_{out} generally increases when V is increased from zero, goes through a maximum and decreases to zero at V = V_{oc}. The maximum power point Pm is the product of J_m and V_m

Fill Factor (FF)

Fill factor is a parameter related to the maximum power point and is often described as a measure of the "squareness" of the J-V curve and describes the degree to which the voltage at the maximum power point (V_m) matches V_{oc} and that the current at the maximum power point (J_m) matches J_{sc}. Its value is determined by the ratio of the maximum power (V_mJ_m) to the maximum power attainable by the solar cell ($J_{sc}V_{oc}$), with a value between 0 and 1.

$$FF = \frac{V_mJ_m}{J_{sc}V_{oc}} \qquad (5)$$

Solar Energy to Electricity Conversion Efficiency (η)

The overall solar energy to electric power conversion efficiency (η), the key parameter of the device, measures how much power is converted by the cell in comparison to the amount of absorbed light that reaches the device. It is given by the ratio of the maximum output power (V_mJ_m) to the incident solar power (P_{in}). The overall sunlight to electric power conversion efficiency of a DSC is given by the following expression

$$\eta = \frac{P_m}{P_{in}} = \frac{J_{sc}V_{oc}FF}{P_{in}} \quad (6)$$

3.0 RESULTS

3.1 Transparency of the Starch

Table 1: Changes in Transparency of the Films at Various Hours and Intervals of 24 hours

	Process parameters			Exposure Time (Hours)					
				0	24	48	72	96	120
S/N	Temperature (^0C)	Time (Mins)	Amount of Glycerol (ml)	Degree of Transparency (%)					
1	70	5	0	95.544	76.826	0	0	0	0
2	83	12	0.8	98.558	86.998	0	0	0	0
3	90	10	0.5	96.917	91.759	90.205	88.412	88.197	0
4	80	5	0.5	98.558	91.23	54.291	0	0	0
5	80	15	0.5	97.169	91.23	81.677	0	0	0

Five different oxidized starch films were produced at different conditions of temperature, time and amount of glycerol. The oxidized sucrose and hydrogen peroxide were kept constant due to almost fixed point effects during the preliminary experiment on the starch modification in this study as shown on table 1. For industrial application of cassava starch film where transparency is important, sample three is considered to be the best due to its ability to retain high percentage of it transparency up to 96 hours in water, however, previous studies failed to examined this important property of starch film

3.2 Water Absorption Analysis

Table 2: Weight Variation of the Films at Various Hours and Intervals of 24 Hours

	Process parameters			Exposure Time (Hours)				
				24	48	72	96	120
S/N	Temperature (^oC)	Time (Min)	Amount of Glycerol (ml)	Degree of weight lost (%)				
1	70	5	0	4.375	-	-	-	-
2	83	12	0.8	50	-	-	-	-
3	90	10	0.5	14.38	23.28	31.5	52.05	0

4	80	5	0.5	42.85	61.9	-	-	-
5	80	15	0.5	18.18	30	-	-	-

The water absorption analysis was carried out in order to determine the extent to which the film material can retain its properties before it completely dissolves in water. This can also be used to determine its area of application. The results on Table 2 shows that sample 1 has the least percentage weight loss of 4.38 % at 24 hours immersion in water, on further immersion in water material completely dissolved in less than 48 hours. The result of sample three is of utmost interest as it experience only 14.38 % at 24 hours immersion in water, 23.28 % weight loss at 48 hours, 31.5 % weight loss at 72 hours in water and 52.05 % weight loss in water at 96 hours. The ability of sample three to retain high proportion of it weight in water over a long period could be attributed to the overall contributory effect of oxidized sucrose, hydrogen peroxide and glycerol as well as the high reaction temperature (90 ^{o}C) which enhanced the proper bonding of the starch film. Pawinee and Natchanan (2019) reported that the water solubility of cassava starch film modified with glycerol ranges from 10 to 36 % in 24 hours of water immersion. This shows that there is significant improvement in the water solubility of the oxidized cassava starch film produced in this study and that it can be recommended for use where water solubility is less desired in starch film.

3.3 Mechanical Properties of the Film

Table 3: Mechanical Properties of the Starch film Sample

S/N	Sample Code	Tensile Strength (MPa)	Elongation (%)
1	Sample 6	25.57	8.01 ± 103
2	Sample 9	21.51	6.95 ± 1.21
3	Sample 10	29.00	7.40 ± 0.52
4	Sample C	42.13	1.27 ± 0.23
5	Sample O	14.47	10.87 ± 1.61

The structural and mechanical starch behavior of the glycerol plasticized, sucrose-oxidized cassava starch film was investigated as shown on Table 3. From the results, it can be inferred that the tensile strength and elongation of the films are greatly influenced by the concentration of glycerol as plasticizer. Pure cassava starch film (sample C) without glycerol as plasticizer cured in 5 mins at a temperature of 70^0C had a tensile strength and elongation of 42.13 MPa and 1.27±0.23% respectively. Sample O which had a glycerol concentration of 0.8 ml, cured in 12 minutes at a temperature of 83^0C had tensile strength and elongation of 14.47 MPa and 10.87 ±1.61% respectively, Samples 6, 9 and 10 with curing times 10 mins, 5 mins and 15 mins and temperatures of 90^0C, 80^0C and 80^0C respectively had tensile strengths of 25.57, 21.51 and 29.00 MPa respectively. Cross-linked starch films have superior properties such as high mechanical and thermal properties, high water stability, resistance to high temperature and low pH, due to the stronger structure compared to films from pure native starches. Tensile strength and Elongation increases with increase in glycerol concentration to a certain point. At lower concentration, glycerol concentration has no significant effect on the tensile strength and elongation of the film since it couldn't sufficiently break enough hydrogen bonds to allow the flexibility of the cross-linked films. However, a higher amount of glycerol concentration leads to the breaking of more bonds creating wider space between two chains thereby decreasing the tensile strength. Hence, the optimum tensile strength and elongation can be attained with glycerol concentration of 0.5 ml at 5 – 10 minutes curing time which agrees with the reports of Helan et al., (2015). Using plasticizers with cross-linkers yield stronger cross-links with less hydroxyl group, which provide them higher strength with higher elongation as reported by (Helan, Hazal, Bignan, & Yiqi, 2015). Thus, plasticizer addition overcomes film brittleness caused by high intermolecular forces and provides flexibility to the starch films.

3.4 Characterization and Validation of the Photovoltaic Operation of the Device using Standard Measurement Techniques.

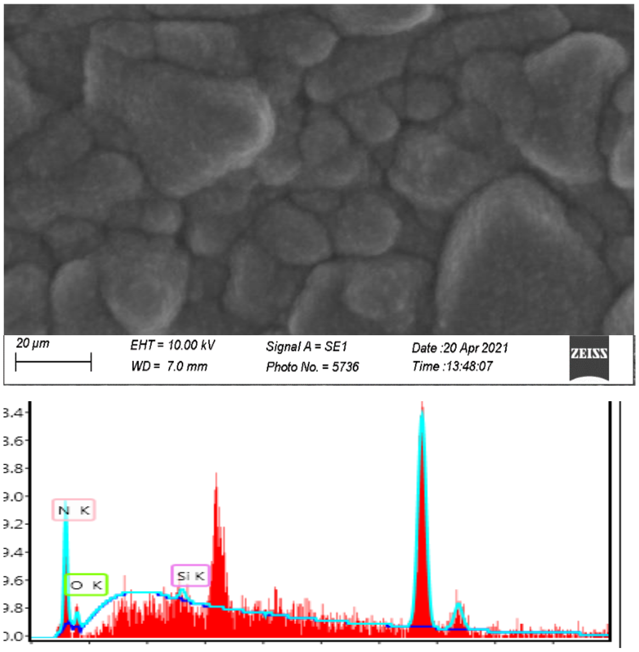

Figure 4: SEM and EDS Image of Dense TiO_2 Layer

One difficult step in the manufacture parts was the compact TiO_2 layer. Because the goal was to get a compact film that minimize recombination by preventing holes. Furthermore the film needs to be thin to minimize series resistance. To get it right required a lot of trial and error by experimenting with the parameters used for spray pyrolysis to find optimal thickness and compactness. If the layer is not compact enough, pinholes will be seen in the surface as small dark dots. The result of pinholes is that the holes are not blocked properly. No pinholes can be seen in the figure which means it is compact enough.

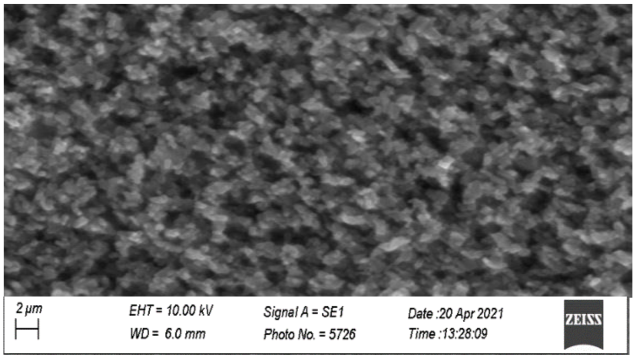

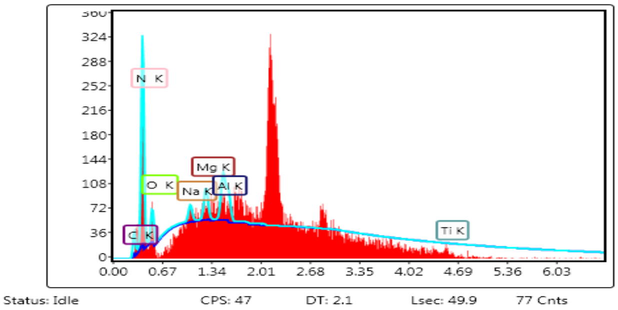

Figure 5: SEM and EDS Image of Mesoporous TiO_2 Layer

Figure 5 shows the mesoporous TiO_2 layer that is covering the FTO topography structure with a dense crystalline TiO_2.The mesoporous TiO_2 change the topographic surface structure with its small crystals with grain size of 10-20 nm. Large heights variations exist in this layer, which can be seen by the dark holes that can be interpreted as pinholes. In this layer pinholes are of no concern due to the compact TiO_2 layer underneath it. Figures 6 and & shows the SEM and EDS images of the ZrO_2 and carbon layers respectively, the images show the suitability of the layers since they maintained a pinhole-free structure required by the PSC devices.

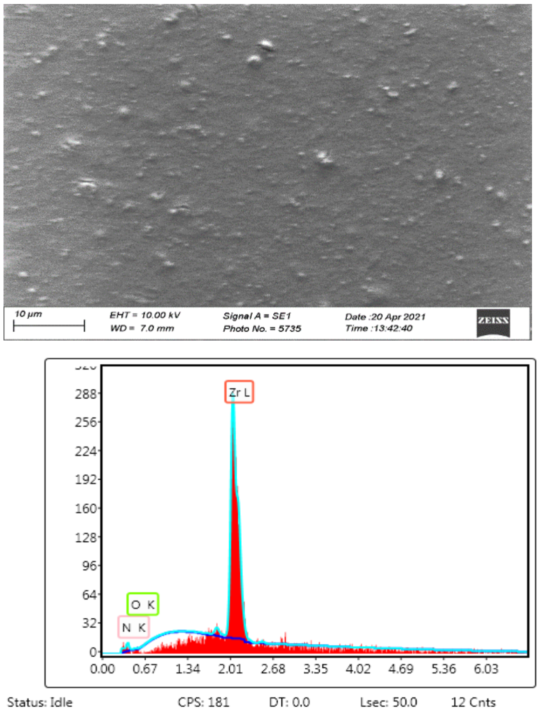

Figure 6: SEM and EDS Image of Zirconium oxide Layer

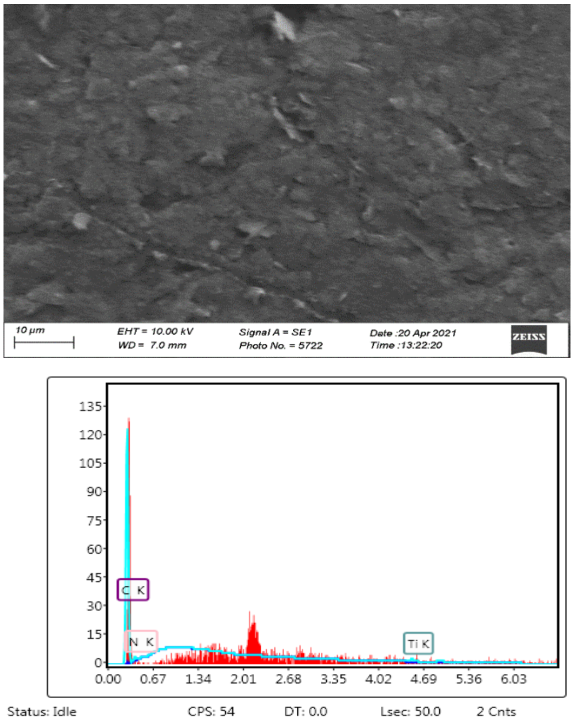

Figure 7: SEM and EDS Image of Carbon Layer (Elcocarb)

3.4.1 UV Spectrophotometry

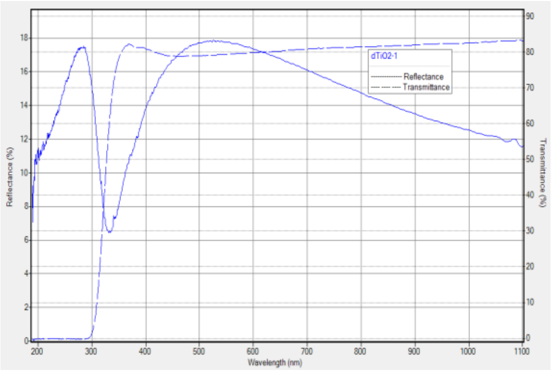

Figure 8: Reflectance and Transmittance Spectra of the Dense TiO_2 Interface

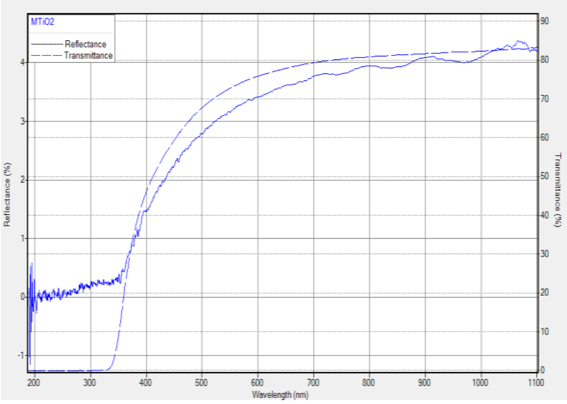

Figure 9: Reflectance and Transmittance Spectra of the Mesoporous TiO_2 Interface

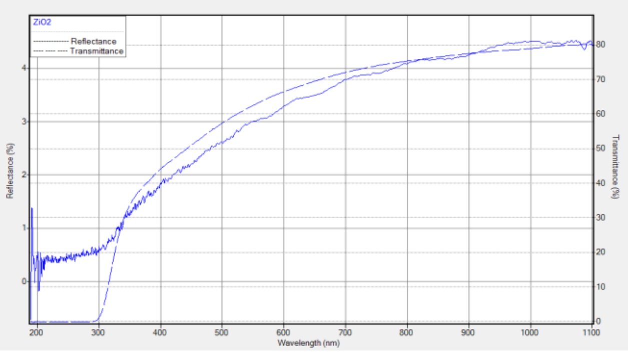

Figure 10: Reflectance and Transmittance Spectra of the Zirconium Layer

The Absorbance of the PSC is shown in figure 12. The absorbance value compares favorably with reported literatures.

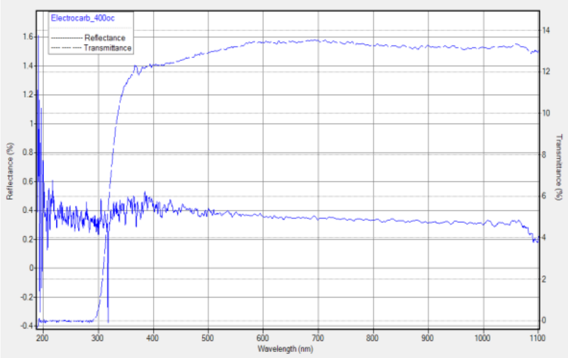

Figure 11: Reflectance and Transmittance Spectra of the Carbon Interface

The UV spectrophotometry of the PSC device layers were measured as shown in figures 8, 9, 10 and 11 respectively. The various layers presented relatively good Reflectance and Transmittance values with respect to the wavelengths.

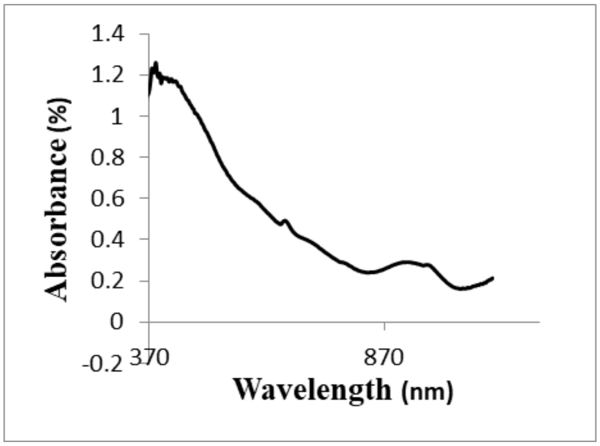

Figure 12: Absorption for Perovskite Interface

Optical absorption measurements were taken in order to monitor the band edge transition of the perovskite films formed. Figure 13 shows the absorbance of the different PSC layers, perovskite film that was fabricated from PbI_2 did not show any remarkable absorption, refer to figure 12.

The absorption shoulder, which is evident at 750 nm, is as a result of the direct gap transition from the first valence band maximum to the conduction band minimum

(Xu et al., 2016). The strong light harvesting capacity could be as a result of the quality of the perovskite crystals fabricated (Li Cong et al., 2017). The result shows that lead is a good precursor in fabricating perovskite as it has a stronger light absorbance capacity.

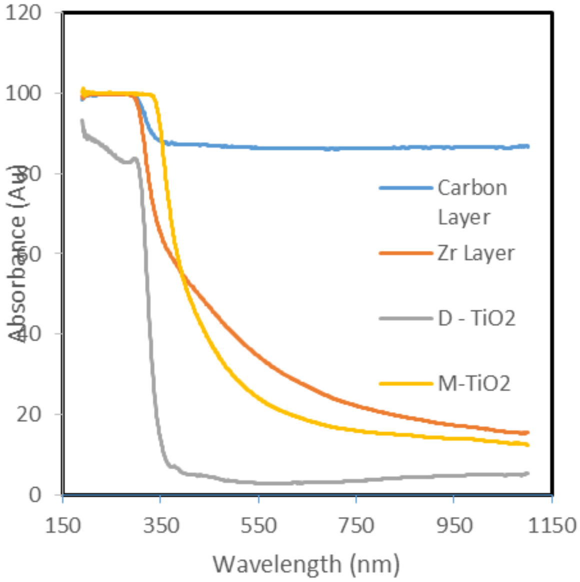

Figure 13: Absorption of each interface of the PSC in function of the part of light which reach it.

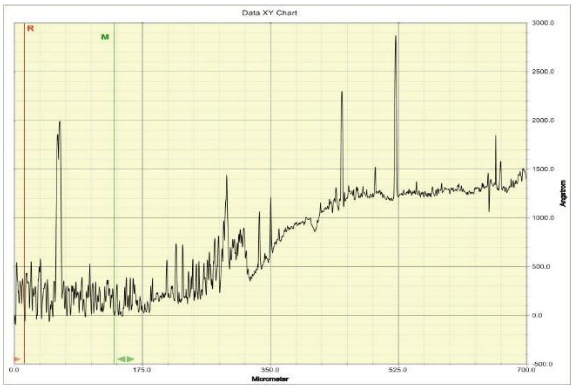

Figure 14: Profilometry of Densed TiO_2 Layer

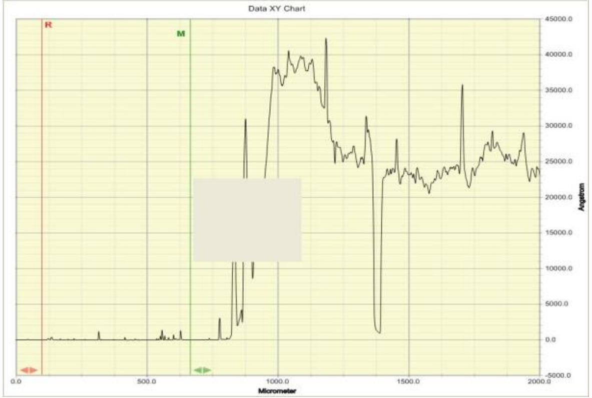

Figure 15: Profilometry of Mesoporous TiO_2 Layer

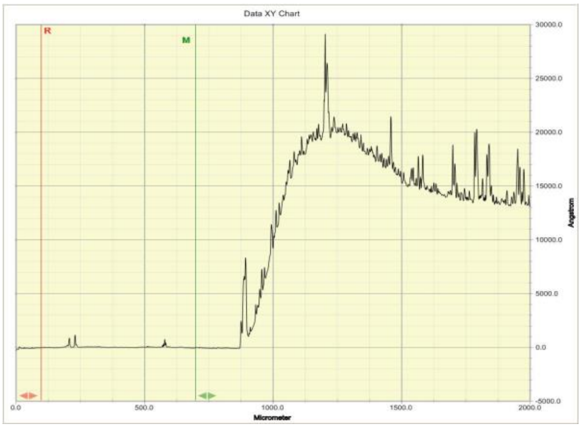

Figure 16: Profilometry of Zirconium Layer

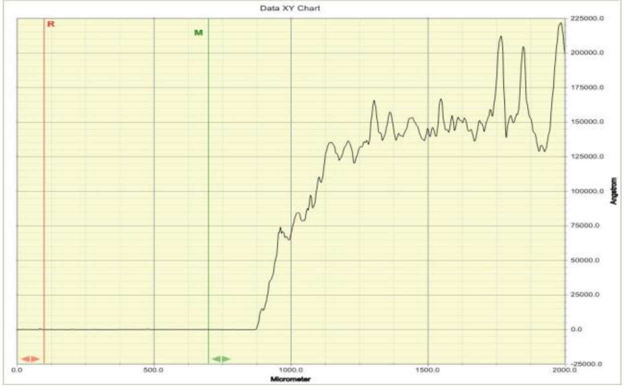

Figure 17: Profilometry of Carbon Layer

The profilometry of the various layers are shown in figures 14, 15, 16, 17.

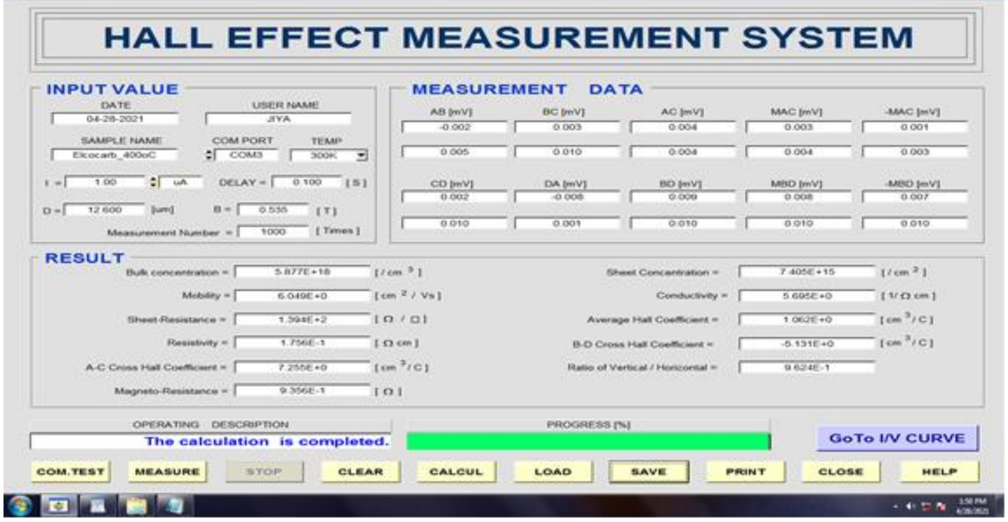

INPUT VALUE

DATE: 04-28-2021
USER NAME: JIYA
SAMPLE NAME: Ekocarb_400oC
COM PORT: COM3
TEMP: 300K
I = 1.00 uA
DELAY = 0.100 [S]
D = 12.600 [um]
B = 0.535 [T]
Measurement Number = 1000 [Times]

MEASUREMENT DATA

AB [mV]	BC [mV]	AC [mV]	MAC [mV]	-MAC [mV]
-0.002	0.003	0.004	0.003	0.001
0.005	0.010	0.004	0.004	0.003

CD [mV]	DA [mV]	BD [mV]	MBD [mV]	-MBD [mV]
0.002	-0.008	0.009	0.008	0.007
0.010	0.001	0.010	0.010	0.010

RESULT

Bulk concentration = 5.877E+16 [/ cm ^{3}]
Mobility = 6.049E+0 [cm ^{2} / Vs]
Sheet-Resistance = 1.394E+2 [Ω / □]
Resistivity = 1.756E-1 [Ω cm]
A-C Cross Hall Coefficient = 7.255E+0 [cm ^{3}/ C]
Magneto-Resistance = 9.356E-1 [Ω]
Sheet Concentration = 7.405E+15 [/ cm ^{2}]
Conductivity = 5.695E+0 [1/ Ω cm]
Average Hall Coefficient = 1.062E+0 [cm ^{3}/ C]
B-D Cross Hall Coefficient = -5.131E+0 [cm ^{3}/ C]
Ratio of Vertical / Horizontal = 9.624E-1

OPERATING DESCRIPTION: The calculation is completed.

Figure 18: Hall Effects for the Carbon Layer

The Hall effects measurement is shown in figure 18. The measurements compare favorably with reported literatures.

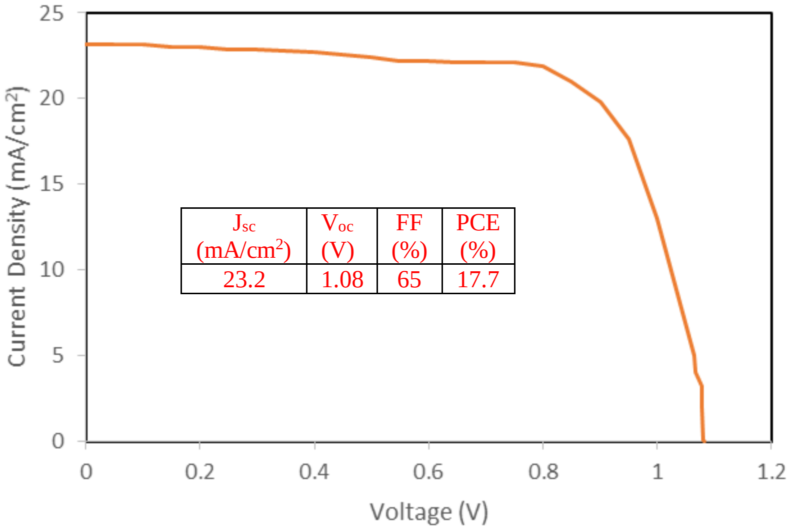

J_{sc} (mA/cm^2)	V_{oc} (V)	FF (%)	PCE (%)
23.2	1.08	65	17.7

Figure 19: J-V curve of the PSC device with the control architecture measured under a simulated AM 1.5 Solar radiation

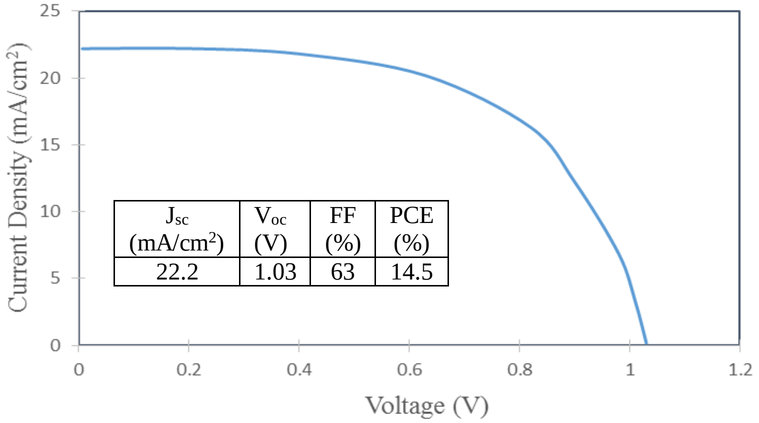

J_{sc} (mA/cm²)	V_{oc} (V)	FF (%)	PCE (%)
22.2	1.03	63	14.5

Figure 20: J-V Curve of the modified PSC with oxidized sucrose cross-linked cassava starch measured under a simulated AM 1.5 Solar radiation

The effect of the oxidized starch film is shown in figure 19. The buffer layer allows for a reduction in the thickness or total removal of the HTM layer. This caused a reduction in series resistance, thus improving FF (Wang et al., 2016). The stability of the control PSC device and the device including the sucrose-oxidized cassava starch film as a buffer layer was also measured. Devices were fabricated and encapsulated in a nitrogen-filled glove box using an epoxy resin and exposed to simulated full sunlight. The PSC device with the control architecture (figure 19) underwent a more rapid degradation, particularly within the first 288 hours though with a higher PCE than the modified device. However, in contrast, the PSC device with the buffer layer only degraded a small amount. The best device maintained 95% of its initial efficiency after exposure for 550 hours (figure 20).

4.0 CONCLUSION

PSCs tend to degrade when light is soaked under AM1.5 G sunlight, leading to a decrease in efficiency which follows the pattern of decreasing J_{SC}. The presence of TiO_2, which is photo-catalytically active for the UV light and exposure to high temperatures were found to be the reasons for the degradation. The degradation was not induced by moisture or UV radiation, but by the migration of metal from the top contact to the Perovskite layer. The buffer layer stopped the movement of metal to the perovskite absorber as purported by Asghar et al., (2017)

5.0 REFERENCES

Anker, M., Stading, M., & Hermansson, A. M. (2010). Aging of whey protein films and the effect of Mechanical and Barrier Properties. *Journal of Agricultural and Food processing*, *49*(2), 989-995.

Asghar, M. I., Zhang, J., Wang, H., & Lund, P. D. (2017). Device stability of perovskite solar cells – A review. *Renewable and Sustainable Energy Reviews*, 131-146.

Beery, K. E., & Ladisch, M. R. (2001). Chemistry and properties of Starch based Desiccant. *Enzyme and Microbial Technology* , 573-81.

Helan, X., Hazal, C., Bignan, M., & Yiqi, Y. (2015). Robust and Flexible Films from 100% Starch Crosslinked by Biobased Disaccharide Derivative. *ACS Sustainable Chem. Eng., 3,* 2631-2639.

Kawahara, M., Mizutani, K., Suzuki, S., Kitamura, S., Fukada, H., Yui, T., & Ogawa, K. (2013). Dependence of the Mechanical properties of a Pollulan film on the preparation temperature. *Bioscience, Biotechnology and Biochemistry, 67*(4), 893-895.

Miguel, A., Gabriel, L., Mauricio, E. C., Wei, Z., Michael, B. J., Henry, J. S., & Hernán, M. (2015). Optical Description of Mesostructured Organic−Inorganic Halide Perovskite Solar Cells. *J. Phys. Chem. Lett, 6*, 48-53.

Móczó, J., Kun, D., & Fekete, E. (2018). Desiccant Effect of Starch in Polylactic Composites. *eXPRESS Polymer Letter, 12*(11), 1014-1024.

Rindlav-Westling, A., Stading, M., & Gatenholm, P. (2002). Crystallinity and Morphology in Films of Starch, Amylose and Amylopectin Blends. *Biomacromolecules, 3*(1), 84-91.

Seigo, I. (2015). Printable solar cells . *WIREs Energy Environ 4,*, 51-73.

Wang, D., Wright, M., Elumalai, N. K., & Uddin, A. (2016). Stability of perovskite solar cells. *Solar Energy Materials and Solar Cells*, 255-275.

ISSN 2121-2987

Journal of NIMechE Vol.10 No. 2, pp 57-61
Printed in Nigeria

Copyright@2022, The Nigerian Institution of Mechanical Engineers (A Division of Nigerian Society of Engineers)

DEVELOPMENT OF AN UPDRAFT GASIFIER FOR ONYEAMA COAL

A.J Agabi[1a], A.Nasir[1] , O. J. Okegbile[1] , A.S. Kovo[2] , A.B. Garba[1]

[1] Department of Mechanical Engineering, Federal University of Technology, Minna,

[2] Department of Chemical Engineering, Federal University of Technology, Minna

[a] Email: nimilen@yahoo.com

ABSTRACT

The design and MATLAB simulation of the operating parameter of Onyeama coal in an updraft gasifier was investigated. The operating parameters considered are: power rating, air required, fuel consumption, hopper volume, time, reactor diameter and height. These results show that there exist a linear relationship of all the operating parameter with the power rating. It can be deduced that the sizing of the updraft (diameter and height) increased commensurately to increase in the power rating requirement and the operational time respectively. The lower values of the power rating obtained for the reactors diameter is a function of the coals heating value as well as the power rating requirement. The power rating should not be more than 700KW to obtain the optimal fuel consumption requirement. It can be established that onyeama coal proved to be more conservative in terms of the amount of coal that would be required for a particular rating.

Keywords: Operating parameter, MATLAB, onyeama coal and simulation

1.0 INTRODUCTION

Energy and good healthy condition has been reported to be the most significant aspect of life necessary for the societies (Vikrant and Argawal, 2019). The global need of energy sources such as crude oil, coal and natural gas with 33.28%, 28.11% and 24.13% in ranking has been reported in 2016 as the highest energy sources consumed globally, (Shakorfow, 2016) (Chukwu et al., 2016). Among the three sources of energy, coal is the cheapest and least expensive as compared with crude oil and natural gas that power generation. The design of any gasifier is usually accomplished with many assumptions in operating parameter, kinetic and thermodynamic effect that affect the gasification of the coal (Akanksha et al., 2018). These factors vary from one coal source to another. Another factor mentioned are depleting (Shakorfow, 2016). It is clear that research into coal as a fuel is not only timely but important at this period in the world energy sources (Shakorfow, 2016) (Akanksha et al., 2018). However the use of coal as an energy source is always accompanied with higher emission of carbon monoxide and carbon dioxide (Vikrant and Argawal, 2019). The design of gasifier is one of the greater factors in the development of a gasifier for the gasification of coal for

is the operating parameter and has been reported as the most significant factor that affects the successful operation of coal gasification (Akanksha et al., 2018). In this present work, the design and simulation of the operating parameter of an updraft gasifier for Onyeama coal is studied.

2.0 MATERIALS AND METHOD

The power requirement of a gasifier is determined by the fuel consumption rate which is empirically the amount of fuel (coal) that must be burnt per specific time in order to achieve the required amount of power of the gasifier. The size of the reactor is a function of the diameter of the cross-section of the cylinder where the fuel is being burnt. This is generally a function of the amount of the fuel consumed per unit time (FCR) to the specific gasification rate (SGR) of the fuel. The height of the gasifier which plays an important role in the performance of the gasifier is the total distance from the top and the bottom end of the reactor. This determines how long the gasifier would be operated in one loading of fuel. Basically, it is a function of a number of variables such as the required time to operate the gasifier (t), the specific gasification rate (SGR), and the density of the fuel.

2.1 Model Formulation Concept

The updraft coal gasifier was designed using relevant design equations and criteria as shown in Table 2. MATLAB software is used in determining the operating parameter using Onyeama coal with composition displayed in Table 1. The model equations were adopted from the work of Hong et al (2009). The core essence of the simulation was to see the trend in the design sizing of the system if the **power requirements, reaction times as well as the inherent coal were not constant**. Hence the simulation graphs will give an outline for knowing what the system sizing will be if any parameter is selected within the range of the three design factors as (i.e. power requirements, reaction times as well as the inherent coals).

Table 1: Composition of Onyeama coal

Proximate analysis		Ultimate analysis	
Moisture %	5.87	H%	3.8
Volatile matter	29.61	C%	86.55
Fixed carbon	63.61	N%	1.2
Ash	1.25	S%	0.6
Calorific value	33.33	ASH	1.25

(Source: Chukwu et al., 2016)

2.2 Design Requirements

Table 2 Design Parameters and their deductions

Design Parameters	Symbols	Formula	Values	Units
Fuel Consumption Rate	$\dot{m}_f$	$FCR = \dot{m}_f = \frac{\text{Power Required}}{LCV \times \eta_{thermal}}$	108.36	Kg/hr
Diameter of Reactor	D_r	$D_r = \left(\frac{4 \times \dot{m}_f}{SGR \times \pi}\right)^{0.5}$	630	Mm
Height of Reactor	H_r	$H_r = 1.4 \times \left(\frac{SGR \times t}{\rho_f}\right)$	1460	Mm
Power Required	P	$P = m_f \times L\dot{C}V \times \eta_{thermal}$	5	kW

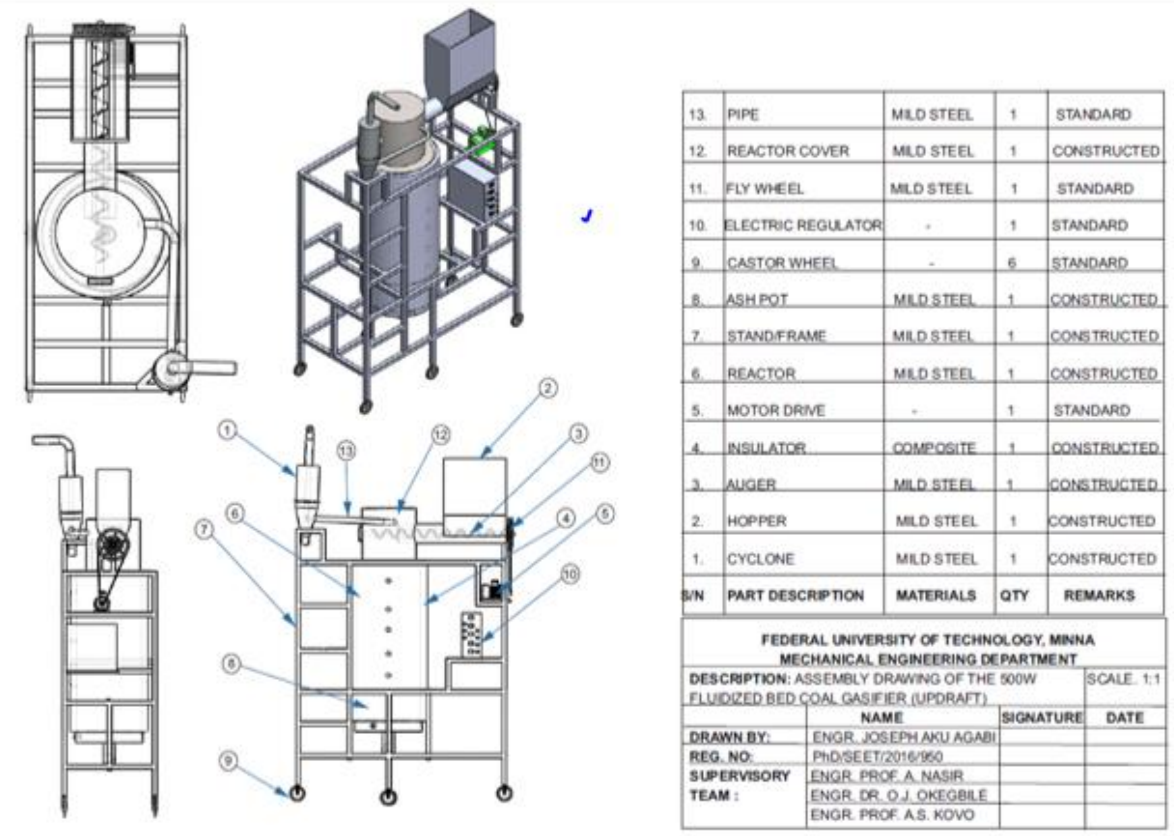

13.	PIPE	MILD STEEL	1	STANDARD
12.	REACTOR COVER	MILD STEEL	1	CONSTRUCTED
11.	FLY WHEEL	MILD STEEL	1	STANDARD
10.	ELECTRIC REGULATOR	-	1	STANDARD
9.	CASTOR WHEEL	-	6	STANDARD
8.	ASH POT	MILD STEEL	1	CONSTRUCTED
7.	STAND/FRAME	MILD STEEL	1	CONSTRUCTED
6.	REACTOR	MILD STEEL	1	CONSTRUCTED
5.	MOTOR DRIVE	-	1	STANDARD
4.	INSULATOR	COMPOSITE	1	CONSTRUCTED
3.	AUGER	MILD STEEL	1	CONSTRUCTED
2.	HOPPER	MILD STEEL	1	CONSTRUCTED
1.	CYCLONE	MILD STEEL	1	CONSTRUCTED
S/N	**PART DESCRIPTION**	**MATERIALS**	**QTY**	**REMARKS**

FEDERAL UNIVERSITY OF TECHNOLOGY, MINNA
MECHANICAL ENGINEERING DEPARTMENT

DESCRIPTION: ASSEMBLY DRAWING OF THE 500W FLUIDIZED BED COAL GASIFIER (UPDRAFT) SCALE 1:1

	NAME	**SIGNATURE**	**DATE**
DRAWN BY:	ENGR. JOSEPH AKU AGABI		
REG. NO:	PhD/SEET/2016/950		
SUPERVISORY TEAM :	ENGR. PROF. A. NASIR		
	ENGR. DR. O.J. OKEGBILE		
	ENGR. PROF. A.S. KOVO		

Figure 1: Assembly Drawing of the Gasifier

3.0 RESULTS AND DISCUSSION

Power rating and fuel consumption rate

Figure 2 displayed the plot of fuel consumption and power rating requirement for the updraft gasifier. As the power rating increases from 100kW to 1000kW, the fuel consumption rate also rises. Due to its high heating value, the coal has low economic fuel consumption close to that of the calculated fuel consumption of 108.6kg/hr. Equation (1) is the linear regression equation and the percent/residual curve displayed in Figure 3.

Fuel consumption rate FCR (kg/h) = 0.080 + 0.154 Power required (kW) (1)

From Eq. (1), a linear relationship exists between fuel consumption with the power required for the gasification with a constant coefficient of 0.080. Inputting this in equation 1, the coefficient of power requirement for the gasification is 0.154. The Pred R-Squared has a value of 100%. While the Adj R-Squared also has a value of 100% and 0.168280 as standard deviation. Thus the model is significant.

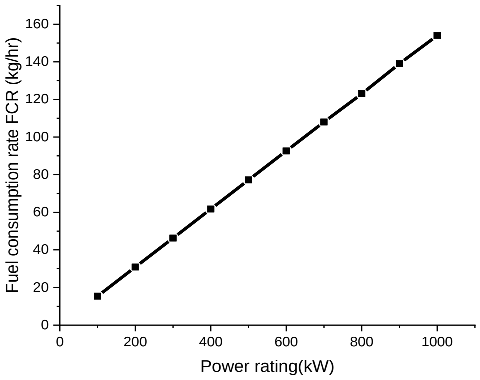

Figure 2: Variation of Fuel consumption rate and power required.

Figure 2 presents the residual plot for the analysis. Figure 2 showed the experimental value is close to the predicted values since the points are randomly distributed close to the line in the plot. It can be seen from the values of the Pred R-Squared and was close to 100.0% for the Adj R-Squared.

This work has shown that for optimal gasifier performance, the power rating is 700kW since the value of fuel consumption at 700kW power rating is 108Kg//hr, which is close to that of the calculated values 108.6Kg/hr.

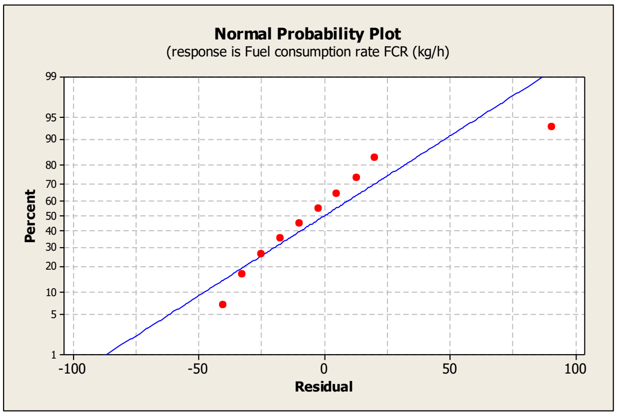

Figure 3: Residual plots for the fuel consumption and power rating

4.0 CONCLUSIONS

The design and MATLAB simulation of the operating parameter of Onyeama coal in updraft gasifier was investigated. The design operating parameters considered in the work are: power rating, air required, fuel consumption, hopper volume, time, reactor diameter and heights. These results show that there exist linear relationship of all the operating parameter with the power rating. It can be deduced that the sizing of the updraft gasifier (diameter and height) increased commensurately to increase in the power rating requirement and the operational time respectively.

REFERENCES

S. Vikrant and V. K. Agarwal, (2019). "Numerical Simulation of Coal Gasification In A Circulating Fluidized Bed Gasifier," *Brazilian J. Chem. Eng.*, vol. 16, no. 03, pp. 1289–1301.

A. M. Shakorfow (2016), "Operating and Performance Gasification Process Parameters," *Int. J. Sci. Res.*, vol. 5, no. 6.

M. Chukwu, C. O. Folayan, G. Y. Pam, (2016). Characterization of Some Nigerian Coals for Power Generation Journal of Combustion, Article ID 9728278, 11 pages

http://dx.doi.org/10.1155/2016/9728278

M. Akanksha ., G. Shalini ., S. Tripurari ., (2018). Effect of operating parameters on coal gasification. International Journal of Coal Science & Technology. Volume 5, Issue 2, pp 113–125.

T. Hong , C. Donglin and C. Jiuju (2009). "Effect of Operation Parameters on High Temperature Air Gasification." in *IEEE. Asia-Pacific Power and Energy Engineering Conference*

o

ISSN 2121-2987

Journal of NIMechE Vol.10 No. 2, pp 62-81
Printed in Nigeria

Copyright@2022, The Nigerian Institution of Mechanical Engineers (A Division of Nigerian Society of Engineers)

A COMPREHENSIVE REVIEW OF APPLICATION OF CUTTING FLUIDS IN TURNING AISI 304 ALLOY STEEL

Emmanuel Imhanote Awode[1*] Matthew Sunday Abolarin[2] and Kabiru Alani Olaiya [3].

[1]Mechanical Engineering Department, Air Force Institute of Technology, PMB 2104, Kaduna, Nigeria.

[2]Department of Mechanical Engineering, Federal University of Technology, Minna, Nigeria.

[3]Department of Mechanical Engineering, Lagos State Polytechnic, Ikorodu, Lagos State, Nigeria

Corresponding author's e-mail: e.awode@afit.edu.ng; greatawode@gmal.com; msabolarin2006@gmail.com; kabeeson2003@yahoo.com;

ABSTRACT

The growing challenge to having a safe environment and health as drawn the attention of government regulators, private sectors and machine operators to minimise the use of mineral oil-based cutting fluid. The last two centuries as witnessed the use of cutting fluids extensively in metal cutting operations. Generally, in early times cutting fluids consisted of primary oils which were used with brushes on the machine tool to cool and lubricate the metal forming process. Formulation of cutting fluid becomes more complicated with critical cutting operation. Cutting oils or water-miscible fluids are the largely classified available cutting fluids in the market today. Vegetable oil-based cutting fluids application in machining of AISI 304 alloy steel is the essence of this review. A lot of review has been reported that vegetable oil-based cutting fluids, known as metalworking fluids, tend to be environmentally friendly form of machining with related performance achieved when mineral oil-based cutting fluids are used. In this review, attention is placed on recent research work on formulation and application of vegetable oil-based cutting fluids in turning process. More so, the performances of various vegetable oil-based cutting fluids on some process parameters such as thrust force, surface roughness, temperature developed at the tool chip interface, and tool wear during turning process using different tool materials were highlighted. Therefore, a comparative study of some cutting fluids during AISI 304 alloy steel turning operation has been achieved.

Keywords: Cutting fluids, surface roughness, tool wear, turning, alloy steel

1. INTRODUCTION

One of the commonly viewed and employed variable that is needed for high quality machining operation is the cutting fluids because it prevent overheating of both workpiece and cutting tool, improve workpiece quality and minimise cutting tool wear. Cutting tool transform raw material workpiece into desired workpiece during machining. Cutting parameters such as cutting speed, feed rate and depth of cut are major factors that determine tool wear and tool life. Kuram *et al*, (2013) work shows that cutting fluid that is termed excellent must not be harmful and toxic to the operators' health condition, it must also be hazard-free, affordable and should be smoke-free or fog-free when used. Kuram *et al*, (2013) also reveal that cutting fluids are seen as either mineral oil base or vegetable oil base. However, base on their chemical formulation, cutting fluids are classified under: straight oils (nonemulsifiable), soluble oils (emulsified oils or emulsions), synthetic oil (non-mineral oil but formulated from alkaline organic and inorganic compounds), semi-synthetic oil (combination of the soluble oils and synthetic fluids). Results from formulated vegetable oil based cutting fluids have highly performed better than mineral oil-based cutting fluids during turning process (Lawal *et al,* 2012). Machining industry has achieved tremendous feat beginning from raw material processing to finished products which involve the application of cutting fluid, technology and certain mathematical model. In recent times, technological advancement had made it possible to achieve high dimensional accuracies with complex geometry (Alves and Oliveira, 2008). The formulation of a new generation of cutting fluids that delivers high performance machining and environmental friendliness could be realised with the use of vegetable oil base stock (Taga *et al,* 2015). Vegetable oils are generally extracted from plants and they are known to be triglyceride. Triglycerides are known to have lower densities compared to water, and may be solid (fats or butters) or liquid (oils) at normal room temperatures. Triglycerides which are also called Triacylglycerol (TAG) are made from glycerol molecules with three long chain fatty acids attached at the hydroxyl groups via ester linkages. These authors industrial analysis shows that vegetable oil can prolong tool life, minimise surface roughness and improve the performance of cutting when compared to mineral oil (Kuram *et al,* 2013 and Woods, 2005).

Summarily, cutting fluids possess a lot of those liquids and gasses that are needed and are applied to the tool and the workpiece that is machined. A lot of quantities are employed every year to achieve a number of objectives. For example, cutting fluids prevent tool overheating, cool workpiece, reduce surface roughness, prevent corrosion of workpiece, aid satisfactory chip formation, prevent inaccurate final dimensions from machining results, flush away chip from the cutting zone and reduce power consumption. Conclusively, the right cutting fluid can reduce the number of unplanned stoppages and increase the life of both the tool and the cutting fluid (Richard, 2021). Therefore, there is need to determine the water solubility fluids performance in the various classification.

1.1 Water Soluble Fluids

The rise in demand for biodegradable materials has created way for employing vegetable oils as an alternative to petroleum based polymeric materials (Bisio and Xanthos 2005; Li, 2001), largely in machining operations. There is consistent rise as regards environment concern (Eichenberger, 1991). Lubricants are used in several areas; hence, their environmental acceptability is prioritise with significant effect. Therefore, in the early 90s, discoveries on biodegradable functional fluids came up as one of the major importance in lubrication, which caused a lot of rising figures of environmentally friendly fluids and lubricants in the market (Busch and Backe, 1994). Vegetable oils, such as rapeseed (Flider, 1995) and canola (Green, 1993) are among the more futuristic spacemen as basestocks for the biodegradable lubricants. They are readily biodegradable and less costly than synthetic basestocks. They most display quite acceptable performance as lubricants (Tract, 1994). Conventionally, Cutting fluids are classified into three major parts; that is; (i) water-soluble fluids (ii) neat cutting oils and (iii) gases. The water-soluble fluids can be grouped into emulsifiable oils (soluble oils), chemical (synthetic) fluids or semi-chemical (semi-synthetic) fluids, as shown in Figure 1. Fluids placed in these groups are available for light, medium and heavy duty performance (Baradie, 1996).

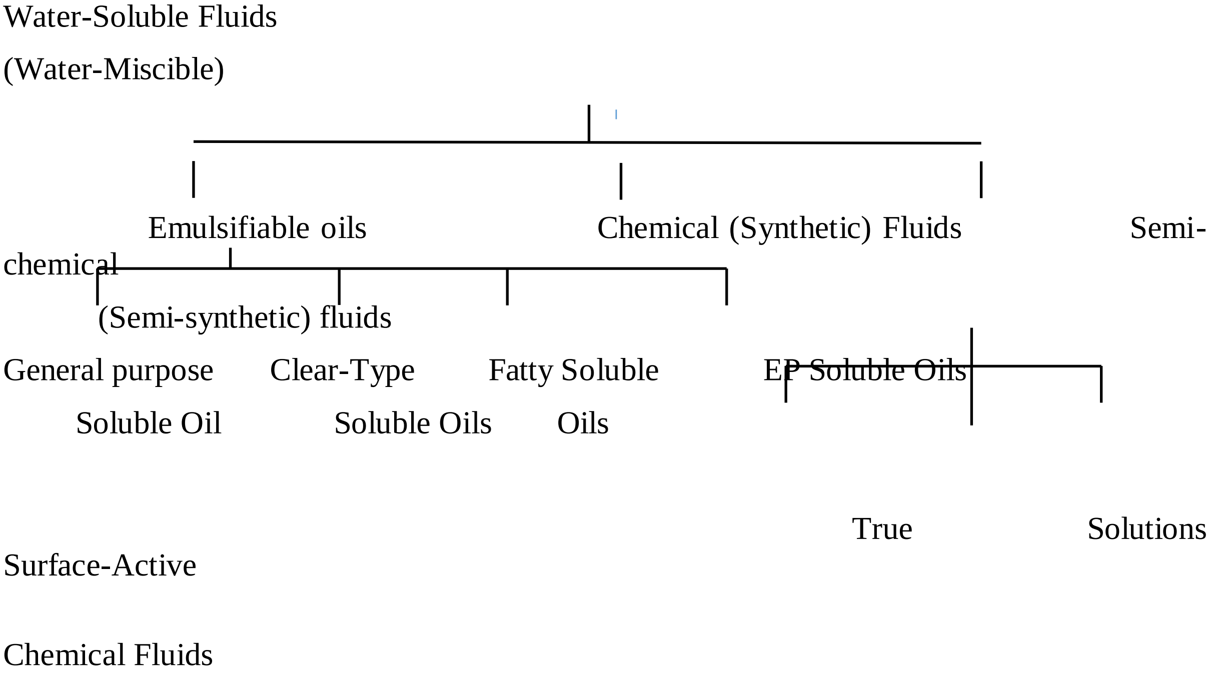

Figure 1: Water-soluble fluids classification (Baradie, 1996)

The oil-in-water is dispersed with the introduction of emulsifiers in order to establish a stable oil-in-water emulsion. The amount of emulsifier increase influences increase in pH, kinematic viscousity and thermal conductivity. The reduction in the amount of emulsifier influences the reduction in fire and flash points (Rao *et al*, 2007). The amount of critical property of soluble oils comes from emulsion stability that boast the highest. There must be sustenance without separation for minimum of six months of the cutting fluids concentrate (Kuram *et al,* 2013). The presence of water in emulsion induces growth of bacteria, rust, losses of phosphorus, chlorine and sulphur based chemical additives known as EP (extreme pressure) additives employed under extreme pressure conditions alone (Kuram *et al,* 2013). Therefore, the means where extreme pressure additives form lubricant layer that are solid between cutting fluid and the metal surface is refer to as chemical reaction. The criteria for extreme pressure additives to be able to lower friction and wear significantly is good anti-weld properties and low shear strength (Kuram *et al,* 2013). Therefore, there is need to understudy these various cutting fluids when carrying out machining operation.

2.0 APPLICATION OF CUTTING FLUIDS DURING MACHINING OPERATION

The commonly used fluid during machining operation is known as cutting fluid. Most often these fluids used for cutting are also refer to as coolant but it is more than that. A cutting fluid does many functions and cooling the tool and workpiece is just one out of the several functions (Club, 2019). Cutting fluids contribute to machining process because it acts as lubricant by reducing friction and reduces the heat generated (Ademoh *et al,* 2016). Also, the cutting fluid act as an effective coolant, because frictional heating cannot be completely eliminated and often, not even substantially reduced. Cutting fluid could act as an anti-weld agent by chip flushing to stop the tendency of the work material to weld the tool under heat and pressure (Ademoh *et al,* 2016).

Although, machining performance as effectively improved as a result of cutting fluid usage, traditional metal cutting fluids are becoming a devalued added cost to businesses in recent times in the machining industry Singh and Gupta 2006). Lawal *et al*, (2012) conducted a comprehensive review on the application of vegetable oil-based metalworking fluids (MWFs) in machining ferrous metals. The cause of heat and friction were removed when vegetable oil-based MWFs were employed, which made provision for lubrication between chips of both interfaces. The work further discussed the machinability of several ferrous metals with vegetable oil-based MWFs as fluids for cutting. The authors pointed out that research and development (R & D), and environment impact, are the factors and challenges faced when using MWFs in machining. The work was concluded with MWFs inclusion in machining, showing better performance. Coconut oil showed better performance compared to mineral oil, in terms cutting parameters (90 m/min cutting speed, 1 mm depth of cut, and 0.35 mm/rev feed rate). The surface roughness values obtained were 4.5 µm and 5.5 µm for coconut and mineral oils respectively.

2.1 Vegetable oil-based cutting fluid for turning process

Vegetable oil-based cutting fluids are used to remove friction and heat effect, ensure chip-tool interfaces lubrication, improvement of workpiece surface finish and flush away chips from turning of steel alloys. Therefore, the machinability of AISI 304 alloys is sometime a difficult challenge; Low thermal conductivity, high ductility, high work hardening tendency and high strength are part of the characteristics that make them difficult. The general observation when turning these materials are high cutting force, high tool wear and poor surface finish of the work materials. Therefore, there is need to understudy the properties of the vegetable oils that is suitable for the cutting fluids formulation.

2.2 Properties of vegetable oils suitable for based Cutting Fluids

Kuram *et al,* (2013) revealed that vegetable oils consist of triacylglycerides (triglycerides) which are glycerol molecules with three long chain fatty acids attached at the hydroxyl group via ester linkages. Desirable properties of lubricants are provided by the triglycerides structure of vegetable oils. High strength lubricant films which interact strongly with metallic surfaces and reduce both friction and wear are provided by the long, polar fatty acid chains. Thermal and oxidation stability of these oils are limited, despite, vegetable oils have a higher viscosity index (Abdalla and Patel, 2006). (Kuram *et al*, 2013) work also discovered for the following reasons, that vegetable oils out-perform other oils:

i. Vegetable oils machining temperature increases due to a high natural viscosity. At high temperature the viscosity of vegetable oil drops more slowly than that of mineral oils.

ii. Vegetable oil molecules are quite homogenous in size, but mineral oil molecules vary in size. Consequently, the properties of mineral oils such as viscosity and boiling temperature are more susceptible to variation (Krahenbuhl, 2002).

iii. Vegetable oils have good properties for lubrication. The vegetable oil molecules make possible the highly lubricating properties of vegetable oils, as well as the chemical structure of the oil itself. Dense homogenous alignment of vegetable oils molecules create a thick, strong and durable film layer of lubricant, which gives the oil greater capacity to absorb pressure in contrast to mineral oil.

iv. Vegetable oils reduce smoke formation and fire hazard because it possesses a higher flash point (Krahenbuhl, 2002 and Woods, 2005). The cutting fluid is used in high temperature conditions because it possesses higher flash point value.

v. Vegetable oil results in less loss from vaporization and misting because it possesses higher boiling point and greater molecular weight (Khan and Dhar, 2006).

2.3 Typical process of cutting fluid formulations

The composition of oil-in-water cutting fluids can be characterised as the addition of water to base oil and emulsifier. Other components which may also be added to the fluid are: solution improvers, biocide/fungicides, corrosion and rust inhibitors, neutralising agents, agents to improve stability in hard waters and foam inhibitors (Alves and Oliveira, 2008). This author, presented the formulation processes of cutting fluid as follows:

(a) Additives selection: important check and balances should be done in selecting components that are not challenging or hazardous to health or the environment. Juneja, (2003), listed some of the additives and their function in Table 1.

(b) Mixing: add the base oil to water and stir for 2 min. Then other substances (additives) are added and stirred to mixture consistency, for 15 min. A test mixture must repose for 24 hrs without oil/water separation. If the emulsion is not stable, the amount of emulsifier needs to be adjusted.

Cutting emulsion verification: the chemical and physical properties of the cutting fluid need to be checked such as: pH, Viscosity, corrosion and biodegradability which may necessitate adjustment of formulation.

Tables 1: Cutting Fluid Additives and their Functions

Additives	Function
Mineral oils and other hydrocarbon	Base oil
Polyglocoether (for water soluble oils)	Emulsifier
Aliphatic amines (for water soluble oils)	Neutralizing oil
Aliphatic amines in neutralized form	Neutralizing agent
Sulphonates	Corrosion protection and extreme pressure additive (EPA)
Fatty acid amides	Lubricating Improvement
Sulphur/ Phosphorous Compound	Extreme Pressure additives
Aldehyde derivatives (for water based coolants)	Biocides

Source: Juneja, (2003).

Alves and Oliveira (2008) work presented the processes required to determine the corrosion grade of the cutting fluid among other cutting fluid formulation processes.

These processes are corrosion test, pH level test and Viscosity test. Therefore, both petroleum and vegetable oils have a typical characteristics and comparatively shows some differences as shown in Table 2.

Table 2: Characteristics of petroleum and vegetable oils

Characteristics of petroleum and vegetable oils [38]

Characteristics	Petroleum oil	Vegetable oil
Lubricity	Low	High
Oxidative stability (RPVOT)	300	50
Viscosity Index (VI)	100	200
Hydrolytic stability	High	High
Polarity	Low polar	High polar
Saturation	Saturated	Unsaturated
Flash point (°F)	200	450
Pour point (°F)	-35	-35

RPVOT Rotary Pressure Vessel Oxidation Test

2.4.1 Neem oil based cutting fluid

Vegetable oils have proven in many instances to be a viable option for use as cutting fluid especially considering the added advantage of environmental degradation. The challenge is finding out whether Neem seed oil can be used as cutting fluid. As Nigeria is situated in tropical region of the world where temperature rarely drops to 8°C, characterised and formulated Neem oil is suitable as coolants and can readily be poured (Ademoh *et al*, 2016). The dry neem seed with it chemical chain is $C_{35}H_{44}O_{16}$ shown in Figure 2.

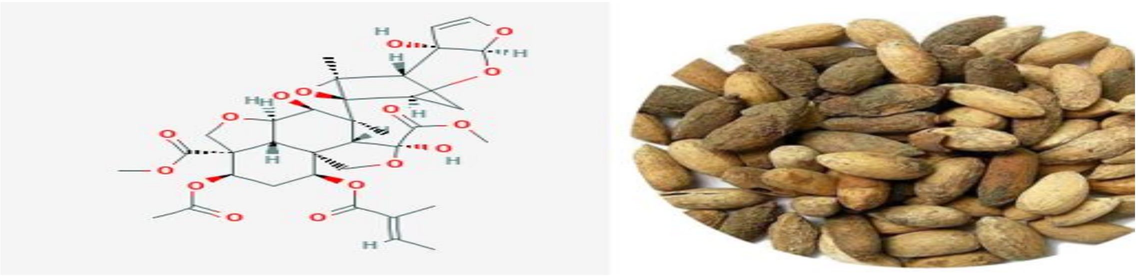

Figure 2: Dry Neem Seed with it chemical chain. Source: (CAS, 2021).

2.4.2 Jatropha oil-based cutting fluid

Cutting fluid that is jatropha oil-based is obtained from jatropha which is a genus in the spurge family that develop substances that are toxic to protect them against animals and other pests (BioPro, 2015). Jatropha shows a pattern of suitable fatty acid that is uniquely grown as a lone crop so as to stay off animal feed production competition and direct food competition (Winter, 2012). The use of cutting fluids from jatropha oil-based are gradually gaining popularity in machining as a result of environmental and health impacts that are not wanted from traditional mineral oil (Kazeem and Adesina, 2020). Jatropha oil based cutting fluid is employed as an anti-wear fluid and modifies friction as a result of their good interaction with the surfaces with which they are engaged (Kazeem and Adesina, 2020). This review seek to understudy unpopular vegetable oils like jatropha oil as machining cutting fluids. The effects of jatropha oil emulsion on tool wear and surface roughness in turning AISI 304 alloy steel using tungsten coated carbide insert were carried out in this work and compared with traditional mineral oil. This review shows an evaluation of a jatropha oil based cutting fluid role during turning operation.

Shivani *et al,* (2011) investigated the extraction and analysis of Jatropha curcas seed oil. Jatropha curcas is a versatile shrub with several applications and many economic potentials for its seed oil, which can be turned into biodiesel- an alternative to petro-diesel. It aims to turn around energy challenges and also to minimise environmental changes. The fact that the oil of Jatropha curcas is not readily edible makes its usage very attractive and devoid of competition from other edible vegetable oils.

The present study deals with oil extraction by various methods and its physico-chemical analysis. Figure 3 shows the Jatropha seeds optimized using organic solvents to get the jatropha seed oil. The effects of parameters on the oil extraction namely type of organic solvents and different techniques were also considered to optimize the processing conditions for achieving maximum oil yield with the acid value and antioxidant property of the oil were also investigated. The maximum oil yield was obtained by using Soxhlet extraction method and hexane as a solvent.

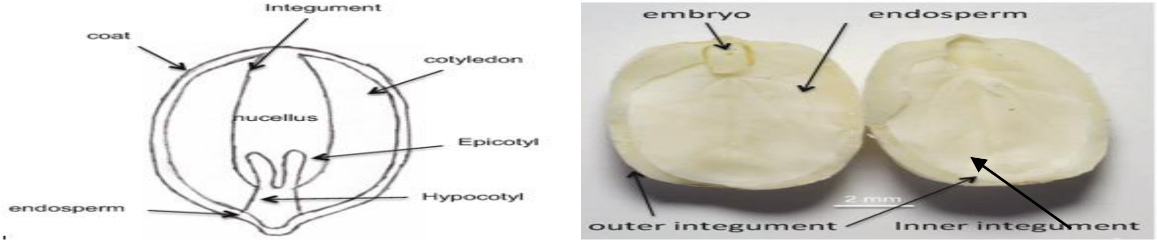

Figure 3: Jatropha Curcas Seed. Source: Shivani *et al,* (2011).

2.4.3 Sunflower oil-based cutting fluid

Kuram, (2012) studied the effect of cutting fluid types and cutting parameters on surface roughness and thrust force with three different vegetable-based cutting fluids developed from raw and refined sunflower oil and two commercial types (vegetable and mineral based cutting oils) during drilling of AISI 304 austenitic stainless steel with high speed steel E-grade (HSS-E) tool. The vegetable oil-based cutting fluids were formulated with various additives to meet the specifications such as resistance to bacterial growth, corrosion, antifoaming agent and anti-wear characteristics (Kuram, 2009). Table 3 shows the characterization of vegetable-based cutting fluids developed for the study. They considered spindle speed, feed rate and drilling depth as input parameters with two sets of experimental design. In the first set of experimental design, they studied the effect of spindle speeds (520, 620 and 720 rpm) at a constant feed rate of 0.12 mm/rev and depth of 21 mm., while in the second set, they studied the effect of feed rates (0.08, 0.12, 0.16 mm/rev) at a constant spindle speed of 620 rpm and drilling depth of 21 mm. From the analysis, the following observations were made: (i) an increase in the spindle speed and change of cutting fluid type decreased the thrust force at the feed rate of 0.12 mm/ rev and drilling depth of 21 mm, which was consistent with the literature (Davim *et al*, 2006; Basavarajappa *et al*, 2008 and Ramulu *et al*, 2008) (ii) when the spindle speed was 620 rpm, and drilling depth was 21 mm, the thrust force decreased as the feed rate decreased and this was consistent with previous findings [Mendes *et al*, 2006; Shetty *et al*, 2009 and Rivero *et al*, 2006) (iii) at a feed rate of 0.12 mm/rev and drilling depth of 21 mm, an increase in spindle speed improved surface finish and this was in agreement with findings from other researchers (Mendes *et al*, 2006, Rivero *et al*, 2006 and Tsao, 2007).

2.4.4 Coconut oil-based cutting fluid

Xavior *et al*, (2009) determined the influence of cutting fluids on tool wear and surface roughness during turning of AISI 304 austenitic stainless steel, with carbide cutting tool, using different cutting fluids (coconut oil, emulsion and neat cutting oil-immiscible with water). Taguchi design of experiment (DOE) L_{27} $(3)^4$ orthogonal array was employed for the work, with cutting speed, feed rate, depth of cut and cutting fluids as variable input parameters. The machining operation results obtained showed that coconut oil had the highest effect on surface roughness and tool (1.91, 2.06, and 2.11µm and 0.045, 0.055, 0.071 mm) followed by cutting oil (2.25, 2.50 and 2.43 µm, and 0.098, 0.095 and 0.104 mm). Soluble oil had the lowest effect of (2.68, 2.92, and 2.92 µm, and 0.076, 0.094 and 0.10 mm), with cutting parameters (0.5 mm constant depth of cut, 0.2, 0.25, and 0.28 mm/rev feed rate, and 38.95, 61.35 and 97.38 m/min cutting speed. The observation from the authors' showed that feed rate contributed 61.54% to surface roughness, while cutting speed had 46.49% contribution to tool wear. Coconut oil proved to have better effect than the conventional mineral oil in terms of improving surface finish and reducing tool wear.

Krishna *et al*, (2010) investigated the performance of nanoboric acid suspensions in SAE-40 and coconut oil during turning of AISI 1040 steel with cemented carbide tool (SNMG 120408). The variation of cutting tool temperatures, average tool flank wear and the surface roughness of the machined surface with cutting speed were studied using nonsolid lubricant suspensions in lubricating oil. The experiments were conducted under the following conditions; cutting speed (60, 80 and 100 m/min); feed rate (0.14, 0.16 and 0.2 mm/rev); depth of cut (1.0 mm). Solid lubricants of boric acid with particle size of 50 nm, lubricating oil SAE-40 and coconut oil with flow rate of 10 ml/min were used for lubrication. The temperature was measured by the embedded thermocouple placed at the bottom of the tool inserted in the tool holder. They reported that the cooling action of the lubricant with nanosolid lubricant suspensions was evident from the measurement of the cutting tool temperatures. The authors submission shows that cutting temperatures increased with cutting speed irrespective of the lubricant, and cutting temperatures were less with coconut oil compared to SAE-40 for identical cutting conditions. Also, cutting temperatures increased with increase in feed rate at all the lubricant conditions. However, Table 3 present the physiochemical properties standard method and description employed for each of the reviewed vegetable oils.

Table 3: Physiochemical properties of vegetable oils

Property	**Method**	**Description**
Specific gravity	$\frac{weight\ of\ oil}{weight\ of\ equal\ vol\ of\ water}$	The weight of oil was compared to the weight of an equal volume of distilled water to determine the specific gravity of the extracted oil by using a specific gravity bottle.
Free fatty acid		Free Fatty Acid (FFA) = $\frac{Acid\ value}{2}$
Viscocity@ 40°C	ASTM D445 and ISO 3104	Equation used was: $\frac{\eta}{dt} = A - Bt^2$
Acid value	Acid value mg/KOH/g	= $\frac{Titre\ value\ x\ 0.1\ M\ KOH\ x\ 56.10}{weight\ of\ sample\ (g)}$
Peroxity Value	ASTM DD5348	The muffle furnance was used to heat the oil Till weight remain constant
Flash Point	ASTM D93	The flash point tester was used to determine the flash point of the various sample
Saponification value	ASTM D558	
pH value		The pH values of the vegetable oils were determined using the pH meter.
Iodine value		AOAC (2006) was used to evaluate the Iodine
Density @ 15°C	ASTM D4052	Specific Gravity (SG) = $\frac{Weight\ of\ Xml\ of\ oil\ x\ 0.1\ x\ 12.69}{Weight\ of\ Xml\ of\ Water}$ = $\frac{B-A}{C-A}$

2.5 Turning Operation

Pralhad *et al*, (2018) predicted surface roughness and cutting force under MQL turning of AISI 4340 with nano fluid, by using response surface methodology. A cylindrical bar of AISI 4340 workpiece material was used, having BHN 217, 100mm length and 24mm diameter. CCMT-090308 tungsten carbide insert was used as cutting tool. Mitutoyo made surface roughness tester (SJ-201P) with a cut-off value of 0.8mm was employed to measure the turned workpiece. Kistler Dynamometer, a charge amplifier and PC software were employed to measure the cutting forces. Cutting speed, feed rate, depth of cut and tool nose radius were the cutting parameters considered for the machining operation. The experimental design was full factorial design matrix with RSM employed for experimental analysis. CNC lathe was used to conduct MQL machining trials with nano fluid. The authors were able to develop a surface roughness and cutting force predictor mathematical model, in relation to cutting speed, feed, depth of cut and tool nose radius for alloy steel (AISI 4340) material, under MQL mode with nano fluid. Prediction error related to validation experiments showed surface roughness average error was below ±11% for maximum error mathematical prediction, while cutting force average error was below ±5%. Also, cutting force (F_z) and surface roughness (R_a) predicted values yielded suitable fit with quadratic model from ANOVA results, and confirmation experiments conducted.

Zheng *et al*, (2018) studied the effects of cutting parameters on wear behaviour of coated tool and surface roughness in high-speed turning of 300M. The HRC47 hardness workpiece material used was a 300M (40CrNi2SiMoVA) of low alloy medium carbon martensitic high-strength steel, 110 mm diameter and 300 mm long. The tool was a coated cemented carbide with high content of cobalt matrix. The tool insert and the tool holder were SNMG120408FN and MSSNR2020K12 respectively. The turning operation was conducted using a CNC lathe (Model CKD6136i, Dalian Machine Tools Group, China), with max spindle speed of 6000 rev/min. The experiment was carried out under dry condition, with a (Model USB200) digital tool microscope. VBave = 0.3 mm was the average wear width of the flank face requirement for tool failure. Cutting force and temperature were measured, using a thermal tracking instrument (Model TH5104R, NEC, Japan). Surface roughness tester (Model CS-3200 was used to detect the machine surface roughness (*Ra*). The machining operation conclusively yielded 130N-240N as the resultant cutting force, which in the initial cutting stage was not very large. Axial force *Fz*, is the maximum component obtained. Cutting speed, *vc* = 300–500 m/min, feed, *f* = 0.10–0.20 mm/rev, and depth of cut, *ap* = 0.15, 0.25 mm affected the cutting force. Also at the initial stage, the cutting temperature was within the range of 300–500 °C.V*c* is the most important effect factor on the cutting temperature, while *ap* is the least effect factor. Peeling off and micro-chipping were some of the damages characteristics experienced at the rake face at *Vc* = 600 m/min. The coated tool main wear mechanisms are the oxidation wear, diffusion wear, adhesive wear and abrasive wear. Surface roughness, *Ra* is majorly influenced by the feed, *f,* and *Ra* is likely to rise with increase in the average flank wear. Also, increase in cutting parameters resulted in accelerated tool flank wear. Therefore, optimization of cutting parameters, prediction of tool life and machined surface roughness, depended on the positive role from the results of the work.

Lawal *et al*, (2013) investigated vegetable and mineral oil-in-water emulsion cutting fluids, in turning AISI 4340 steel with coated carbide tools. The turning process was carried out using Colchester VS Master 3250 (165 ×1,270 mm) gap bed centre lathe, powered at 7.5 kW, with a TiN coated tungsten carbide tool insert, using 3,250 rpm spindle speed on a round bar, AISI 4340 alloy steel with a diameter of 90 mm and a length of 360 mm for sustaining cylindrical turning length ratio, and achieve the require stiffness of workpiece/cutting force/chuck. The metal machining industry have accepted and applied hardened HB 270-310 AISI 4340 alloy steel, which has become popular in industrial sector for manufacturing of shafts, gears, and aircraft landing gear. Cutting speed, feed rate and depth of cut are the three cutting parameters considered for the experimentation with DOE via Taguchi method specified L_{27} (3^4) orthogonal array, as the employed basic experimental set up plus four input parameters with three assumed levels each. Tool insert configuration and machine rating determine parameter selection. In each experimental run, a fresh cutting tool insert was used for a fixed cutting time of 15 min, thus, flank wear was observed and measured after each turning for 15 min, using an optical microscope. Signal to noise ratio (S/N) for the optimal cutting parameters for the cutting force were: 160 m/min of cutting speed (level 1); 0.18 mm/rev of feed (level 1); 1.75 mm of depth of cut (level 2), and 2.97 mm^2/s palm kernel oil based cutting fluid (level 3). The significant factors that affected flank wear obtained from ANOVA is 85.36% cutting speed; 4.81% feed rate; followed by 2.5% depth of cut, and 1.8% cutting fluid. For stainless steel high machining, there is extremely high temperature on cutting tools in the cutting zone, resulting in rapid tool wear. The experimental work employed cooling during the machining process, so as to limit heat. Also, employing regression analysis with MiniTab 14, mathematical model for cutting speed, feed rate, depth of cut and cutting fluids can be obtained. Conclusively, the experimental results obtained from this work indicated that flank wear when turning AISI 4340 steel with coated carbide tools, can be improved with the use of the developed novel vegetable oil-in-water emulsion cutting fluids formulations.

Mishra and Gangele (2012) applied Taguchi method in optimization of tool flank wear width in turning operation of AISI 1045 steel. The machining test was carried out on an engine lathe of HMT, employing tungsten carbide inserts) in dry condition. The cutting parameters were speed, feed and cutting depth. The workpiece was AISI 1045 steel rod of dimension 80mm diameter and 400mm length. For each trial condition tungsten carbide positive rake triangular inserts for all the three edges were used. This was in line with the trial condition specified by orthogonal array 27 cutting edges of carbide inserts using 4 minutes machining time. Magnifying glass of 10X magnification was employed to measure the tool flank wear width. The tool flank wear width were prominently affected by three machining parameters (cutting speed, feed rate and depth of cut). ANOVA was employed to obtain each machining parameters percentage contribution. The authors obtained average confirmation run of the three confirmation runs conducted at 88.33 µm surface roughness selected optimal settings for the turning process parameters. The work found Taguchi method suitable for tool flank wear width optimisation. Minimum tool wear for the machining operation were found to be cutting speed at level 1(110m/min), feed rate at level 1 (0.15mm/rev) and depth of cut at level 1 (0.10mm). Machining parameters percentage contribution to tool wear characteristics contribution were cutting speed 47.45%, feed rate 25.75%, and depth of cut 16.52%. Tool flank wear width reduction of 23.85% was obtained during working from the experimental work.

2.6 AISI 304 alloy steel

The workpiece material for this study is an austenitic chromium-nickel stainless steel categorised as AISI 304 as shown in Figure 4. This type 304 is the most versatile and widely used stainless steel (Azom 2019). Stainless steel types 1.4301 is also known as grades 304. AISI 304 can also be referred to as 18/8 which is derived from the nominal composition of type 304, being 18% chromium and 8% nickel. Stainless steel type 304 is a part of a family of stainless steel alloys (301, 302, 303, 304, 316, and 347). This alloy steel grade is mostly used in food and chemical processing industries. This alloy steel is also employed in beverage and dairy industries, used as heat exchangers and chemicals that are mild. Presently, stainless steel are a household name involve in everyone's life and greatly involve in wild range of industries


AISI 304, 25mm diameter, 500mm length

Figure 4: AISI 304 alloy steel Workpiece

The chemical composition of stainless steel is the chemical element deposits within the steel. 304 alloy steel has 9 visible elements in percentage just like other 304 series as shown in Table 4.

Table 4: Chemical composition for 304 stainless steel alloys

%	**304**	**304L**	**304H**
C	0.0 - 0.07	0.0 - 0.03	0.04-0.08
Mn	0.0 - 2.0	0.0-2.00	0.0-2.0
Si	0.0 - 1.00	0.0-1.00	0.0-1.0
P	0.0 - 0.05	0	0.0-0.04
S	0.0 - 0.03	0.0-0.02	0.0-0.02
Cr	17.50-19.50	17.50-19.50	17.00-19.00
Ni	8.00 - 10.50	8.00-10.50	8.00-11.00
Fe	Balance	Balance	Balance
N	0.0-0.11	0.0-0.11	0.0-0.10

Source: (Azom, 2019)

Turning operation on AISI 304 alloy steel

Turning is a machining operation that removes metal from the outer diameter of a rotating cylindrical workpiece (Khandey, 2009). Turining operation causes the reduction of the diameter of the workpiece, normally, to a required dimension, and smooth finish on the metal is achieved. Most times, the workpiece will be turned so that adjacent sections have varying diameters. The machining operation that produces cylindrical parts is turning. Yang and Tarng (1998) used turning operation to design the optimisation of cutting parameters for turning operations based on the Taguchi method as shown in Figure 5. Thus, proper selection of the cutting parameters, are often accomplished using mathematical models, based on statistical regression techniques or neural computing.

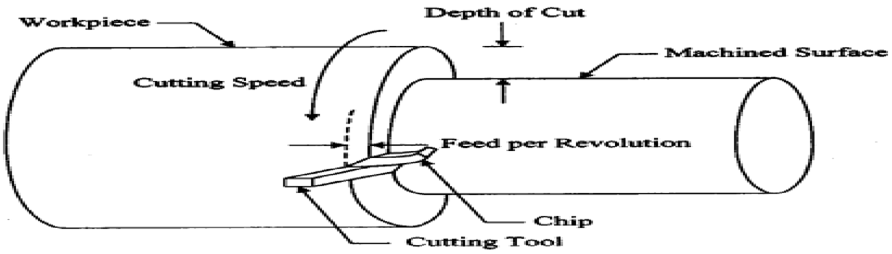

Figure 5: Basic Turning Operation. Korkut et al, (2004).

Korkut et al, (2004) determined the optimum cutting parameters during machining of AISI 304 austenitic stainless steel (ASS). The machining test were performed by single point turning of AISI 304 ASS with dimensions 200 mm long and 30 mm in diameter. The experiments were conducted using CNC Johnford TC-35 lathe, with cemented carbide as cutting tool. Thus, a continuous variable spindle speed of up to 3500 m/min, with a maximum power of 20kW was obtained during the machining operation. The result obtained showed the flank wear (V_B) curve in the machining of the workpiece (AISI 304 ASS) at a cutting speed of 120,150 and 180m/min. The results also showed the cutting parameters readings as 0.24mm/rev feed rate, and 2.5 mm depth of cut.

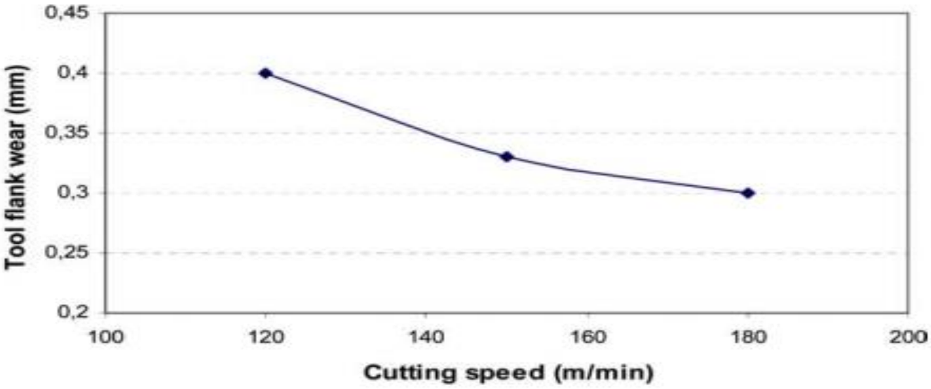

Figure 6: Flank wear when machining AISI 304 ASS. Korkut et al, (2004)

Figure 6 shows that tool wear increases with increase in cutting speed. The author further showed that tool wear started to increase at 210 m/min cutting speed when more test were carried out.

3. CHALLENGES FROM RESEARCH AND DEVELOPMENT OF VEGETABLE-OILS BASED CUTTING FLUIDS

Challenges from research and development of vegetable-oils based cutting fluids application in machining processes have witnessed tremendous attention in recent times, as a result of performances recorded during machining processes. Another factor is the current focus to the environmental impacts of industry by governmental regulations. However, just like all other aspects of technology, R & D is an ongoing concern in the application of vegetable-oil during machining processes. A critical observation at literature on the use of vegetable oil-based cutting fluids shows that, it is commonly used in machining of several AISI alloy steels.

There are a lot of these vegetable-oils based cutting fluids in today's market and some of the examples of vegetable-oils that are commercialised are (i) Desigreen: 100, 120, 215, 300, Desiclean: 1000, Desigreen based-12, Desigreen penetrant (ii) ECOLUBE and (iii) CIMFREE VG: 920M, 990M, 901ZH, 3900H, 703ES, S175, S110P, MF5350. Some of these products are used for medium to heavy-duty machining and grinding processes and are applicable to ferrous and non-ferrous metals. From the understudied literature, it was seen that, there had been a gap in the application of vegetable-oils based cutting fluids on various AISI alloy steel grade materials. A handful attempts have been made in the application of vegetable oil based cutting fluids during machining of AISI 304 alloy steel grades (Ojolo and Ohunakin, 2011; Ojolo *et al*, 2008). However, a lot of work still needed to be carried out in the application of vegetable-oils based cutting fluids in machining of AISI 304 alloy steels. AISI alloy steel materials which were commonly grouped into 200, 300 and 400 series currently occupy a significant position in manufacturing industry, as they have diverse applications in engineering fields. AISI 304 alloy steels are known to be heat-resistant alloys of 18/8 chromium-nickel, that exhibit a combination of mechanical strength and resistance to surface degradation. This statement calls for urgent need to focus more attention on research and development in the application of vegetable-oils based cutting fluids in the machining of AISI 304 alloy steel materials. The results of investigation of the effect of palm oil as MQL lubricant on high speed drilling of titanium alloys by Rahim and Sasahara (2011) shows that vegetable-oils based cutting fluids have great potential in machining of AISI 304 alloy steel grades.

3.1 Gas Chromatography Mass Spectrometer (GC-MS) Analysis

The fatty acid composition results for the two oils samples indicated that jatropha seed oil (JSO) has an approximately 21.6% saturated fat with the main contributors being 14.2% palmitic acid, 7% stearic acid and 0.4% 0ther acids. On the other hand, 78.4% of jatropha seed oil is unsaturated fat with 44.7% oleic acid (monounsaturated) and 32.8% linoleic acid (polyunsaturated). Neem seed oil (NSO) has approximately 37.0% saturated fat with the main contributor being 18.1% palmitic acid and 18.1% stearic acid, while about 63.0% is unsaturated with 44.5% oleic acid (monounsaturated) and 18.3% linoleic acid (polyunsaturated) are major contributors. The fatty acid composition or profile for one of the two samples of oils is shown in Figure 7 showing the mass spectrum for JSO analysis.

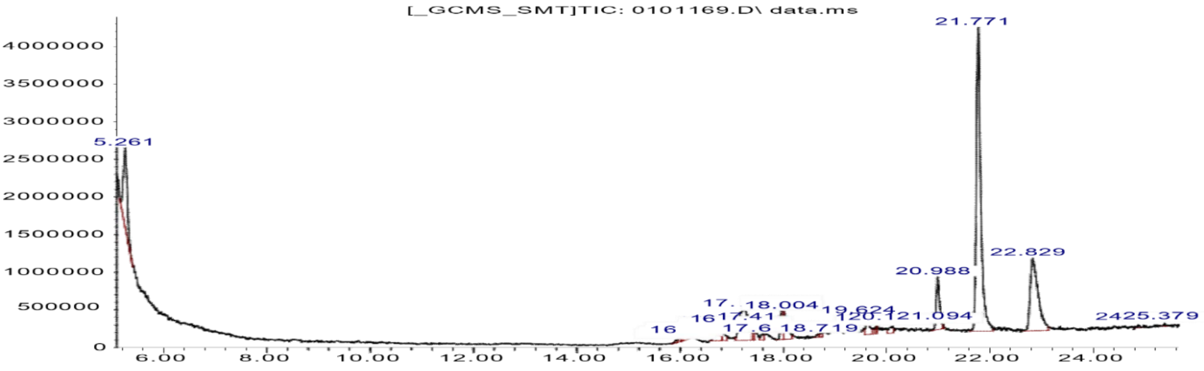

Figure 7: Gas Chromatography and Mass Spectrum (GCMS) Test Analysis for JBCF

The results obtained in Figure 7 and Table 5 are in agreement with existing literatures.

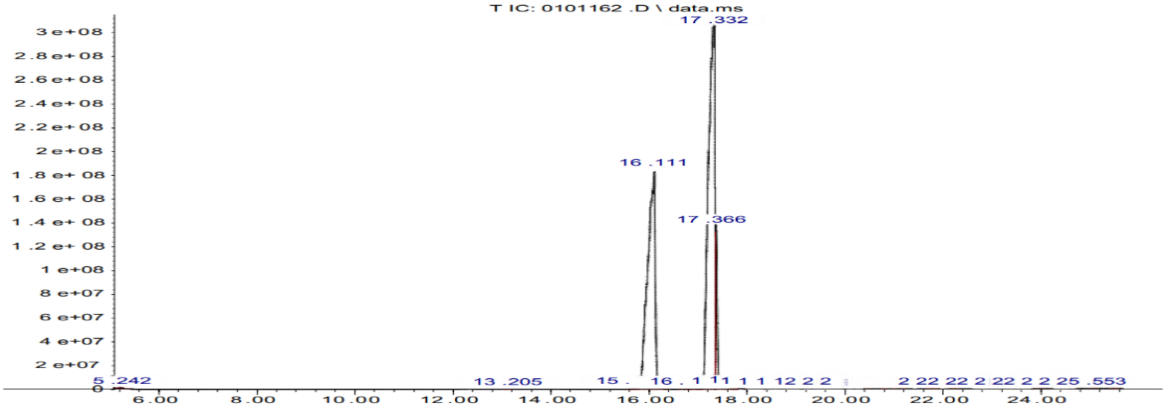

Figure 8: Gas Chromatography and Mass Spectrum (GCMS) Test Analysis for NBCF

Table 5: Fatty acid composition of Jatropha and Neem oils

Type of acid		Symbol	Fraction (%)	
Common Name	Formula		JSO	NSO
Palmitoliec acid	$(CH_3(CH_2)_{10}COOH)$	C16:1*	0.7	-
Myristic acid	$(CH_3(CH_2)_{12}COOH)$	C14:0*	0.1	-
Palmitic acid	$(CH_3(CH_2)_{14}COOH)$	C16:0*	14.2	18.1
Stearic acid	$(CH_3(CH_2)_{16}COOH)$	C18:0*	7	18.1
Oleic acid	$(CH_3(CH_2)_7CH=CH(CH_2)_7COOH)$	C18:1**	44.7	44.5
Linoleic acid	$(CH_3(CH_2)_4CH=CHCH_2CH=CH(CH_2)_7COOH)$	C18:2**	32.8	18.3
Linolenic acid	$CH_3CH_2CH=CHCH_2=CHCH_2=CH(CH_2)_7CO_2H$	C18:2*	0.2	0.2
Arachidic acid	$(CH_3(CH_2)_{16}(CH_2)_2COOH)$	C20:0*	0.2	0.8
Margaric acid	$(CH_3(CH_2)_{14}CH_2COOH)$	C17:0*	0.1	-
Total saturated acids			21.6	37.0
Total unsaturated			78.4	63.0

acids		
Ratio of saturated / unsaturated	1:3	2:3

***** saturated acids ****** unsaturated acids

4. CONCLUSION

The need for cooling and lubrication in machining are very important in minimising the impact of the contact processes at the cutting zone of the tool workpiece interface. Historically, over a century, water was used majorly as a coolant as a result of its high thermal capacity and availability (DI, 1998 and McCoy, 1994). Machines and parts corrosion and poor lubrication were the setbacks of such cooling process. Mineral oils were also employed at this time as these have much higher lubricity, but the lower cooling ability and high costs restricted their use for low cutting speed machining operations. It was later discovered that oil added to water (with a suitable emulsifier) gave good lubrication properties with good cooling effects and these became known as the soluble oils, however, environmental challenges are left to be addressed. Currently, there are wide scale evaluations of the use of MWFs in machining, so as to minimise the amount of lubricants in metal removing operations. However, these became less effective when employing better surface finish quality, higher machining efficiency and various cutting conditions are required. Krahenbuhl (2002) therefore, suggested vegetable oils as a viable replacement to petroleum, considering the subject from performance, cost, health, safety and environmental points of view. This work is therefore a review of recent researches in the application of vegetable oil-based cutting fluids during machining of AISI 304 alloy steel. The review focuses on the performance and environmental impact of these vegetable oils as emulsion and straight oils for various materials and machining conditions. The following are the major features:

1. The pH test, stability test, corrosion test and viscousity test were carried out for the individual adopted samples. ASTM D 445 was for standard viscousity test of 0.47 mm^2/s JSO and 0.44 mm^2/s NSO. While, ASTM D 4627 was for corrosion test. Stability test was carried out 72 hours for each sample with JA and NC samples highly stable, boasting 95% and 92% volume of water respectively. The pH test value for JSO and NSO were 8.36 and 8.67 respectively.
2. The ANOVA shows the input parameters contribution of cutting speed, feed, and depth of cut as follows: JBCF = cutting speed, CS (27.39%), feed rate, FR (6.16%) and depth of cut, DOC (62.73%) respectively for surface roughness; NBCF = cutting speed, CS (37.26%), feed rate, FR (24.78%) and depth of cut, DOC (36.74%); MBCF = cutting speed, CS (33.69%), feed rate, FR (38.29%) and depth of cut, DOC (24.53%).
3. The ANOVA show that DOC, CS and FR has more significant effect on the surface roughness with DOC (62.73%) for JBCF, follow by cutting speed (37.26%) for NBCF and, also feed rate (38.29%) for MBCF respectively.
4. The introduction of vegetable oil-based cutting fluids in machining applications has made it interesting

and possible to achieve better performance as reported by all researchers. Coconut oil showed the best performance at cutting speed (90 m/min), depth of cut (1 mm) and feed rate (0.35 mm/rev) when compared to mineral oil on turning of AISI 304 austenitic stainless steel. Surface roughness (Ra) of 4.5 mm and 5.5 mm were obtained respectively for coconut oil and mineral oil.

5. Vegetable oil-based cutting fluid is being identified as having superior lubricating properties compared to other based-oil. The use of these coolants has improved significantly the machining performances with reported increase of 117% in tool life and 7% reduction in thrust force. An increased machining performance and lower environmental impact can be obtained with vegetable oils-based cutting fluids. However, vegetable oil-based cutting fluids are good as metalworking fluids during machining process and their relative effects in improving product quality and reducing cutting force is work material dependent.
6. Sunflower oil-based cutting fluid employed during the drilling of AISI 304 austenitic stainless steel material and high speed steel E-grade tool had the least thrust force at spindle speed of 720 rpm. The least surface roughness was reported at spindle speed of 720 rpm when commercial vegetable cutting fluid was used. When the spindle speed was increased from 520 to 720 rpm, the surface roughness decreased by up to 32% for sunflower cutting fluid. Sunflower cutting fluids (a mixture of two surfactants and commercial vegetable cutting fluid) had low surface roughness at feed rate of 0.12 mm/rev. Sunflower cutting fluid had the least surface roughness of 2.04 mm at feed rate of 0.12 mm/rev.

REFERENCES

[1] Kuram, E., Ozcelik, B., & Demirbas, E. (2013). Environmentally Friendly Machining: Vegetable Based Cutting Fluids. J.P. Davim (ed.). *Green Manufacturing Processes and Systems, Material Forming and Tribology*. DOI: 10.1007/978-3-642-33792-52. Springer-Verlag, Berlin Heidelberg 2013. Retrieved, 6 October, 2015.

[2] Lawal, S.A., Choudhury, I.A., & Nukman, Y. (2012). Application of vegetable oil-based metal working fluids in machining ferrous metals-A review. *International journal of machine tools and manufacture* 52 (2012) 1-12. Journal homepage: www.elsevier.com/locate/ijmactool.

[3] Alves, S. M., & de Oliveira J. F. G. (2008). Development of new cutting fluid for grinding process adjusting mechanical performance and environmental impact. *Journal of Materials Processing Technology 179 (2006) 185–189.* University of S˜ ao Paulo, Engineering School of S˜ ao Carlos-EESC, Nucleos of Advanced Manufacturing, Brazil.

[4] Taga, O., Kiral, Z., & Yaman, K. (2015). Determination of Cutting Parameters in End Milling Operation based on the Optical Surface Roughness Measurement. Department of Mechatronics Engineering, Dokuz Eylül University, Tinaztepe, Buca, Izmir, 35397, Turkey. The Scientific and Technical Research Council of Turkey-Defense Industries Research and Development Institute, Ankara, 06261, Turkey.

[5] Woods, S. (2005). Going Green. *Cutting Tool Engineering*. **57** (2) pp 48-51.

[6] Richard, F. (2021). Tips for more efficient handling of cutting fluids.

Lubricant technology people. https://www.fuchs.com. Copyright FUCHS 2021.

[7] Bisio A.L., Xanthos M. (2005). How to manage plastics wastes, Technology and Market Opportunities, Hanser Publishers, NY.

[8] Li F., Hanson M.V., Larrock R.C. (2001). Soybean oil–divinylbenzene thermosetting polymers, synthesis, structure, properties and their relationships, Polymer 42 1567–1579.

[9] Eichenberger H.F. (1991). Biodegradable Hydraulic Lubricant—An Overview of Current Developments in Central Europe, Paper No. 910062.

[10] Busch C., Backe W. (1994). Rapidly biodegradable hydraulic fluids, Tribol. Schmi. 41 (1) 17–23.

[11] Flider F.J. (1995). Use of rapeseed oil in lubricants, INFORM 6 (9) 1031–1035.

[12] Operating hydraulics in ‘‘Green’’ fluids, Machine Design, 73–77, January 22, 1993.

[13] Vegetable oil based tractor lubricant, Off-Highway Engineering, pp. 7–10, December, 1994.

[14] El Baradie M.A. (1996). Cutting fluids: part 1. Characterization, *J. Mater. Process. Technol.* 56 (1996) 786–797.

[15] Rao, D. N., Srikant, R. R., & Rao, Ch. S. (2007). Influence of Emulsifier Content on Properties and Durability of Cutting Fluid. *Journal of Engineering the Brazilian Society of Mechanical, Science and Engineering*. Vol. XXIX, No. 4, October – December, 2007, pp 396 – 400.

[16] Club technical (2019). Mechanical engineering blog, manufacturing science. CC BY-SA 2.0, https://commons. Wikimedia.org/w/index.php?curid=29442 7

[17] Ademoh, N.A., Didam J.H. & Garba D.K. (2016). Investigation of Neem Seed Oil as an Altanative Metal Cutting Fluid. Department of Mechanical Engineering, Federal University of Technology, Minna, Nigeria and Department of Mechanical Engineering, Nigerian Defence Academy, Kaduna, Nigeria. *American Journal of Mechanical Engineering* *Vol. 4, No. 5*, 2016, pp191-199.doi:10.12691/ajme-4-5-4ResearchArticle.

[18] Singh, A. K., & Gupta, A. K. (2006). Metal working fluids from vegetable oils. Journal of Synthetic Lubrication. pages 167-176. Retrieved from http//www.interscience.willey.com.

[19] Abdalla, H. S., & Patel, S. (2006). The Performance and Oxidation Stability of Sustainable Metal-Working Fluid Derived From Vegetable Extracts Proc Inst. Mech Eng, Part B: Eng Manuf. 220: pp 2027-2040

[20] Krahenbuhl, U. (2002). Vegetable Oil-Based Coolants Improve Cutting Performance (Cutting Fluids). Tooling & Production. Nelson Publishing.

[21] Khan, M. M. A., & Dhar, N. R. (2006). Performance Evaluation of Minimum Quantity Lubrication by Vegetable Oil in Terms of Cutting Force, Cutting Zone Temperature, Tool Wear, Job Dimension and Surface Finish in Turning AISI – 1060 steel. *J Zhejiang Univ. – Sci. A (2006*) **7**(11): pp1790-1799. Doi:10.1631/jzus.2006.A1790.

[22] Juneja, B.L., Sekhon, G. S., & Seth, N. (2003). Fundamentals of Metal Cutting and Machine Tools. Second Edition. New Age International (P) limited Publishers 4835/24/Ansari Road, Daryanganj, New Delhi-110002.

[23] CAS Common Chemistry (2021). CAS, P.O. Box 3012, Columbus, Ohio 43210 U.S.A. help@cas.org 800-848-6538 (North America) 614-447-3600 (worldwide).

[24] BioPro (2015). JatroSolutions GmbH Echterdinger str. 3070599 Stuttgart.

[25] Winter, M., Öhlschläger, G., Dettmer, T., Ibbotson, S., Kara, S., & Herrmann, C. (2012) Using Jatropha Oil Based Metalworking Fluids in Machining Processes: A Functional and Ecological Life Cycle Evaluation. In: Dornfeld D., Linke, B. (eds) Leveraging Technology for a Sustainable World. Springer, Berlin, Heidelberg.

[26] Kazeem R.A., Adesina O.S. (2020). Performance evaluation of jatropha oil-based cutting fluid in turning AISI 1525 steel alloy. CIRP journal of manufacturing science and technology. Volue 31, Novemnber 2020, pages 418-430. https://doi.org/10.1016/j.cirpj.2020.07.004.

[27] Shivani, P., Khushbu, P., Faldu, N., Thakkar, V., & Shubramanian, R. B. (2011). Extraction and analysis of *Jatropha curcas* L. seed oil. Department of Biotechnology, Shree M. & N. Virani Science College, Rajkot, India-360005. 2BRD School of Sciences, Sardar Patel University, Vallabh Vidhyanagar, India. Accepted 30 September, 2011.

[28] Kuram E., Ozcelik B., Demirbas E., Sik E. (2010). Effects of the cutting fluid types and cutting parameters on surface roughness and thrust force, in: Proceedings of
the WCE 2010, London, UK, vol. II, June 30–July 2, 2010.

[29] Kuram E. (2009). Investigation of vegetable-based cutting fluids performance in drilling, M.Sc. Thesis, Gebze Institute of Technology, Gebze, Kocaeli, Turkey, 2009, (in Turkish).

[30] Davim J.P., Sreejith P.S., Gomes R., Peixoto C. (2006). Experimental studies on drilling of aluminium (AA1050) under dry, minimum quantity of lubricant, and floodlubricated conditions, Proc. Int. Mech. Eng. B: J. Eng. 220 (2006) 1605–1611.

[31] Basavarajappa S., Chandramohan G., Davim J.P. (2008). Some studies on drilling of hybrid metal matrix composites based on Taguchi techniques, J. Mater. Process. Technol. 196 (2008) 332–338.

[32] Ramulu M., Rao P.N., Kao H. (2008). Drilling of (Al2O3)p/6061 metal matrix composites, J. Mater. Process. Technol. 124 (2008) 244–254.

[33] Mendes O.C., Avila R.F., Abrao A.M., Reis P., Davim J.P. (2006). The performance of cutting fluids when machining aluminium alloys, Ind. Lubr. Tribol. 58/5 (2006) 260–268.

[34] Shetty R., Pai R., Rao S.S. (2009). Experimental studies on turning of discontinuously reinforced aluminium composites under dry, oil water emulsion and steam lubricated conditions using Taguchi’s technique, Gazi Univ. J. Sci. 22 (1) (2009) 21–32.

[35] Rivero A., Aramendi G., Herranz S., Lo´ L.N. Lacalle pez de (2006). An experimental investigation of the effect of coatings and cutting parameters on the dry drilling performance of aluminium alloys, Int. J. Adv. Manuf. Technol. 28 (2006) 1–11.

[36] Tsao C.C. (2007). An experiment study of hard coating and cutting fluid effect in milling aluminum alloy, Int. J. Adv. Manuf. Technol. 32 (2007) 885–891.

[37] Xavior, M.A., & Adithan, M. (2009). Determining the effect of cutting fluids on tool wear and surface roughness during turning of AISI 304 austentic stainless steel. J. Mater. Process. Technol. 209 (2009) 900-909.

[38] Krishna Vamsi P., Srikant R.R., Nageswara Rao D. (2010). Experimental investigation on the performance of nanoboric acid suspensions in SAE-40 and coconut oil during turning of AISI 1040 steel, Int. J. Mach. Tool Manuf. 50 (2010) 911–916.

[39] Pralhad, B., Patole, V. & Kulkarni V. (2018). Prediction of surface roughness and cutting force under MQL turning of AISI 4340 with nano fluid by using

response surface methodology. Bharati Vidyapeeth College of Engineering, Kolhapur 416004, M.S, India. Manufacturing Rev. 5, 5 (2018) © P.B. Patole and V.V. Kulkarni, Published by EDP Sciences 2018 https://doi.org/10.1051/mfreview/2018002.

[40] Zheng G., Rufeng X., Xiang, C., Guoyong Z., Li, L., & Jun, Z. (2018). Effect of cutting parameters on wear behavior of coated tool and surface roughness in high-speed turning of 300M. *journal homepage: www.elsevier.com/locate/measurement* School of Mechanical Engineering, Shandong University of Technology, 266 West Xincun Road, Zibo 255000, China School of Mechanical Engineering, Shandong University, 17923 Jingshi Road, Jinan 250061, China.

[41] Lawal, S.A, Choudhury, I.A., & Nukman, Y. (2013). Evaluation of vegetable and mineral oil-in-water emulsion cutting fluids in turning AISI 4340 steel with coated carbide tools. *Journal of Cleaner Production.* Manufacturing System Integration, Department of Mechanical Engineering, Faculty of Engineering, University of Malaya, 50603 Kuala Lumpur, Malaysia.

[42] Mishra, A,. & Gangele A. (2012). Application of Taguchi method in optimization of tool flank wear width in turning operation of AISI 1045 steel. Industrial Engineering Letters, 2012 - academia.edu. Research Scholar, Department of Mechanical Engineering, Suresh Gyan Vihar University, Jaipur (Raj.).

[43] Azom (2019). AZoNetwork UK Ltd. NEO, 4th Floor 9 Charlotte Street Manchester M1 4ET, UK Tel: +44 (0)16 1457 7150. www.azom.com

[44] Khandey, S.U. (2009), optimization of surface roughness, material removal rate and cutting tool flank wear in turning using extended taguchi approach. National Institute of Technology, Rourkela 769008, India.

[45] Yang, W.H., & Tarng, Y.S. (1998). Designed optimisation of cutting parameters for turning operations based on the Taguchi method. *Journal of Material Processing Technology* 84. 122-129.

[46] Korkut, I., Mustafa, K., Ibrahim, C., Ulvi, S. (2004). Determination of optimum cutting parameters during machining of AISI 304 austenitic stainless steel. Technical Education Faculty, Gazi University, 06500 Besevler, Ankara, Turkey Stellram Cutting Tool Company, 06370 Ankara, Turkey Institute of Science and Technology, Gazi University, 06570 Maltepe, Ankara, Turkey.

[47] Ojolo S.J., Ohunakin O.S. (2011). Study of rake face action on cutting using palmkernel oil as lubricant, J. Emerging Trends Eng. Appl. Sci. (JETEAS) 2 (1) (2011) 30–35 (&Scholarlink Research Institute Journals, (ISSN:2141-7016).

[48] Ojolo S.J., Amuda M.O.H, Ogunmola O.Y., Ononiwu C.U. (2008). Experimental determination of the effect of some straight biological oils on cutting force during cylindrical turning, Rev. Mate´ r. 13 (4) (2008) 650–663 /http://www. materia.coppe.ufrj.br/sarra/artigos/artigo11 007S.

[49] Rahim E.A., Sasahara H. (2011). A study of the effect of palm oil as MQL lubricant on high speed drilling of titanium alloys, Tribol. Int. 44 (2011) 309–317.

[50] DI N ISO 14040ff, Umweltmanagement-O¨ kobilanzen-Festlegung des Ziels und des Untersuchungsrahmens sowie Sachbilanz (dt. Und engl.), Berlin, Deutschland, 1998.

[51] McCoy J.S. (1994) Introduction: tracing the historical development of metalworking fluids, in: J.P. Byers (Ed.), Metalworking Fluids, Marcel Dekker, New York, 1994, pp.

JOURNAL OF THE NIGERIAN INSTITUTION OF MECHANICAL ENGINEERS
SEPTEMBER, 2021 VOL 10 NO 2 ISSN 2141-2987

CONTENT

Editorial